DYNAMICS OF VAPOR EXPLOSIONS: RAPID EVAPORATION AND INSTABILITY OF BUTANE DROPLETS EXPLODING AT THE SUPERHEAT LIMIT

Thesis by

Joseph Emmett Shepherd

In Partial Fulfillment of the Requirements

for the Degree of

Doctor of Philosophy

California Institute of Technology

Pasadena, California

1981

(Submitted September 12, 1980)

ACKNOWLEDGEMENTS

I would like to thank my advisor, Professor Bradford Sturtevant, for his patience, encouragement and advice throughout the course of our association.

The assistance of all those individuals who contributed to my practical education in graduate school is gratefully acknowledged. In particular, I would like to thank Mr. Harry Hamaguchi for his assistance in photography and the staff of the Aeronautics shop for their help and advice.

I would like to thank Mrs. Karen Valente for her expert typing of this manuscript under sometimes trying circumstances. My thanks to Mrs. Betty Wood for graciously drafting many of the figures on such short notice. The editorial assistance provided by Professor Bradford Sturtevant during the preparation of this manuscript was invaluable.

The author personally benefited from an Earl C. Anthony Fellowship during his first year of graduate school. The investigation described in the present work was supported by the Department of Energy.

Personally, my stay at Caltech was enriched by the friendship of many people, especially Mark Kushner. Finally, and most important, my wife Donna provided the support, love and encouragement without which, the task would have been insurmountable.

ABSTRACT

A preliminary experimental investigation of the vapor explosion of a single droplet (~ 1 mm diameter) of liquid butane at the superheat limit has been completed. These experiments provided the first detailed look at rapid evaporation taking place under conditions such that departures from equilibrium, evaporative fluxes and fluid accelerations are orders of magnitude larger than observed under ordinary circumstances. Single short-exposure photographs and fast-response pressure measurements were used to obtain a description of the complete explosion process within a superheated drop immersed in a bubble-column apparatus. Emphasis was placed on the early (microsecond-time-scale) evaporative stage. Despite the apparant simplicity of the vapor explosion of a single superheated droplet, the present experiments revealed a wide range of phenomina of varying complexity occurring at different stages of the explosion.

The explosion is initiated by the spontaneous formation within the drop of a single vapor bubble, which grows until the drop liquid is completely evaporated. The resulting vapor bubble undergoes volume oscillations and eventually breaks up via Taylor instability. Several new and unusual features of the early evaporative stage of the explosion have been observed, three of which are remarkably repeatable. First, photographs of the evaporative surface show a highly roughened and disturbed interface for most of the evaporative stage. At the earliest observed times (8 μsec) the roughening appears to begin as a rather regular pattern on an otherwise spherical surface, suggestive of a fundamental instability due to evaporative mass flux. Second, due to the asymmetric location of the initial nucleus within the drop, a portion of the evaporating

surface contacts the surrounding fluid first and becomes nonevaporating. As the bubble grows, a unique, axisymmetric structure of circumferential waves terminated by a spherical cap appears on this nonevaporating surface. Apparently, these waves are driven by the impinging jet of vapor coming from the opposing evaporating surface. Third, nucleation and initial development of the bubble in the first 10 μsec is accompanied by a characteristic two-step pulsating pressure signal, suggesting that a fundamental and repeatable unsteadiness, perhaps connected with the above mentioned instability, is taking place at this stage.

A preliminary estimation of the evaporative mass flux has been made from photographically-determined bubble volumes and pressure signals measured in the first 30 μsec. As might have been expected in view of our observations of the highly roughened surface, the inferred mass flux ($\sim$ 400 gm/cm^2-sec) is two orders of magnitude larger than that predicted by the classical, diffusion-limited theory of bubble growth. We propose that the interface roughening is due to an inertial instability of the evaporative surface. A preliminary calculation for the Landau mechanism of instability, supplemented by an ad hoc correction for sphericity indicates that, indeed, the classical mode of bubble growth would be unstable under the conditions found in the present experiment. An explanation of the present observations that is consistent with this theoretical prediction is that the actual instability does occur in the first 1-2 μsec of bubble growth and the instability has developed well into the nonlinear stage by 8 μsec, the earliest time at which bubbles have been observed in the present experiment.

The present observations are completely different than what might be predicted from previous experiments and analyses of near-equilibrium evaporation. The generality of the present results needs to be verified in detail, but they clearly indicate that evaporation at the superheat limit can be much more complex than previously expected.

TABLE OF CONTENTS

TABLE OF CONTENTS (Continued)

TABLE OF CONTENTS (Contents)

I. INTRODUCTION

1.1 Motivation

Destructive industrial accidents and violent natural processes very often involve the sudden contact of two liquids at very different temperatures or the rapid depressurization of a container of heated liquid. In the last 30 years, many examples have been hypothesized or documented in such varied situations as foundries (Witte et. al. 1970), the paper industry, LNG spills into seawater (Reid 1978), nuclear reactor cooling system failures (Board and Caldarola 1977), railroad tank car explosions (Reid 1979) and molten lava-water interactions (Colgate and Sigurgierson 1973). This last example is the most speculative and spectacular, possible cases being the catastrophic explosion of Krakatoa in 1886 and more recently the eruption of Mt. St. Helens (Kerr 1980). A common feature of all these events is their explosive nature; they occur very rapidly and produce destructive blast waves which propagate into the surroundings.

Physically, the mechanisms of all these explosions is the extremely rapid evaporation of the superheated liquid resulting from depressurization or contact with a hotter fluid. The rapidly evolved vapor then displaces the surrounding fluid to produce the blast waves similar to the action of a conventional explosive. However, this vapor explosion differs in several crucial ways from a conventional explosion: it is endothermic rather than exothermic, there is no chemical reaction other than the change in phase and the specific energy release is smaller.

Currently, a qualitative and detailed theory of vapor explosions does not exist. Present understanding is based on observations of

medium and large scale experiments consisting of injecting or pouring various combinations of molten metal and liquid into one another (Anderson and Armstrong 1974). Such interactions are very complex events involving fluid mixing and fragmentation (usually turbulent), heat transfer (often film boiling), multiphase flow and of course, highly non-equilibrium evaporation. Very often the only result reported from such an experiment is that a particular combination of liquids does or does not explode. Invariably, it is found that explosions will always occur if the temperature of the cooler liquid can be raised to the superheat limit. This is the highest temperature at a given pressure to which a superheated liquid can be elevated before spontaneously evaporating.

In contrast to vapor explosions, the homogeneous nucleation theory of the superheat limit is relatively well developed and supported by extensive experimentation. Most of those experiments have been carried out in a particularly simple geometry in which a single droplet of liquid immersed in a host liquid is brought to the superheat limit in a controlled way. Despite the widespread use of this technique since its introduction 20 years ago (Wakeshima and Takata 1958, Moore 1959) the fundamental details of the evaporation process were never investigated. Experimenters were simply interested in the physical chemistry of the superheat limit and the explosive aspect of the vaporization was ignored. Rudimentary facts such as the time scale and overpressure characterizing the explosion were completely unknown and the subject of speculation.

The challenge of the unknown dynamics in such a simple system made it an ideal and obvious choice for the application of

high speed diagnostic techniques (spark photography, piezoelectric pressure transducers) which have been used extensively in gas-dynamics and conventional explosion research. Despite the apparent simplicity of the vapor explosion of a single superheated droplet, the current investigation revealed a wide range of phenomena of varying complexity occuring at different stages of the explosion. A number of unique and previously unreported features of the early stages of explosive evaporation of the droplet have been observed along with some well known features, at the later stages, of bubble dynamics. Emphasis has deliberately been placed on the most non-equilibrium and therefore least understood process of rapid evaporation occurring in the earliest stages of the explosion.

1.2 Basic Theory and Previous Related Work

In this section, a brief summary of relevant background information is presented. The thermodynamics and kinetic theory of the superheat limit is discussed and the experimental technique of superheating explained. Previous theories and experiments on the growth of bubbles from nuclei are mentioned and key differences with the present observations pointed out. The connection of the later stages of droplet vapor explosion and underwater explosions is mentioned and some features of the motion discussed.

1.2.1 Superheat Limit and Metastability

The physical basis for superheating is that it is possible for a liquid to exist at a thermodynamic state where its chemical potential μ is higher than that of its vapor at the same state. Such liquid states are metastable and can only be produced if all sources

of gas nuclei (rough container walls, free surfaces and dissolved gas) are eliminated. The ultimate thermodynamic limit to the existance of such a state is the violation of mechanical or thermal stability. In practice, it is the former requirement which is observed to hold;

$$\left(\frac{\partial p}{\partial v}\right)_T = 0 \quad . \tag{1-1}$$

The locus of points where this is satisfied is known as the spinodal and can be visualized as a line in the pressure-volume plane (Figure 1.1) or pressure-temperature plane (Figure 1.2). The unstable portion of the isotherm, where $\left(\frac{\partial p}{\partial v}\right)_T > 0$, is shown as a dashed line on Figure 1.1. The measured limit of superheat lies near but usually somewhat below the limit predicted by equation 1-1 using typical equations of state extrapolated into the metastable region (Reid 1978).

A mechanistic approach to the superheat limit which is the basis for a more detailed description of the evaporative process is the homogeneous nucleation theory. From the point of view of statistical mechanics, there are constantly fluctuations in phase occurring within the liquid. These fluctuations take the form of microscopic gas bubbles with a spectrum of sizes. The growth or decay of such a bubble is determined by the balance between the work required in generating new surface area (due to surface tension) and the lower free energy of the vapor phase. There is, therefore, a critical size below which a bubble will collapse and above which a bubble will grow. The classical expression for this critical radius R_o is

$$R_o = \frac{2\sigma}{(p_v - p_\infty)} \tag{1-2}$$

where p_v is the pressure in the vapor, p_∞ the ambient pressure and σ the surface tension. When the spectrum of bubbles contains a large number with radii greater than critical, it is concluded that liquid is unstable since these nuclei will grow and ultimately cause a change of phase.

The spectrum of sizes is calculated on a probabilistic basis using the fluctuation theory of statistical mechanics. The probability of a fluctuation of a given size is proportional to

$$e^{-\frac{\Delta W(R)}{kT}} \tag{1-3}$$

where $\Delta W(R)$ is the change in energy necessary to create the bubble of size R. An extensive review of the effort to calculate the superheat limit using this approach and a number of experimental results can be found in Skripov (1974).

The connection to the thermodynamic limit of stability is through the fluctuation theory result of statistical mechanics (Landau and Lifshitz 1969) which relates fluctuations in density $\Delta\rho$ of a volume of fluid V to the isothermal compressibility

$$\overline{(\Delta\rho)^2} = \rho^2 \frac{kT}{V^2} \left(\frac{\partial p}{\partial v}\right)_T^{-1} . \tag{1-4}$$

Since fluctuations in phase are nothing more than fluctuations in density in a liquid-vapor system, as $\left(\frac{\partial p}{\partial v}\right)_T \to 0$ the fluctuations in phase become large and the probability of the creation of a greater than critical sized nucleus rapidly increases.

Thus, in conclusion, the absence of heterogeneous nucleation sites leads to the existence of metastable liquid states. These states are possible until the temperature is increased to the vicinity

of the thermodynamic limit of stability where fluctuations in phase result in homogeneous nucleation and subsequent evaporation.

1.2.2 Experimental Technique

A number of methods have been used to produce superheated liquids. From Figure 1.2 it can be seen that metastable liquid states can be reached from stable states by some combination of increasing the temperature and/or reducing the pressure. The heterogeneous nucleation is suppressed by containing the liquid with a microscopically smooth surface such as another liquid or a freshly prepared glass capillary. Alternately, the experiment is performed on a transient basis, superheating the liquid sufficiently rapidly to achieve the desired state before heterogeneous nucleation sets in.

In the current investigation, the apparatus used is the bubble column first devised by Wakeshima and Takata (1958). In this device, a vertical column of host liquid is maintained hotter at the top than at the bottom. The substance to be studied is introduced at the bottom in the form of a small ($\sim$ 1 mm dia.) liquid drop. The host liquid has been selected so that the drop liquid is both immiscible and buoyant in the host. In addition, the host is chosen so that it remains in the stable liquid state for a temperature range encompassing the boiling and superheat limit temperatures of the drop substance.

The droplet liquid is initially in the stable state and as it slowly rises up the column under the action of gravity, it is superheated at essentially constant pressure due to the heat transfer from the surrounding host. By selecting sufficiently small drops, the velocity of rise will be slow enough so that the drop temperature

is reasonably uniform and close to the host temperature at that point in the column. In this way, the drop temperature can be increased to the limit of superheat at the top of the column where homogeneous nucleation occurs and the drop evaporates with an explosive pop.

In the past 20 years, a large number of substances (particularly hydrocarbons and hydrocarbon mixtures) have been investigated by this technique and for many of these substances, the superheat limit at one atmosphere pressure is 0.9 T_c, where T_c is the critical temperature (Blander and Katz 1975).

The explosive pop at the moment of evaporation has been reported by many investigators and represents the "blast wave" radiated by the mini-vapor explosion that has taken place. However, until the current investigation, no instrument other than the human ear has been used to measure this pressure wave. Thus the first measurement made in this investigation was a determination of the pressure waveform via a fast piezoelectric transducer. The waveform had a completely unexpected and complex appearance with significant structure or "bumpiness" on a microsecond time scale which was remarkably repeatable for different drops (Sturtevant and Shepherd 1977). Much of the subsequent flow visualization was motivated by the desire to understand the physical processes responsible for the unique pressure waveform.

1.2.3 Bubble Growth and Evaporation

The implication of the homogeneous nucleation theory is that evaporation at the superheat limit is effected by the growth of greater than critical size nuclei. That is, nuclei grow to form macroscopic

bubbles and the vapor inside each bubble is provided by the evaporation of liquid at the liquid-vapor interface comprising the bubble surface. In the current investigation, it is found that one such bubble is responsible for the evaporation of a drop. Thus theory and experiments on the growth of vapor bubbles in superheated liquids are very relevant to understanding the results of the current investigation.

Starting with the theoretical work of Plesset and Zwick (1954) and the experiments of Dergarabedian (1953) there have been numerous investigations of this problem and the closely related phenomenon of cavitation. Experimental work has been mainly visualization studies with high speed movies of bubble growth in bulk liquid at relatively low superheat (some examples are Dergarabedian 1960, Florschuetz et. al. 1969, Hooper et. al. 1970, Kosky 1968, Hewitt and Parker 1968). Results relevant to the current investigation are: the bubbles have a smooth surface, are very spherical and grow radially with the square root of time. This behavior and in particular the dependence of growth rate on superheat and substance is in accord with the theory, the most recent version of which can be found in Prosperetti and Plesset (1978). In this theory, the vapor is assumed to be in equilibrium and at saturated conditions as determined by the interface temperature. The interface temperature is determined by the heat flux into the interface which provides the latent heat necessary to support the mass flux through the interface (evaporation).

Approximating this heat transfer process as a thin thermal boundary layer in the liquid next to the bubble surface and determining the bubble motion by incompressible dynamics results in a simple, complete description which has to be solved numerically in

the general case. The corresponding linear version (planar interface) of this model using compressible dynamics has been developed and the simple analytical solution presented here for comparison.

Cavitation research has emphasized a very different aspect of bubble dynamics than the experiments mentioned above. Physically, the dynamics of cavitation bubbles are different since the heat transfer associated with evaporation is usually negligible (Plesset and Prosperetti 1977) and the fluid dynamics of the surrounding liquid is the main factor in determining bubble motion. There has been an extensive treatment (beginning with Kornfeld and Suvorov (1944)) of the role of surface instabilities in collapsing cavitation bubbles as part of the effort to understand the mechanism of cavitation damage. Typical examples of the experimental work can be found in Benjamin and Ellis (1966) and Lauterborn (1974); both theoretical work and the experiments are reviewed in detail by Plesset and Prosperetti (1977). The importance and relevance of these results to the present work is the possibility of such surface instabilities existing on the vapor bubbles formed in the droplet explosion. In fact, two distinct types of surface instabilities were observed in the present experiment; one occurs on the evaporating bubble surface (for different reasons than the instabilities occur on cavitation bubbles) and is discussed below and in Chapter 5; the other occurs at a later stage on the oscillating gas bubble (this is more closely related to the instabilities observed in cavitation bubble collapse) and is discussed in the next section.

The conditions in the current investigation differ from those in the previous experiments and theories mentioned above in two important ways. First, the amount of liquid superheated is small and

therefore the interaction of the growing bubble with the surrounding non-evaporating fluid is important. This interaction was observed in the present experiments in the form of a unique and repeatable axisymmetric disturbance on the vapor-host interface which gives the evaporating droplets a completely unexpected appearance. This disturbance can be conceived of as being produced by the "jet" of vapor evaporated from the opposing surface and impinging on the vapor-host interface. Second, the degree of superheat is much larger, resulting in a system far from equilibrium where theory is on much less firm ground and no observations have previously been made. Present observations show that indeed, the evaporation process appears completely different than has been previously observed or theorized. Photographs of the evaporating surface show a highly roughened and disturbed interface for most of the evaporative stage, a fundamental difference which must drastically influence the mass transfer processes occurring there. More quantitative differences are revealed by calculation of the evaporation rates at early times from experimental data and comparison to the Prosperetti-Plesset theory. The origin of the interface roughness as an instability of the evaporation process is considered and evidence that this has occurred is presented.

1.2.4 Underwater Explosions and Bubble Oscillations

The evaporation of superheated droplets in the current investigation and associated acoustic radiation is a microscopic analog of the explosion of a conventional charge underwater (for a complete discussion of underwater explosions see Cole (1948)). Initial phases of the two processes are similar but differ greatly in intensity.

Detonation of a conventional explosive results in the almost instantaneous creation of a high pressure gas bubble whose impulsive motion produces a shock wave of large amplitude and short rise time. Evaporation proceeds much more slowly than detonation and the pressure wave produced is characterized by its slow rate of increase.

Both processes result in the creation of a high pressure gas bubble in the surrounding host fluid. Such a bubble-liquid system is a nonlinear oscillator with the inertia of the surrounding liquid acting as an effective mass and the pressure-volume relation of the gas providing the spring action. For an incompressible liquid both Cole (1948) and Heuckroth and Glass (1961) have given solutions, and the compressible case has been treated by Epstein and Keller (1971) and Keller and Kolodner (1956). In both cases, the result is that radiation of pressure waves occurs primarily at the minima of the oscillations in bubble volume. These waves are known as "bubble pulses" in underwater explosions and can be seen in all the pressure traces obtained in the current investigation.

The oscillatory motion of the initially spherical bubble is unstable with respect to the creation of surface waves on the bubble (Plesset 1954, Birkhoff 1956, Strube 1971). This especially occurs near the minima in volume where the accelerations are directed from the light vapor to the heavy liquid - a Taylor unstable motion. It is this instability which is a dominating feature of the motion of the bubble and leads to its eventual breakup. Very clear photographs of this process have been obtained and the initial length scales of the instability have been compared to those predicted by the linear theory.

The material in this section is included in this report since it does provide a description of the final stage of droplet vapor explosions which has not been previously observed. However, since this aspect of the problem is well understood in comparison with the evaporative stage of the process, it is not further investigated or emphasized in the present work.

1.3 Outline of the Present Work

The present work is an experimental investigation of the vapor explosion of single liquid butane droplets at the superheat limit. This experiment was of an exploratory nature and at the outset the time scales, mode of evaporation and blast wave strength were completely unknown. In the course of obtaining some of this fundamental information, it became clear that every droplet undergoes a well-defined, repeatable sequence of events which divides the process into stages.

Using high-speed photography and pressure measurements a general survey of all stages was made and an overview of the results is presented in Chapter 3. Briefly, a single bubble forms within the drop and grows until the drop liquid is completely evaporated, producing a vapor bubble which oscillates in volume and eventually breaks up into smaller bubbles via Taylor instability. Two new and unexpected features of the evaporation have been observed. The evaporating bubble surface displays a regularly wrinkled appearance at the earliest observed times ($\sim$ 8 μsec) which rapidly develops into a very rough and highly non-uniform surface persisting for the remainder of the evaporative stage. The invariably observed asymmetric location of the bubble within the drop results in the interaction

of a portion of the evaporating interface with the non-evaporating host fluid near the beginning of the evaporative stage. This interaction results in a unique axisymmetric ridged structure on the surface of the bubble terminated by a spherical cap.

Consequences of these unusual features of the motion are explored by using the photographically-determined volume growth rates and measured pressures to deduce the evaporative mass flux at very early times. The calculated mass flux is many times larger than that predicted by the standard theories of bubble growth and has a complex time behavior reflecting its dependence on measured pressures. Possible instability of the evaporating interface is considered as a mechanism for producing the observed roughness and wrinkling of the bubble surface. Growth rates and the most unstable wavelengths are calculated for the Landau mechanism of instability and compared to the regular wave-like features on the bubble surface at the earliest times.

Finally, as a method for illustrating the implication of applying the standard model of bubble growth to problems with large superheat, a linear one-dimensional version of bubble growth is developed and solved. Some of the limitations at large superheats of the approximations used are pointed out, in particular the exclusion of a class of steady-state solutions.

REFERENCES

Anderson, R. P. and Armstrong, D. R. 1974 "Comparison Between Vapor Explosion Models and Recent Experimental Results", AIChE Symposium Series 70(138), 31.

Benjamin, T. B. and Ellis, A. T. 1966 "The Collapse of Cavitation Bubbles and the Pressures Thereby Produced Against Solid Boundaries", Phil. Trans. Roy. Soc. A260, 221.

Birkhoff, G. 1956 "Stability of Spherical Bubbles", Q. Appl. Math. 13, 451.

Blander, M. and Katz, J. L. 1975 "Bubble Nucleation in Liquids", AIChE Journal 21, 833.

Board, S. J. and Caldarola, L. 1977 "Fuel-Coolant Interactions in Fast Reactors", in Symposium on the Thermal and Hydraulic Aspects of Nuclear Reactor Safety. Vol. 2: Liquid Metal Fast Breeder Reactions. (ed. O. C. Jones, Jr. and S. G. Bankoff), American Society of Mechanical Engineers, New York, New York, 195.

Cole, R. H. 1948 Underwater Explosions, Princeton University Press, Princeton, New Jersey.

Colgate, S. A. and Sigurgeirson, T. 1973 "Dynamic Mixing of Water and Lava", Nature 244, 552.

Dergarabedian, P. 1953 "The Rate of Growth of Vapor Bubbles in Superheated Water", J. App. Mech. 20, 537.

Dergarabedian, P. 1960 "Observations on Bubble Growth in Various Superheated Liquids", J. Fluid Mech. 9, 40.

Epstein, D. and Keller, J. B. 1971 "Expansion and Contraction of Planar, Cylindrical, and Spherical Underwater Gas Bubbles", J. Acous. Soc. Am. 52, 975.

Florschuetz, L. W., Henry, C. L. and Khan, A. Rashid 1969 "Growth Rates of Free Vapor Bubbles in Liquid at Uniform Superheats Under Normal and Zero Gravity Conditions", Int. J. Heat Mass Transfer 12, 1465.

Heuckroth, L. E. and Glass, I. I. 1961 "Low-Energy Underwater Explosions", Can. Aero. J 7, 2095.

Hewitt, H. C. and Parker, J. D. 1968 "Bubble Growth and Collapse in Liquid Nitrogen", J. Heat Transfer 90, 22.

Hooper, F. C., Eidlitz, A. and Faucher, G. 1970 "Bubble Growth and Pressure Relationships in the Flashing of Superheated Water", Vols. 1-3, Technical Publication 6904, University of Toronto, Department of Mechanical Engineering.

REFERENCES (Continued)

Keller, J. B. and Kolodner, I. I. 1956 "Damping of Underwater Explosion Bubble Oscillations", J. App. Phys. 27, 1152.

Kerr, R. 1980 "Mt. St. Helens: An Unpredictable Foe", Science 208, 1447.

Kornfeld, M. and Suvorov, L. 1944 "On the Destructive Action of Cavitation", J. App. Phys. 15, 495.

Kosky, P. G. 1968 "Bubble Growth Measurements in Uniformly Superheated Liquids", Chem. Eng. Sci. 23, 695.

Landau, L. D. and Lifshitz, E. M. 1969 Statistical Mechanics, Pergamon, New York.

Lauterborn, W. 1974 "General and Basic Aspects of Cavitation", in Finite-Amplitude Wave Effects in Fluids (ed. L. Bjørnø), IPC Science and Technology Press, Ltd., Surrey, England, 195.

Moore, G. R. 1959 "Vaporization of Superheated Drops in Liquids", AIChE Journal 5, 458.

Plesset, M. S. 1954 "On the Stability of Fluid Flow with Spherical Symmetry", J. App. Phys. 25(1), 96.

Plesset, M. and Prosperetti, A. 1977 "Bubble Dynamics and Cavitation", in Ann. Rev. Fluid Mech (9) (ed. van Dyke, et al), Annual Revies Inc, Palo Alto, California, 145.

Plesset, M. S. and Zwick, S. A. 1954 "The Growth of Vapor Bubbles in Superheated Liquids", J. App. Phys 25(4), 493.

Prosperetti, A. and Plesset, M. S. 1978 "Vapor Bubble Growth in a Superheated Liquid", J. Fluid Mech. 85, 349.

Reid, R. C. 1978 "Superheated Liquids: A Laboratory Curiosity and, Possibly, an Industrial Curse", Chem. Eng. Ed. 12, 60.

Reid, R. C. 1979 "Possible Mechanism for Pressurized-Liquid Tank Explosions or BLEVE's", Science 203, 1263.

Skripov, V. P. 1974 Metastable Liquids, Wiley, New York.

Strube, H. W. 1971 "Numerische Untersuchungen zur Stabilität nichtsphärisch schwingender Blasen", Acustica 25, 289.

Sturtevant, B. and Shepherd, J. 1977 "The Dynamics of Vapor Explosions", APS Bull. 22, 1274.

Wakeshima, H. and Takata, K. 1958 "On the Limit of Superheat", J. Phys. Soc. Japan 13, 1398.

REFERENCES (Continued)

Witte, L. C., Cox, J. E. and Bouvier, J. E. 1970 "The Vapor Explosion", Journal of Metals 22, 39.

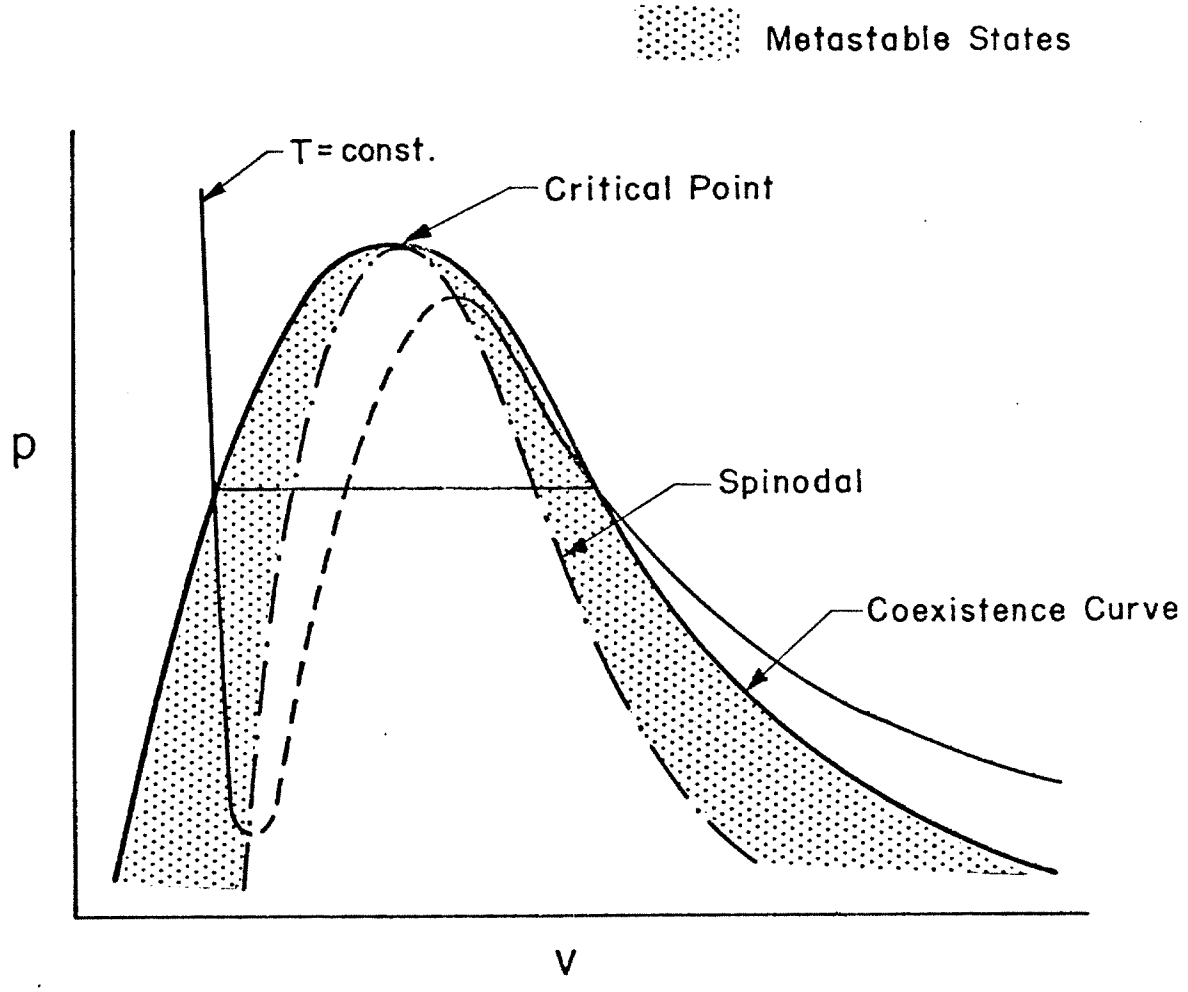

FIG. I.1 PRESSURE-VOLUME PLOT SHOWING LIQUID, VAPOR AND METASTABLE STATES

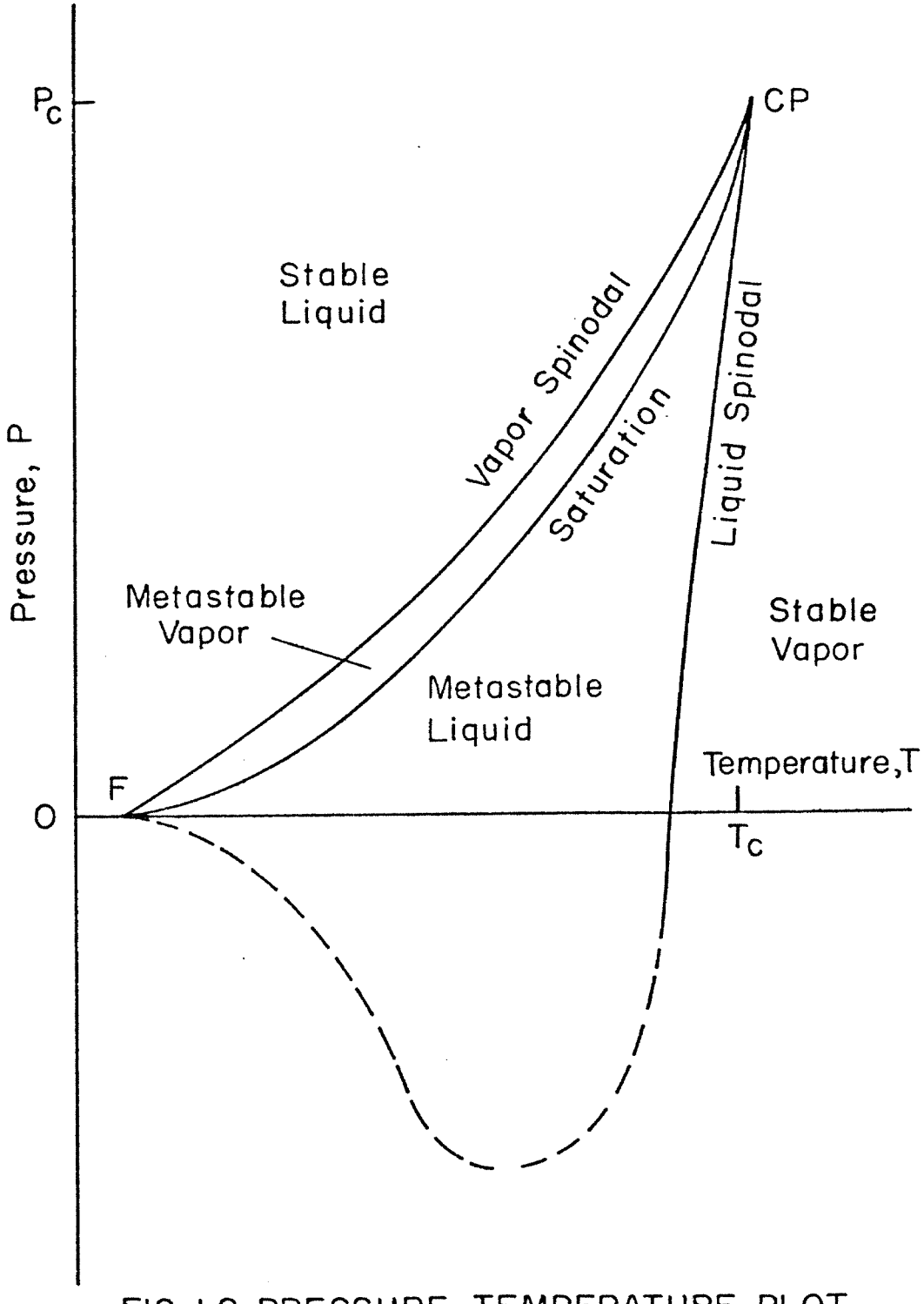

FIG. I.2 PRESSURE-TEMPERATURE PLOT SHOWING LIQUID, VAPOR AND METASTABLE STATES

II. EXPERIMENTAL FACILITY AND INSTRUMENTATION

2.1 Introduction

In this chapter, the equipment and operating procedure used in the experiment is described. The basic apparatus in which explosions are produced is a vertical column of ethylene glycol heated at the top and cooled at the bottom. Droplets of liquid n-butane (~ 1 mm dia.) are introduced at the bottom and are superheated as they drift up the column. Near the top of the column the droplets reach their superheat limit (105° C) and explode. In principle, this is the same technique of superheating that was first used by Wakeshima and Takata (1958). The explosion occurs in an instrumented test section where the pressure produced by the explosion is detected by fast piezoelectric transducers and digitally recorded. The explosion is photographed at a preset delay time after the detection of the pressure signal. Illumination is provided by a triggered spark gap and both transmitted and scattered light are imaged simultaneously.

2.2 Apparatus

A bubble column designed for continuous operation with automatic temperature control was the basic facility used in the current investigation. A test section at the top of the column was equipped with access ports into which different transducers and optical windows could be inserted according to the type of experiment being conducted.

The choice of substance in the current investigation was dictated by convenience and the past experience of other investigators. Ethylene glycol was used as the host liquid since it is an easily available, relatively non-toxic substance which has been used successfully

before, for example, see Porteous and Blander (1975). Butane, the middle member of the alkane family of hydrocarbons, was used for the superheated droplets since it has convenient boiling (- 0.5° C) and superheat limit (105° C) temperatures for use with pure glycol as host. An important point is that the superheat limit is low enough so that heat-sensitive pressure transducers can survive in the test section without special precautions. Representative properties of n-butane and ethylene glycol can be found in Tables 2.1 and 2.2 respectively.

Unlike many experiments with superheated liquids, no special precautions were taken with regard to purity. Both butane and glycol used were of technical grade and discoloration and particulates in the glycol were quite evident after months of use. However, the superheat limit observed was within the range reported by other experimenters (Blander and Katz 1975) and no premature nucleation was noticeable. Contrary to some reports (Reid 1978), <u>every</u> drop which contained only pure liquid reached the superheat limit and exploded.

The column proper (see Figure 2.1) consists of a 12" section of Pyrex 4" diameter pipe which together with a 6" high, 4" square anodized aluminum test section contains the host fluid. At the bottom, the pipe is seated onto a refrigerated aluminum base plate which contains the drop injector and a drain valve. At the top the test section is sealed with an anodized aluminum top plate to which is attached an expansion volume for the host fluid, an electrical heater (500 W) and a thermocouple which can be traversed along the centerline of the column.

Refrigeration is a two step process, with the primary unit an ordinary freon (R-12) charged compressor system cooling an ethylene glycol-water bath (Figure 2.2). The secondary loop is powered by a peristaltic pump which circulates an ethylene glycol-water solution through the bath, the base plate and the drop injection mechanism. The bath and secondary loop are contained in an insulated compartment underneath and supporting the base plate. The test section and column are also insulated. To compensate for the vastly different thermal conductivities of the test section and the remainder of the column, two aluminum strips (labeled heat sinks in Figure 2.1) are connected between the bottom of the test section and the base plate. The size of strips is adjusted so that the temperature gradient measured along the centerline of the column in the test section is $\sim 1.5^{\circ}$ C/cm; a value which yielded an acceptable minimal scatter in the location of the explosion.

Thermocouples located in the bath, base plate and top plate are connected to on-off controllers of conventional design which independently regulate the primary and secondary refrigeration systems and the heater. All thermocouples used are of chromel-constantan type and both legs of each circuit are referenced to a water-ice bath, the voltages are read by a digital multimeter (Keithley 163b) which can be switched in parallel to the inputs of the controllers. Typical operating temperature ranges (determined by the setting and hysteresis of the controller) are: top plate, 118 to 121° C; test section center, 104.5 to 105.5° C; base plate, - 8 to -9.5° C; bath, - 26 to -30° C.

A stainless steel holding tank (see Figure 2.2) immersed in

the glycol-water bath is used to liquefy and store the butane. Butane is transferred into the tank from the commercial high pressure bottle (at room temperature) after the tank is evacuated by a roughing pump and sealed off. The high pressure bottle and tank are isolated and the butane allowed to condense. A small amount of helium is then admitted to pressurize (5-10 psig) the liquid butane.

Butane is injected into the bottom of the column through a shortened and squared off No. 19 (0.008" i.d.) hypodermic needle attached via standard LUER-LOK fittings and tygon tubing to a glass 5 cc syringe. The syringe is fitted with a cooling jacket through which the secondary coolant is circulated and a micrometer screw which is used to translate the plunger. Approximately 1/4 turn of the micrometer screw will produce a single ~ 1 mm dia. droplet. At the beginning of a series of experiments (and whenever the butane in the syringe is depleted), the syringe is filled by backing off the plunger micrometer and cracking open the valve to the pressurized holding tank, allowing the butane to enter and push back the plunger.

Once a drop is formed at the end of the hypodermic needle, often surface tension forces prevent it from escaping up the column. A jet of host fluid directed upward from a tube concentric with the needle gives the necessary impulse to start these drops drifting upward. The jet is merely a short squirt produced by a manually operated syringe located beneath the base plate. An insulated viewing port equipped with a magnifying lens is used to view the operation of the drop injector.

2.3 Operation

Due to the large mass of fluid and metal involved, the column takes approximately 10 hours to reach a steady-state condition after turn on. Between explosions of individual droplets a certain period of time (5-10 minutes) must be allowed to elapse during which the mixing induced by the explosion subsides and the quiescent conditions are re-established. These circumstances compel the actual experiments to be conducted in a series of runs, for each of which the apparatus is left on continuously for several days. During each run between 50 and 100 individual explosions would be successfully recorded. The data presented in this work are the cumulation of numerous runs over a period of three years. Many involved testing various diagnostic techniques and thus did not contribute to the data bank.

The course of a typical run is as follows: the primary and secondary cooling loops are turned on and the temperature in the bath and base plate reduced below the butane boiling point. Butane in the holding tank is replenished if necessary and the syringe filled with butane; after testing the drop injector and checking the level of host fluid the heater is turned on. Monitoring the test section temperature profile to determine when steady state conditions are reached, the heater controller is then adjusted to obtain the desired explosion location, i.e., position of superheat limit in the test section. During the initial equilibration period the electronics and optics have been set up and aligned so that recording explosions can begin at this point.

2.4 Instrumentation and Data Acquisition

The observations which form the basis of this work are simultaneous recordings of the pressure waves measured by fast piezoelectric transducers and single short-exposure photographs of the exploding drops. In addition, some preliminary measurements using spark shadowgraphy and optical extinction methods were first steps in understanding the problem and are documented in Appendix A.

2.4.1 Pressure Measurements

The utility of fast pressure transducers depends on the existence of significant structure in the acoustic radiation of the explosion on a time scale short compared to the acoustic transit time in the test section. This was in fact verified by the first experiment in the apparatus; the sound speed in ethylene glycol at 108° C is 1.5 mm/μsec and the characteristic scale of the test section is 100 mm yielding a transit time of 66 μsec, much larger than the observed structure (Figure 3.19) time scale of 10 μsec.

Transducers used were Model PCB 113A21 manufactured by Piezotronics and were mounted directly in aluminum or brass plugs placed in one of three locations in the test section shown in Figure 2.3. All transducers were mounted so the face of the sensitive element (flush with the face of the plug) was normal to and concentric with the nominal origin of the explosions, the center of the test section.

Acoustically, the explosion can be characterized as a compact volume source producing, at distances large compared to the source size, outwardly propagating spherical waves. The pressure measured

by the transducer is the sum of the pressure produced by primary waves directly propagated from the explosion and secondary waves indirectly propagated through reflection and diffraction from the interior of the test section. Due to the large difference in acoustic impedance of the glycol and the mounting plug-transducer combination, any wave incident on the transducer will undergo reflection, momentarily doubling the signal strength. Similar reflection processes occur at the other boundaries of the test section and result in secondary waves arriving at the transducer sometime later than the primary wave. The presence of these secondary waves and others produced by diffraction at the edge of the transducer plug, etc., make quantitative interpretation of the measured pressures difficult. This is especially true at very long times (1-10 msec) where the test section acts like a lossy acoustic resonator driven by the oscillations of the bubble resulting from the explosion.

Overall, the qualitative appearance of the pressure trace is similar to that produced in the absence of these deleterious effects since the secondary waves have traveled much farther to reach the transducer and hence, due to their spherical nature, are considerably attenuated relative to the primary waves. Transducer configurations A and B of Figure 2.3 were used primarily to obtain a reference signal to trigger the light source used for photography. Configuration C was used to obtain quantitative information at the earliest stages (< 30 μsec) of the explosion before the secondary waves first reached the transducer.

The voltages produced by the transducers were directly recorded by a Nicolet Explorer III digital oscilloscope and stored as

digital data on a minifloppy magnetic disk. The Explorer III could be interfaced (via IEEE 488 bus) to a calculator-based computer system (HP 9825) to whose floppy disk the raw data were permanently transferred at the end of a run. The scaling, plotting and further processing of the data presented in the present work were all carried out with this system.

A very important feature of the Explorer III for this experiment was the "pretrigger" option; a consequence of the digital memory, this enables a portion of a waveform received before the trigger signal to be saved. In this case, the trigger signal was the pressure waveform itself and the use of this feature allowed the beginning of this signal to be recorded and used as a reference ("zero time") for succeeding events.

2.4.2 Photography

The technical accomplishment which made the present investigation successful was the photography of evaporating vapor bubbles within the liquid droplet. Preliminary investigations (Appendix A) with parallel light revealed that the basic difficulty was the focusing action of the droplet due to the greatly differing indices of refraction of host ($n = 1.43$) and drop liquid ($n = 1.33$). Parallel light incident on the drop is refracted and emerges as a cone of light spreading out so that only a small fraction enters the aperture of the camera and is imaged on the film. Therefore, with parallel illumination, drops photographed as black spots on a white background and nothing could be learned about the processes in the interior of the drop.

The solution of this problem was the use of a source of very diffuse illumination behind the drop. This is not as efficient a use

of the available light as parallel illumination but it does permit photography of the interior of the drop. Initially, Xenon flash lamps behind ground glass diffusers (Figure 2.4) were used for illumination but it was found that there was considerable blur in the image due to the intrinsic long duration of the flash (5-10 μsec). However, some results of this preliminary method are unique and are briefly discussed in Chapter 3.

To obtain a short duration light pulse (< 1 μsec), the primary light source was changed to a high pressure (1 atmosphere) spark gap discharge. A conventional "point source" design used for shadowgraphy was extensively modified to increase repeatability, holdoff and light output. The final configuration utilized most of the light from a linear spark (0.25" long) between 2 hemispherical electrodes in an air/argon mixture (90%/10%). Typically the gap was operated at 7 kV (with a 0.1 μf capacitor this yields $\sim$ 2.5 J energy input per shot) with triggering through a tertiary electrode driven by a low inductance trigger transformer (EG&G). To be able to use conventional photographic film it proved necessary to collect and use as much of the light from the spark gap as possible. A reflector behind the spark and a collimator-condenser system were used to collect the light and focus it onto the entrance of a high efficiency diffuser. The diffuser was simply a section of tubing lined with a diffuse reflector (the dull side of Reynolds wrap), one end of which was closed except for an entrance slit and the other end covered by ground glass or lucite. A schematic of the basic arrangement is shown on Figure 2.5 together with the test section and cameras.

As shown in Figure 2.5 the drop could be photographed

simultaneously from two views using the transmitted light with camera A and the perpendicularly scattered light with camera B. Each camera was of the same type, a 4 x 5 format view camera with a 135 mm focal length lens, modified by attaching a 35 mm film transport in place of the usual sheet film holder. The lens-film distance was adjusted to give a magnification of two on the negative; for a typical f-number of 16 this gave an acceptable compromise between resolution and depth of field for the available illumination. A 35 mm roll type film was used instead of the usual sheet film for economy (the smallest images only occupied < 1% of even the 35 mm format) and convenience in camera operation and film processing. Kodak Tri-X (400 ASA) film was used in both cameras, for camera A the film was processed in Kodak Microdol-X developer using standard development time plus two minutes; for camera B the film was "push-processed" to a nominal 4000 ASA using a fine grain developer (ETHOL UFG). Aperture settings of each camera determined the exposure. For a particular spark gap-diffuser combination the correct settings would be determined by a series of test exposures at the different possible apertures.

The triggering signal used to fire the spark gap was derived from the pressure signal generated by the explosion itself. An inherent delay corresponding to the time required for the pressure signal to travel from the droplet to the transducer determined the earliest possible time any photographs could be taken (the smallest of these inherent delays was about 8 μsec corresponding to a path length of $\sim$ 5 mm). An auxillary oscilloscope connected in parallel with the pressure recording oscilloscope triggered a delay generator

immediately upon the appearance of the explosion pressure signal. The delay generator produced a signal a preset length of time following the trigger which fired the spark gap. Prior to the explosion (after the drop had been injected into the column), the room had been darkened and the camera shutters opened so that the film is exposed when the spark gap fires. Following the explosion the camera shutters are closed, the films advanced one frame and electronics reset in anticipation of the next explosion.

By reading off the time elapsed from the beginning of the pressure signal to the glitch on the pressure trace caused by electromagnetic noise from the spark gap circuitry and adding the drop-transducer acoustic transit time, a unique time could be assigned to every photograph. It is this time, the time elapsed since the pressure wave first left the drop, which is used to label all the photographs appearing in the present work.

2.5 Conditions in the Drop at the Time of the Explosion

As the droplet translates up the column, heat is constantly being transferred to the drop liquid from the host. This heat transfer takes place at a finite rate; hence the temperature in the interior of the drop lags behind the ambient temperature of the glycol. Further, the droplet liquid is circulating due to the shear stress on the surface of the drop that is generated by the translational flow field.

Both the circulation and finite rate of heat transfer are important in determining the final temperature field in the droplet at the time of the explosion. This problem is very complex for the range of conditions encountered in the bubble column and no general solution exists. In this section, the relevant physical parameters are pointed out and an estimate given for the temperature lag of the drop at the time of explosion.

Physically, the most important parameters in determining the heat transfer rate are the Reynolds number Re of the droplet translation, or equivalently the Peclet number $Pe = RePr$, and the viscosity ratio K, $K = \mu$ drop/μ host. Droplets rising up the column accelerate since the drag force decreases as the glycol temperature increases and its viscosity falls. Glycol viscosity rapidly decreases from a value of 60 cP at 0° C to 7 cP at 50° C and the final value in the test section is 2 cP at 100° C. In comparison the butane viscosity varies only slightly, from 0.2 cP at 0° C to 0.1 cP at 100° C.

Therefore, typically Re ranges from $\sim$ 0.1 at the bottom of the column to 50-200 in the test section (the range in the final Re corresponds to a range of 0.5-1.0 mm in drop radius). Those

Reynolds numbers were estimated from the terminal velocity correlation given in Clift et al (1978) and the measured temperatures along the centerline of the column.

At all times during the motion of the drop the butane viscosity is much smaller than that of glycol. Neglecting the possible influence of impurities in the glycol, this implies that the butane will be freely circulating inside the drop. Initially, when $Re \leq 1$, the creeping flow solution of Hadamard (discussed in Clift, et al 1978) will be valid and the maximum circulatory velocity will occur at the drop center and is $U/2$, where U is the translational velocity. As the drop rises and Re increases, the circulation pattern becomes more complex and its characteristic velocity decreases.

The heat transfer into the drop can be described in terms of an average Nusselt number Nu, which for large Re but laminar flow has the form $Nu \sim Re^{1/2}Pr^{1/3}$. To obtain some idea of what the temperature lag in the drop was, an ad hoc model of the heat transfer process was constructed:

a) Circulation within the drop was assumed to be sufficient to keep the drop fluid well mixed, so that the entire volume of the drop participated in the heat transfer simultaneously.

b) The Nusselt number was assumed to be constant and given by empirical formula for <u>solid</u> spheres (White 1974),

$$Nu_m = 2 + 0.3\ Pr^{1/3}Re^{0.6} \quad .$$

c) Assuming a constant Reynolds number and temperature gradient, the overall thermal energy balance,

$$\overline{q}A = C_p \frac{dT}{dt} \quad ,$$

into the drop was used to determine the drop temperature as a function of time.

Using the conditions characteristic of the test section, $\frac{dT}{dz} = 1.5^\circ$ C/cm and $U = 10$ cm/sec for a 0.5 mm radius drop, and the temperature lag is found to be $\sim 10^\circ$ C.

Obviously, this calculation is quite crude and the assumptions are rather drastic. Circulation is not that effective in keeping the drop temperature uniform and the transport of heat across the closed streamlines of laminar flow must occur by diffusion. Generally, the outer part of the drop and the core of circulation along the center-line will be hotter than the interior of the circulating regions.

Circulation, while difficult to properly treat, is nevertheless of utmost importance. If only diffusive transport is effective within the drop, then under the same conditions as used above the temperature lag in the interior of the drop would be $\sim 50^\circ$ C.

REFERENCES

Blander, M. and Katz, J. L. 1975 "Bubble Nucleation in Liquids", AIChE Journal 21, 833.

Clift, R., Grace, J.K. and Weber, M. E. 1978 Bubbles, Drops and Particles, Academic Press, New York.

Porteous, W. and Blander, M. 1975 "Limits of Superheat and Explosive Boiling of Light Hydrocarbons and Hydrocarbon Mixtures", AIChE Journal 21, 560.

Reid, R. C. 1978 "Superheated Liquids: A Laboratory Curiosity and, Possibly, an Industrial Curse", Chem. Eng. Ed. 12, 60.

Wakeshima, H. and Takata, K. 1958 "On the Limit of Superheat", J. Phys. Soc. Japan 13, 1398.

White, F. M. 1974 Viscous Fluid Flow, McGraw-Hill, New York.

TABLE 2.1

REPRESENTATIVE PHYSICAL PROPERTIES OF LIQUID ETHYLENE GLYCOL

Critical Temperature	T_c	372	°C
Boiling Temperature (1 Atm)	T_b	197.6	°C
Freezing Temperature (1 Atm)	T_f	-13	°C
Density (20° C)	ρ^{20}	1.11	g/cm^3
Specific Heat (20° C)	C_p^{20}	2.34	J/gm° C
Thermal Conductivity (20°C)	k^{20}	2.8×10^{-3}	W/cm° C
Viscosity (20° C)	μ^{20}	20.9	cP

TABLE 2.2

REPRESENTATIVE PHYSICAL PROPERTIES OF SATURATED N-BUTANE LIQUID

Critical Temperature	T_c	156	°C
Superheat Limit Temperature (1 Atm)	T_{SL}	105	°C
Boiling Temperature (1 Atm)	T_b	-0.5	°C
Freezing Temperature (1 Atm)	T_f	-138.3	°C
Density (20° C)	ρ^{20}	0.579	gm/cm^3
Specific Heat (20° C)	C_p^{20}	2.39	J/gm° C
Thermal Conductivity (20°C)	k^{20}	1.18×10^{-3}	W/cm° C
Viscosity (20° C)	μ^{20}	0.17	cP

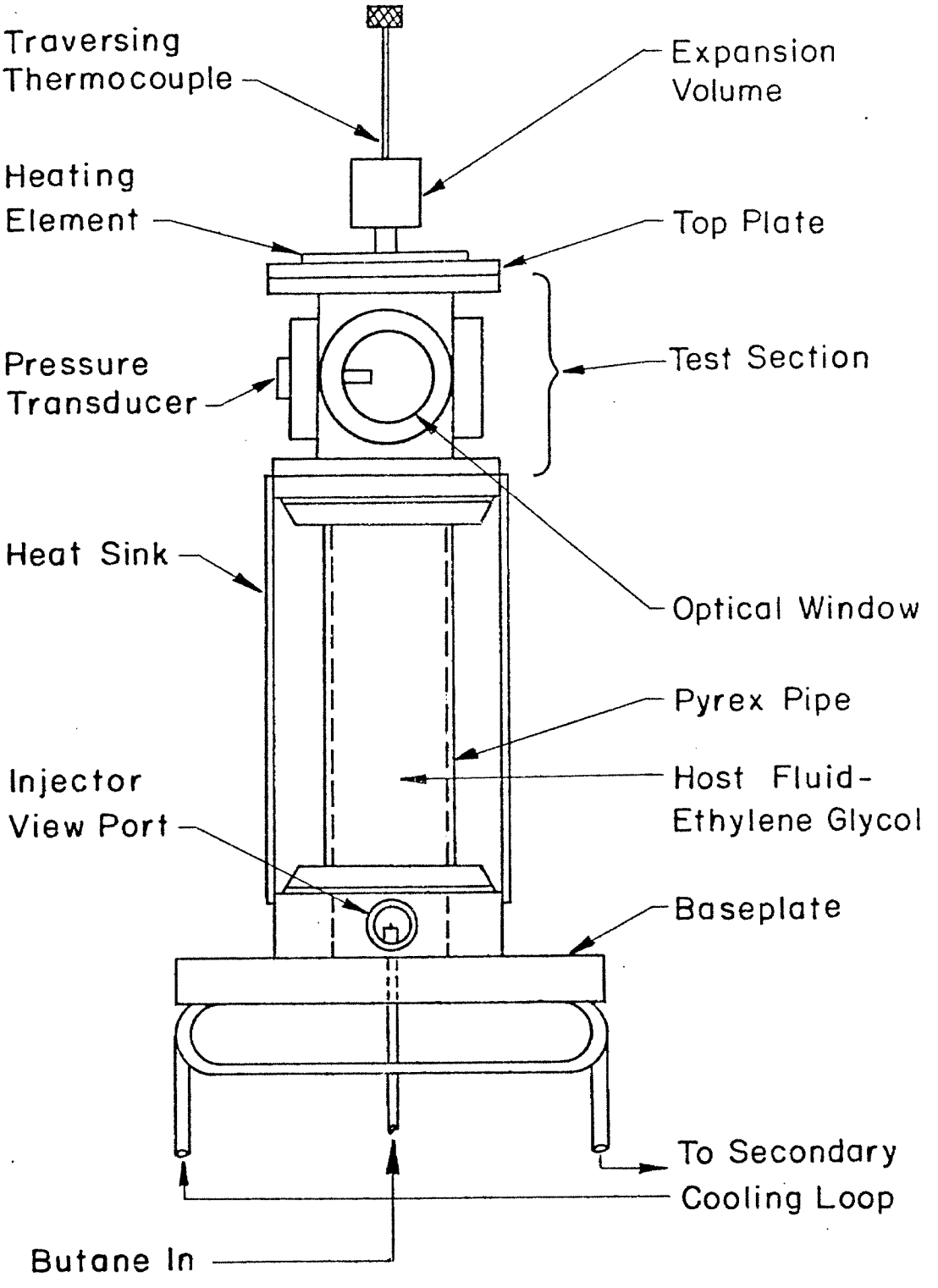

FIG. 2.1 BUBBLE COLUMN AND TEST SECTION

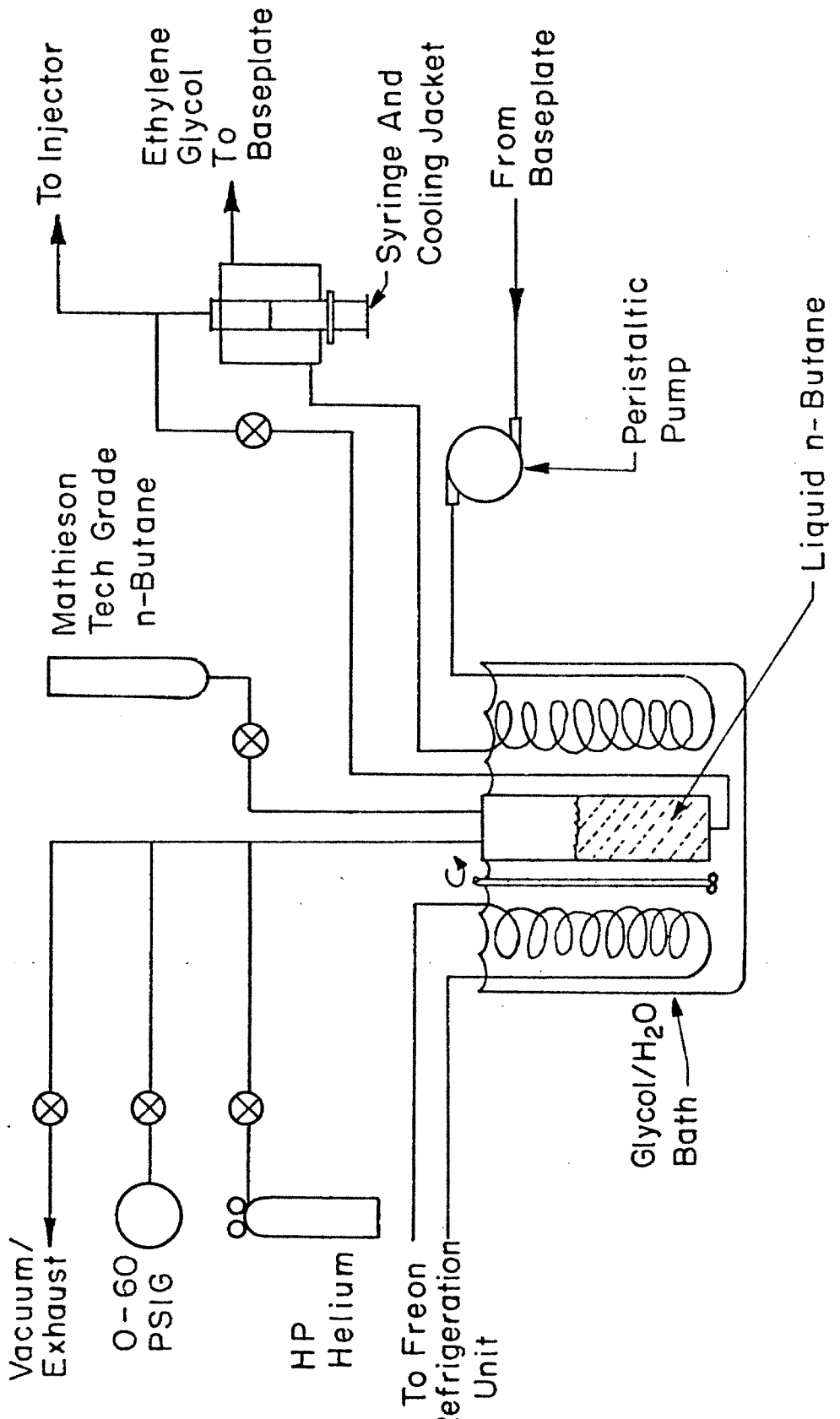

FIG. 2.2 REFRIGERATION AND BUTANE INJECTION SYSTEM

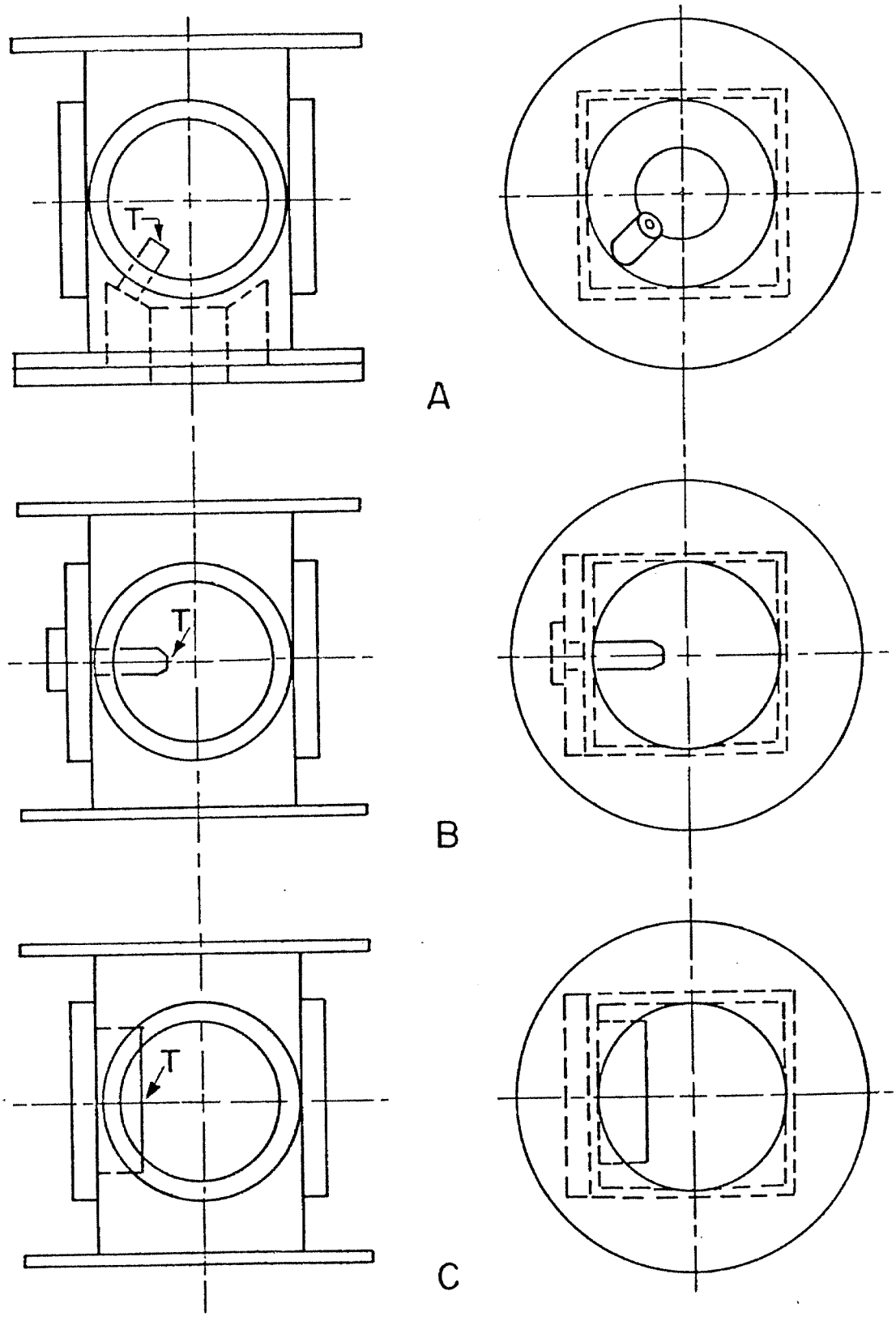

FIG. 2.3 TRANSDUCER LOCATIONS WITHIN THE TEST SECTION (T = TRANSDUCER FACE)

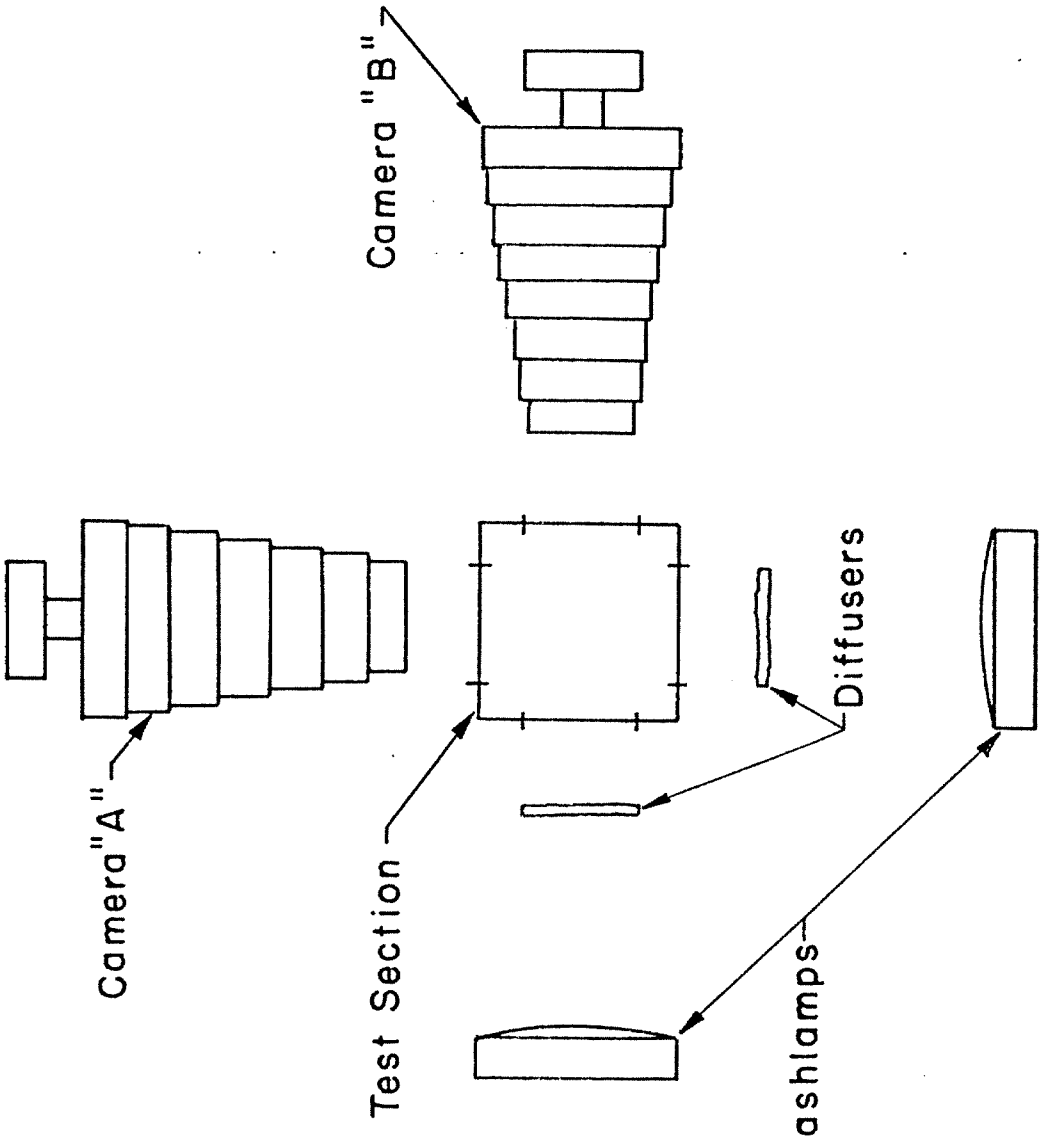

FIG. 2.4 PLAN VIEW OF APPARATUS FOR DUAL VIEW FLASHLAMP PHOTOGRAPHY

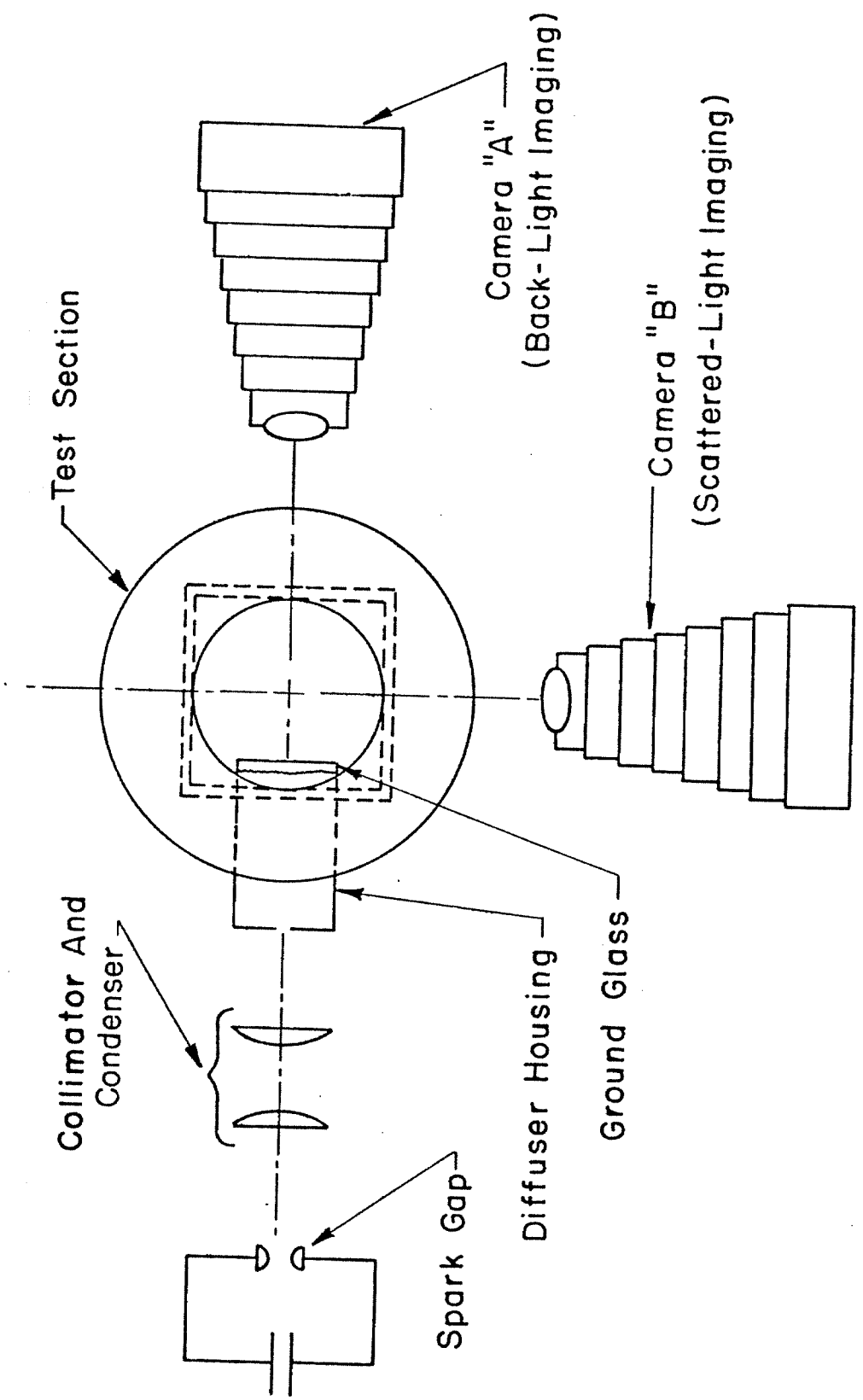

FIG. 2.5 DUAL VIEW SPARK GAP PHOTOGRAPHY SETUP

III. SURVEY OF OBSERVATIONS

3.1 Introduction

This chapter contains an exposition of selected photographs and pressure traces of individual explosions arranged to illustrate the general sequence of events and particularly interesting features discovered in the present investigation. It should be made clear that only one photograph (or two different views taken simultaneously) was taken for each explosion and that all the time sequences shown are composites, each print having been obtained from a different explosion.

A large catalog of individual explosions consisting of pressure traces and photographs taken at varying time delays was built up during the course of the experimental investigation. These records represented a large spectrum of drop sizes and delay times and were sorted into subsets according to the similarity of pressure traces, stage of explosion seen and presence of unusual features. Out of nearly 500 photographs approximately 70 were selected as being of best quality and greatest interest and are presented here. The majority of these selected prints are arranged in a series of 7 plates which form a photographic history of a "typical" explosion. All of the prints in this series represent explosions of comparable strength as determined by the similarity of the pressure traces.

This chapter is organized as follows: First, an overview of the results is illustrated by displaying selected prints from the main series in combination with a pressure trace on a single plate. Second, a detailed discussion of the explosion utilizing the main series of plates follows, and particular points are illustrated with additional plates. Third, a selection of pressure traces is presented demonstrating the effect of initial drop size and variety of time scales

characterizing the acoustic radiation.

3.2 Overview

An overview of the various stages in the explosion up to 2 msec is shown in Figure 3.1. The bar underneath each print indicates a scale of one mm (this is the convention used throughout; in Table 3.1 the experimental run number and delay times are given for the individual prints in each figure). Prints are in sequence of increasing time as though they were frames excerpted from a movie of a single droplet exploding.

The explosion begins 13 μsec before print (a) with the emission of the first pressure signal from a spontaneously created nucleus of vapor (the critical radius given by equation 1-2 is only 4 nm!). The bubble, which has grown from this nucleus, can be seen in print (a) located asymmetrically within the butane drop, which in turn, is surrounded by the host liquid (the background is the uniform diffuse light, which in most prints is pure white). The darkening at the edge of the drop and the light ring just inside are optical effects due to the strong scattering of light rays at grazing incidence, and a similar darkening of the bubble periphery can also be seen. Of particular note is the regular pattern seen on the bubble, suggestive of a wrinkled surface. This surface is the evaporating liquid-vapor interface of the growing vapor bubble and the idea that interface wrinkling is due to an evaporative instability is explored in Chapter 5.

As the bubble grows, a portion of its surface contacts the host liquid and thus becomes nonevaporating. This relatively smooth nonevaporating surface can be seen bulging out of the drop at the top in

print (b) (56 μsec). Other views of the bulge more clearly show a unique axisymmetric wave-like structure, the nodes appearing in some cases to be very sharp corners (one such node can be seen in print (b)). Simultaneously, the evaporating interface had developed a very rough appearance and scatters light strongly so that the bubble appears black. The non-evaporating interface spreads over the surface of the drop as evaporation proceeds and in print (c) (88 μsec) the roughness of the evaporating interface can be seen still imprinted on this surface. In print (c), only a small amount of the butane in the drop is still liquid and appears as a lighter crescent-shaped area at the bottom of the drop.

When the liquid butane has been completely evaporated (occurring between 40-160 μsec depending on the initial drop size), the resulting gas bubble is at a higher pressure than ambient due to the nonequilibrium nature of the evaporation process and so continues to expand. Surface disturbances prominent in print (c) smooth out during the expansion process and result in the smooth bubble seen in print (d) (610 μsec). Due to the large difference between the indices of refraction of the vapor and liquid the bubble appears black except for a centrally located white spot of transmitted light. At this point, the bubble has actually overexpanded to a pressure less than ambient due to the inertia of the surrounding fluid and begins to collapse. As the gas inside the bubble is compressed, ultimately halting the collapse, the light vapor is accelerated into the heavier host fluid, a Taylor-unstable motion. Surface distortions induced by this instability at the maximum radius of the oscillation give the bubble the dramatic appearance in print (e) (1.05 msec).

This instability is catastrophic in that the bubble never recovers the smooth surface seen at the first volume maximum (print (d)). As

the bubble re-expands from the first minimum, the surface distortions change scale as seen in print (f) (1.5 msec). The bubble continues to oscillate in volume and Taylor instability at successive minima progressively breaks down the bubble surface to produce smaller bubbles. In all experiments the final state visible to the human observer is a cloud of small bubbles rising toward the surface of the host liquid.

The pressure trace shown in Figure 3.1 was obtained from a transducer 2.5 cm from the drop (configuration C of Figure 2.3). Letters labeling particular points on the pressure trace refer to the previously discussed photographs on this figure and show the stage of the explosion occurring at that time.

The initial pressure rise (between a and c on Figure 3.1) is due to the evaporation process. Increasing pressure in the vapor bubble and displacement of surrounding fluid by the specific volume increase in the liquid-vapor transition results in the radiation of compression waves. The broad peak just after point c corresponds to the completion of the evaporation process. While still expanding, the surface of the gas bubble is decelerating and radiating expansion waves into the surrounding liquid, so the pressure falls. At the maximum volume (point d), the minimum pressure occurs. As the bubble collapses, the gas inside compresses and radiates compression waves, so the pressure rises to a peak at minimum volume (point e). Continuing to oscillate in volume, the bubble radiates pulses at the minima, the oscillations diminishing in amplitude as its energy is radiated away and otherwise dissipated, and as disintegration into smaller bubbles occurs.

3.3 Detailed Discussion

The main series of plates is presented as a group in Figures 3.2 - 3.8, arranged in order of increasing time. In Figure 3.9, the particular stage of the explosion covered by each plate is indicated on two representative pressure traces. Discussion of these plates is found in the succeeding sections of this chapter and serves as a framework for a more detailed exposition of various aspects of the explosion.

3.3.1 Nucleation and Initial Growth

The earliest stage at which the explosion has been photographed is ~ 8 μsec after the first pressure signal has left the drop. In this time, nucleation has occurred and from the microscopic nucleus, a bubble of ~ 200 μm diameter has grown. At large superheats this growth process is highly nonequilibrium and may possibly involve noncontinuum phenomena; the actual details are unknown. The only information obtained in the present experiment on this process is contained in the pressure signal, which at these times exhibits a characteristic "bumpy" structure that is remarkably repeatable from explosion to explosion. Examples of these pressure signals are presented in Section 3.4 and a detailed discussion of the implications of this structure and comparison to the predictions of the standard theory is found in Chapter 4.

Photographs taken at the earliest times (using transducer configuration B for triggering, Figure 2.3) are seen in plates 3.2 (main series) and 3.10 (somewhat smaller initial drop sizes). Two features stand out; first, all of the bubbles are very close to the drop surface and in many cases (prints (c)-(f) of Figure 3.2) a small bulge can be

seen protruding out of the drop; second, the bubble surface appears wrinkled, in some cases regularly and in others with a spectrum of length scales.

The appearance of bubbles so close to and in many cases interacting with the drop surface raises the inevitable question: Is the nucleation truly homogeneous? It is reasonable that bubbles should form close to the drop surface since there is a hot thermal layer in the outer part of the drop (as discussed in Section 2.5) and the nucleation rate is strongly dependent on temperature. Unfortunately, because no bubbles younger than 8 μsec could be observed in these experiments, all observed bubbles were of finite radius and it was impossible to determine definitely whether nuclei formed within or on the surface of the drop. Whether the nucleus actually forms on the surface or in the interior of the drop depends on the relative size of the interfacial forces acting on the emerging nucleus. Jarvis et al (1975) in an amplification of an idea of Moore (1959) have delineated three mechanisms of nucleation for superheated droplets immersed in a host liquid. These three mechanisms are depicted in Figure 3.12: a) homogeneous nucleation, occurring when the droplet liquid wets (spreads on) the host; b) surface nucleation, occurring when neither host nor droplet liquid wets the other; c) "bubble blowing", occurring when the host wets the droplet liquid. Jarvis et al measured the interfacial tensions at room temperature for a pentane droplet-ethylene glycol system and concluded from extrapolation to the superheat limit that nucleation would be homogeneous with a large margin left for error. Butane is very similar to pentane (they are adjacent members of the alkanes) and the interfacial tensions that are known for butane-

glycol are close enough to those of pentane-glycol to suggest that the same conclusion can be drawn in the present experiment.

There is conclusive evidence that in at least one case nucleation did occur in the interior of the drop; this was obtained in the course of experimenting with dual flash lamp photography. In Figure 3.11, four sets of prints are shown which are simultaneous views ("A" and "B") taken at right angles to one another; set (a) clearly shows a bubble completely within a drop. In summary, the evidence is strong that nucleation occurs in the interior of the drop near the surface and it is during the growth of the resulting bubble that interaction with the surface occurs (typically before 10 μsec has elapsed).

3.3.2 Developing Bubble Structure

As the bubble grows from the nucleus within the drop, evaporating and displacing the surrounding butane and host liquid, a complex and distinctive structure develops which is schematically indicated in Figure 3.13. The off-center location of the bubble results in a portion of the bubble surface closest to the drop surface contacting the host fluid and becoming nonevaporating before any other portion does so. This nonevaporating interface area grows axisymmetrically with time, its boundary (the triple intersection of host, butane liquid and vapor) taking, for a spherical drop, the form of a circle on the surface of the drop. The axis of symmetry passes through the original drop center, the centroid of the bubble and the point where the bubble surface first contacted the host. Random orientation of this axis (due to the random nature of nucleation) with respect to the camera results in a variety of perspectives on the developing bubble.

Circumferential bulges or waves culminating in a spherical cap

progressively appear on the nonevaporating surface as it covers the drop. The first stage in this process can be seen as the single protruding bulge present in many of the prints in Figures 3.2 and 3.10. Subsequent growth of the single bulge into a spherical cap and the addition of surrounding circumferential waves can be seen in all the prints of Figure 3.3; in particular, the cap is pointed directly at the viewer in print (e) and the symmetry of the waves is striking. Striking proof of how axisymmetric these features are is found in print sets (b), (c) and (d) of the dual flash lamp photographs in Figure 3.11; with a certain amount of effort the viewer can visualize the axis of symmetry and corresponding features on each print of each set. Print set (a) of the dual view spark gap photographs (Figure 3.23), also vividly shows these features.

Once the basic structure of the developing bubbles was determined, some highly unusual appearing explosions could be recognized as merely peculiar perspectives of the standard configuration. The best example is a series of prints seen in Figure 3.14 which shows the development of the bubble from the back side; that is, the cap is on the far surface of the drop from the viewer and only its outline is seen through the evaporating interface as a definite ring.

A certain amount of variation of the basic nonevaporating structure exists between individual explosions. Examples of this are seen most clearly in the later stages of evaporation in Figure 3.4; prints (b) and (d) show the cap and several annuli facing the viewer while (a), (c), (e) and (f) show profile views. In these views, an area of irregular wrinkling of the nonevaporating bubble surface above its boundary (Figure 3.13) can also be seen; this is a result of the

evaporating interface wrinkling which will be discussed in connection with that phenomenon. The cap is indistinct in print (e) and no annuli are visible; in contrast, print (f) shows very clear and sharp edged annuli surrounding a prominent spherical cap; prints (a) and (c) represent intermediate cases. Two of the most plausible causes of this individual variation are: random variations of the nucleus' distance from the drop surface and the dynamic nature (i.e. traveling waves or oscillating standing waves) of the surface disturbances. To actually pinpoint the mechanism, it would be necessary to take very high speed (microsecond framing rates) movies of individual explosions.

Peculiar bubble shapes and surface waves have been seen previously in studies of cavitation bubble collapse (Ellis, 1965) and interacting bubbles (Hooper et al, 1970), but in the present context this phenomenon is completely unexpected and rather bizarre in appearance. It is conjectured that the surface distortions and the protrusion into the host liquid are both driven by the "jet" of evaporated vapor coming from the opposing interface and impinging on the nonevaporating interface. Thus, the appearance of surface disturbances should be modeled by the start-up of a gas jet into a liquid; some exploratory flow visualization in a simple apparatus verified this and is described in Appendix B. However, the phenomenon is not completely understood and the similarity of the two flows may be superficial.

3.3.3 Structure of the Evaporating Interface

The unusual shape of the nonevaporating bubble surface is interesting, but a much more important discovery is the tremendous wrinkling and extreme roughness of the evaporative interface. This wrinkling begins on the smooth and spherical interfaces of the

earliest stages as a rather regular pattern covering the entire bubble (prints (a) and (b) of Figure 3.2; prints (a), (b) and (c) of Figure 3.10). At the same time that the bubble is interacting with the drop surface, the regular pattern is developing into a larger scale folding of the surface (prints (c), (d), (e) and (f) of Figure 3.2; prints (e) and (f) of Figure 3.10). Very rapidly (within $\sim$ 5 μsec) the evaporating surface becomes roughened to the extent that light no longer passes through, resulting in the opaque bubbles seen in Figure 3.3. This rapid transition from regular wrinkling suggests the presence of a fluid dynamic instability driven by evaporation and manifested by distortion of the interface. Further development of this idea is found in Chapter 5.

Fuzzy outlines of the evaporating bubble surface (Figure 3.3) and the grainy appearance of the interface in the back views (Figure 3.14) demonstrate the extent of the disruption of the interface. Photographs of perpendicularly scattered light show that the evaporating interface is an extremely good diffuse reflector, an idea consistent with the presence of fine scale roughening. As the bubble grows, the evaporating surface remains in the mean symmetrical, although at later times some large scale disturbances can be seen (prints (a), (e) and (f) of Figure 3.4). These large scale disturbances, along with a spectrum of other scales, can also be seen impressed on the nonevaporating surface between the boundary of the nonevaporating region and the more regular features near the axis of symmetry.

The overall impression is that, after a period of development, the wrinkling of the interface saturates and persists at a constant level for the remainder of the evaporation process. The persistent

roughening of the interface appears random in orientation and occurs on many length scales, suggesting a fundamental instability of the evaporation process. The significance of the roughening to the dynamics of the evaporation process lies in the tremendous increase of the effective area of the evaporating surface. This effective area increase yields a proportional increase in the evaporative mass flux per mean surface area. Calculations performed in Chapter 4 show that this mass flux is orders of magnitude larger than the standard diffusion-limited theory predicts. Analogous effects in other fluid dynamic contexts are well known, for example, the vastly greater effectiveness of turbulent over laminar mixing.

Disturbances on evaporating surfaces have been previously observed (Hickman 1972) and possible instabilities of evaporating interfaces have been previously proposed (Palmer 1976, Miller 1973). However, none of the previous observations of bubble growth have shown unstable evaporating interfaces; all of the growing vapor bubbles observed had smooth and regular surfaces. A list of these visualization studies and the experimental conditions in each is given in Table 3.2. Important points are that all of these experiments were done at very low superheats (none at or even near the superheat limit) and nucleation and growth occurred entirely in the bulk liquid. There have also been some investigations of slightly nonequilibrium droplet evaporation (Tochitani et al 1977, Simpson et al 1974) and bubble growth on electrically pulse heated wires (Faneuff et al 1958) which do not show any wrinkling or instability of the evaporating surface.

In comparison to all these previous visualizations, the present experiment is unique. The degree of superheat and consequently the

evaporative mass flux is much larger than in any of the experiments in Table 3.2. Therefore, it is not surprising that new phenomena should appear. Particularly, it is important to note that the present observations are completely different than those predicted by the mere extrapolation of the near-equilibrium results and theories. The extent of the generality of the present results needs to be verified in detail, but clearly, the present observations indicate that evaporation at the superheat limit can be much more complex than previously envisioned.

3.3.4 Summary of Evaporation Stage

The final disappearance of the liquid butane in the drop correlates very well with the occurrence of the first peak in the pressure signal. At this point, the evaporating interface appears to have consumed all the liquid butane and the obvious conclusion is that evaporation has ceased. However, the possibility also exists that the bubble still contains a liquid-vapor mixture at this time, and phase changes occur during the subsequent bubble oscillations. Unfortunately, the light passing through the bubble is strongly scattered due to the enormous difference of host and vapor indices of refraction and no information is available on this question. However, the pressure produced by the oscillating bubble strongly suggests that its contents are predominantly gaseous and this is the point of view taken throughout this discussion.

Examples of explosions near the end of the evaporative stage are shown in Figure 3.5; in prints (a), (b), (d) and (e), a small amount of butane liquid can still be seen in the drop. The characteristic cap and annular waves are visible in all these prints;

also distributed over the surface is a spectrum of more irregular disturbances originating on the roughened evaporating interface. All of these surface features appear "softer" than at earlier stages, indicating that the smoothing effect of surface-wave propagation has taken effect.

From nucleation to the final consumption of the liquid butane, the evaporation process is summarized in Figure 3.15. Outlines of the vapor bubble within the drop are shown (taken from actual photographs) at the various stages of the explosion. Evaporation begins at (a) with the creation of a nucleus near the drop surface; by the time 8 μsec has elapsed the nucleous has grown to a bubble of $\sim$ 200 μm diameter in (b). Interacting with the drop surface, the growing bubble displaces the surrounding fluid and develops its distinctive structure in (c), (d) and (e). Simultaneously, the characteristic wrinkled structure of the evaporating interface develops and persists for the remainder of the evaporation. Ultimately all the liquid butane is vaporized and only a gas bubble remains in (f).

3.3.5 Gas Bubble Oscillations and Breakup

Immediately following the cessation of evaporation, the gas bubble is at a net positive overpressure, a consequence of the dynamic (nonequilibrium) nature of the previous event, occurring in the evaporation process. Evaporation at the superheat limit occurs sufficiently rapidly that the increased pressure in the bubble can only be partially alleviated by volume expansion and acoustic radiation before the droplet is completely vaporized. The overpressure remaining in the bubble represents stored energy, which is then released during the subsequent oscillations of the gas bubble. A portion of

this energy is radiated away into the environment (the "ping" heard upon evaporation), the rest is dissipated through the creation of new bubble surface (Taylor instability), the viscous dissipation associated with the gas and host liquid motion and the process of thermally equilibrating the vapor with the host.

The fate of the oscillating bubble is determined by the coupling between volume oscillations and surface oscillations (capillary waves on the bubble surface), the spherical analog of the Taylor instability (Taylor 1950) for plane surfaces. This coupling results in amplification of small surface disturbances into drastic deformations, ultimately causing the breakup of the bubble. Some results of the linear stability theory of this coupling and the application to the freely oscillating bubbles, such as occur in the present work, are presented in Appendix C. In summary, growth is stabilizing, collapse destabilizing and the most unstable region is near the minimum radius (Taylor instability). Furthermore, in the spherical case the possibility arises of algebraic growth, a behavior which does not occur in the plane case.

Initial surface distortions are damped out as the bubble expands (Figure 3.6), at the maximum radius (print (e)) only an evenly distributed small amplitude modulation ("orange peel") remains. As the bubble collapses (Figure 3.7) toward the minimum radius, the first distortions seen (print (a)) are already in the nonlinear stage. At the minimum radius, the tremendous outwardly directed acceleration (on the order of 10^4g! C.f. 50 g in the original experiments on the Taylor instability (Lewis 1950)) on the interface produces the convoluted surface seen in print (b). Rebounding from the minimum,

(print (c)), the bubble stretches its surface, the scale of the deformations correspondingly increases and the number of nodes decreases. Away from the minimum, expansion of the bubble has a stabilizing effect on small surface disturbances. However, the deformations have developed to such an extent (prints (d), (e) and (f)) that this has little influence and the smooth surface of the first maximum is never recovered.

Although the bubble is quite deformed after passing through the first minimum, it continues to oscillate in volume. These volume oscillations are confirmed by the extinction meter measurements described in Appendix A and the bubble pulses radiated at the minima (in comparison, the surface deformations contribute very little to the acoustic emission). The selection of prints in Figure 3.8 reveals the highly complex and nonlinear shapes the bubble surface assumes. After several cycles of oscillation, distinct smaller bubbles can be seen (prints (e) and (f)) pinching off from the original bubble. The destructiveness of the surface instability is quite evident in Figure 3.16. These five pictures and the pressure trace are representative of smaller initial drop sizes than seen in Figure 3.8. Deformations appear to be even more drastic, and in two cases (prints (d) and (e)), the bubble has disintegrated altogether. Finally, a completely different appreciation of the deformed bubbles is obtained from the image of the scattered light. In Figure 3.17, print sets (b), (c) and (d) show simultaneous views of the transmitted (white background) and scattered light (dark background).

Bubble oscillations and surface instabilities have been extensively studied in recent years (e.g. Plesset and Prosperetti 1977)

and the phenomena seen in the present experiment contribute nothing fundamentally new to this field. In particular, the instability of an oscillating gas bubble has been previously observed in underwater explosions (Cole 1948), cavitation research (Benjamin and Ellis 1966, Lauterborn 1974) and acoustically driven bubbles (Kornfeld and Suvorov 1944, Hullin 1977).

However, the oscillating gas bubbles produced by droplet vapor explosions are unique. The bubble is filled with an inert gas, unlike the vacuous bubbles of cavitation or the high temperature bubbles of underwater explosions, and the radial oscillation amplitude is large so that the results are dramatic, but the minimum bubble radius is not so small that the interesting events which occur there cannot be observed (a problem typical of cavitation bubbles). This combination of ideal circumstances in the present experiment has resulted in particularly good photographs of the instability which show much more detail than previous work.

There has been one previously published photographic investigation of the oscillating bubbles resulting from droplet vapor explosions. Apfel and Harbison (1975) took movies at a framing rate of 3500/sec of the superheat limit explosion of an ether droplet suspended in glycerin. The actual evaporation process was not resolved, since the framing rate of the camera was too low, but the resulting bubble oscillations and instability upon bubble collapse were observed. Overall, these observations are consistent with those of the present work, but it is difficult to judge from their published photographs whether the details of the instability are the same.

3.4 Pressure Signals

Each explosion emits a distinctive and unique pressure signal. No two are exactly the same in detail, but there is an obvious similarity of form; yet systematic differences occur between individual explosions. Orientation of the bubble, its location within the drop and the unsteady nature of bubble growth are uncontrollable factors which produce unsystematic differences during the early stages of explosion. During the later stages, the unsteady motion associated with the instability of the oscillating gas bubble produces even more unsystematic variations (this effect is also pointed out by Cole (1948)). Variations in drop size and drop-transducer orientation produce systematic differences in pressure signals. Despite these individual differences, all pressure signals show the initial rise due to evaporation and the succeeding pulses from gas bubble oscillations.

There are several characteristic time scales on which there is significant structure in the pressure signal. The smallest of these are the first 10-20 μsec associated with the development of the vapor bubble and its evaporating surface. Intermediate time scales are the duration, 40-160 μsec, of the evaporative stage and the interval, 0.3-1.2 msec, between the subsequent bubble pulses produced by the volume oscillations. The longest time scale present in the signal, 3-10 msec, characterizes the decay in bubble-pulse peak amplitude that is due to the damping of the volume oscillations. Examples of pressure signals, measured $\sim$ 2.5 cm from the explosion with transducer configuration C, Figure 2.5, are shown in Figures 3.18, 3.19, 3.21 and 3.23. Each of these figures illustrates the effect of initial drop size on the pressure signal for one of the characteristic time intervals listed above.

Figure 3.18 compares pressure signals measured during the initial 50 μsec of 3 different explosions. In all 3 cases, the signal begins with a characteristic two-step structure followed by a generally monotonic increase, on which may be superimposed a nonrepeatable oscillation.

Initial steps or peaks in the first 10-15 μsec are a feature of almost every pressure signal measured in the present study and seem to be reasonably independent of the initial drop size. The universality of this intriguing characteristic signal suggests a fundamental and repeatable unsteadiness in the nucleation and bubble development taking place at this time. A quantitative investigation of this possibility is undertaken in Chapter 4.

In Figure 3.19, pressure signals from 4 different explosions are compared over the entire evaporative stage, including in some cases the end of evaporation and the resulting gas bubble expansion. The size of the initial drop, decreasing from trace (a) to trace (d), affects both the scale and details of the pressure signal produced during evaporation. The most obvious effect is that larger drops require a longer time to completely evaporate and produce a higher ultimate pressure. A quantitative expression of this correlation between evaporation time and ultimate pressure is shown in Figure 3.20 for 46 different explosions. Fundamentally, both of these quantities must depend on the initial drop diameter. However, this dependence was not determined in the present investigation. More subtle is the effect on the characteristic initial structure, which is generally more prominent for smaller drops (e.g. trace (d)) than larger ones (e.g. trace (a)). Possibly, this is due to the reflection, at the interface

of the glycol and remaining liquid butane, of the pressure signal produced by the growing bubble. Such an effect, discussed further in Section 4.2, would only be important for the earliest stages of bubble growth and would affect a greater portion of the initial signal as the initial drop size was increased.

Figure 3.21 compares pressure signals measured over the first 2 msec of 3 different explosions. Both the initial pressure increase due to evaporation and the succeeding bubble pulses due to volume oscillation can be seen in all traces. Spikes on the signals (also seen in Figure 3.23) at 1.05 msec are the record of the electromagnetic noise produced by the spark gap used in the photography. Initial drop size decreases from trace (a) to trace (c). Larger drops produce larger gas bubbles and the bubble oscillation period increases with bubble volume. Therefore, the time interval between bubble pulses is an increasing function of initial drop size. This correlation is quantitatively expressed in Figure 3.22 by plotting the interval between the end of evaporation and the peak of the first bubble pulse vs. the length of the evaporative stage. Bubble-pulse peak amplitude is of the same order as the ultimate pressure produced in the evaporative stage. This is in sharp contrast to the case of underwater explosions produced by detonations; the initial pulse (shock wave) due to the detonation process has an amplitude many orders of magnitude larger than the following bubble-pulse peak amplitudes. Finally, the pressure pulses produced by the oscillating gas bubbles are not as clean and simple as the idealized theory would predict (e.g. trace (c) of Figure 3.2). Many of the smaller peaks, seen between the main pulses, are artifacts from secondary waves generated by reflection inside the

test section. Also, as mentioned previously, the instability of the oscillating bubble surface contributes to the irregular appearance of the signal.

The longest interval over which pressures were recorded was 10 msec. Examples of signals over this interval are shown in Figure 3.23. Smaller explosions (e.g., trace (c)) show a regular damping of the signal followed by a nearly constant amplitude oscillation. Larger explosions (traces (a) and (b)) show the same general damping but a more complex oscillatory signal, which suggests a superimposed oscillation in the mean test section pressure. Such an oscillation in the mean pressure could be due to the net displacement effect of the explosion exciting a low frequency response of the test section.

REFERENCES

Apfel, R. E. and Harbison, J. P. 1975 "Acoustically Induced Explosions of Superheated Droplets", J. Acous. Soc. Am. 57, 1371.

Benjamin, T. B. and Ellis, A. T. 1966 "The Collapse of Cavitation Bubbles and the Pressures Thereby Produced Against Solid Boundaries", Phil. Trans. Roy. Soc. A260, 221.

Cole, R. H. 1948 Underwater Explosions, Princeton University Press, Princeton, New Jersey.

Dergarabedian, P. 1953 "The Rate of Growth of Vapor Bubbles in Superheated Water", J. App. Mech. 20, 537.

Dergarabedian, P. 1960 "Observations on Bubble Growth in Various Superheated Liquids", J. Fluid Mech. 9, 40.

Ellis, A. T. 1965 "Parameters Affecting Cavitation and Some New Methods for Their Study", California Institute of Technology, Hydrodynamics Laboratory, Report No. E-115. 1.

Faneuff, C. E., McLean, E. A. and Scherrer, V. E. 1958 "Some Aspects of Surface Boiling", J. App. Phys. 29, 80.

Florshuetz, L. W., Henry, C. L. and Khan, A. Rashid 1969 "Growth Rates of Free Vapor Bubbles in Liquid at Uniform Superheats Under Normal and Zero Gravity Conditions", Int. J. Heat Mass Transfer 12, 1465.

Hewitt, H. C. and Parker, J. D. 1968 "Bubble Growth and Collapse in Liquid Nitrogen", J. Heat Transfer 90, 22.

Hickman, K. 1972 "Torpid Phenomena and Pump Oils", J. Vac. Sci. Tech. 9, 960.

Hooper, F. C., Eidlitz, A. and Faucher, G. 1970 "Bubble Growth and Pressure Relationships in the Flashing of Superheated Water", Vols. 1-3, Technical Publication 6904, University of Toronto, Department of Mechanical Engineering.

Hullin, C. 1977 "Stabilitäts grenze pulsierender Luftblasen in Wasser", Acustica 37, 64.

Kosky, P. G. 1968 "Bubble Growth Measurements in Uniformly Superheated Liquids", Chem. Eng. Sci. 23, 695.

Jarvis, T. J., Donohue, M. D. and Katz, J. L. 1975 "Bubble Nucleation Mechanisms of Liquid Droplets Superheated in Other Liquids", Journal of Colloid and Interface Science 50, 359.

Kornfeld, M. and Suvorov, L. 1944 "On the Destructive Action of Cavitation", J. App. Phys. 15, 495.

REFERENCES (Continued)

Lauterborn, W. 1974 "General and Basic Aspects of Cavitation", in Finite-Amplitude Wave Effects in Fluids, (ed. L. Bjørnø), IPC Science and Technology Press Inc., Surrey, England, 195.

Lewis, D. J. 1950 "The Instability of Liquid Surfaces when Accelerated in a Direction Perpendicular to Their Planes. II", Proc. Roy. Soc. A202, 81.

Miller, C. A. 1973 "Stability of Moving Surfaces in Fluid Systems with Heat and Mass Transport - II. Combined Effects of Transport and Density Difference Between Phases", AIChE Journal 19, 909.

Moore, G. R. 1959 "Vaporization of Superheated Drops in Liquids", AIChE Journal 5, 458.

Niino, M., Toda, S. and Egusa, T. 1973 "Experimental Investigation of Nucleation and Growth of a Single Bubble Using Laser Beam Heating", Heat Transfer Japanese Research 2, 26.

Palmer, J. 1976 "The Hydrodynamic Stability of Rapidly Evaporating Liquids at Reduced Pressure", J. Fluid Mech. 75, 487.

Plesset, M. S. and Prosperetti, A. 1977 "Bubble Dynamics and Cavitation" in Am. Rev. Fluid Mech. (ed. M. van Dyke, et al), Annual Reviews Inc., Palo Alto, California, 145.

Simpson, H. C., Beggs, G. C. and Nazir, M. 1974 "Evaporation of Butane Drops in Brine", Desalination 15, 11.

Taylor, G. I. 1950 "The Instability of Liquid Surfaces when Accelerated in a Direction Perpendicular to Their Planes. I", Proc. Roy. Soc. A201, 192.

Tochitani, Y., Mori, Y. H. and Komotori, K. 1977 "Vaporization of Single Liquid Drops in an Immiscible Liquid Part I: Forms and Motions of Vaporizing Drops", Warme-und Stoffubertragung 10, 51.

TABLE 3.1 PRINT IDENTIFICATION

Print # ; Delay Time

Figure No.	a	b	c	d	e	f	
3.2	5 3/14 9.0	13 3/14 11.8	14 3/21 8.8	8 3/21 11.6	4 3/14 ~11.0	15 3/21 9.0	(μs)
3.3	6 4/28 16.9	9 4/28 17.4	8 4/28 18.0	19 4/28 22.0	8 4/29 28.0	24 4/29 33.8	(μs)
3.4	4 3/23 51.0	5 3/15 51.0	1 3/23 55.0	8 3/23 53.0	2 3/23 52.0	12 3/7 65.0	(μs)
3.5	18 3/30 69.3	19 3/23 88.0	11 3/23 88.0	17 3/23 90.0	11 3/23 91.0	12 3/23 94.0	(μs)
3.6	32 3/15 174.0	37 3/15 173.0	2 3/16 309.0	3 3/16 305.0	11 3/16 615.0	2 3/31 1058.0	(μs)
3.7	4 3/31 1.06	3 3/31 1.06	10 3/31 1.06	2 4/8 1.5	11 4/8 1.5	15 4/8 2.0	(ms)
3.8	12 4/8 1.5	18 4/8 1.9	23 4/8 2.5	18 4/9 2.8	24 4/8 2.5	12 4/9 6.5	(ms)
4.5	27 4/29 16.4	12 4/28 20.2	18 4/28 24.0	17 4/28 28.5	21 4/29 32.5	20 4/29 39.6	(μs)
C.2	2 3/31 1.06	4 3/31 1.06	3 3/31 1.06	10 3/31 1.06			(ms)
C.3	2 4/8 1.5	15 4/8 2.0	23 4/8 2.5	18 4/9 2.8			(ms)

TABLE 3.1 PRINT IDENTIFICATION (Continued)

Print # ; Delay Time

Figure No.	a	b	c	d	e	f	
3.1	5 3/14 13.0 (μs)	1 3/23 56.0 (μs)	19 3/23 88.0 (μs)	11 3/16 610.0 (μs)	3 3/31 1.05 (ms)	2 4/8 1.5 (ms)	
3.10	2 3/22 8.3	14 3/14 9.0	3 3/14 9.0	16 3/21 9.0	11 3/14 9.0	3 3/21 9.0	(μs)
3.16	8 3/31 1.04	14 4/8 1.9	20 4/8 1.9	15 3/31 5.0	13 4/9 6.5		(ms)
3.23	18 3/30 69.3 (μs)	2 4/8 1.5 (ms)	24 4/8 2.5 (ms)	12 4/9 6.5 (ms)			
3.14	15 3/14 9.0	17 3/14 10.0	3 2/27 17.5	11 3/22 32.0	9 3/23 50.0	7 3/23 55.0	(μs)

TABLE 3.2

VAPOR BUBBLE GROWTH VISUALIZATION STUDIES IN SUPERHEATED LIQUIDS

Investigator	Camera Framing Rate (kHz)	Smallest Radius Recorded (μm)	Substance	Maximum Superheat (°C)	Method of Superheating
Dergarabedian (1953)	1	30-50	Water	5.3	Infrared Lamps
Dergarabedian (1960)	1	3	Water	5.3	Infrared Lamps
			Carbon tetrachloride	5.4	
			Benzene	5.4	
			Methanol	5.4	
			Ethanol	6.3	
Florshuetz et al (1969)	15	50-100	Water	3.9	Pressure Release
			Ethanol	4.9	
			Isopropanol	4.9	
Hooper et al (1969)	15	250	Water	16	Pressure Release
Hewitt and Parker (1968)	15	750	Nitrogen	3.6	Pressure Release
Kosky (1968)	10	1000	Water	36	Pressure Release
Niino et al (1973)	10	30	Acetone	14.3	Pressure Release and Pulsed Laser Initiation
Present Work	N/A	100	Butane	105	Bubble Column

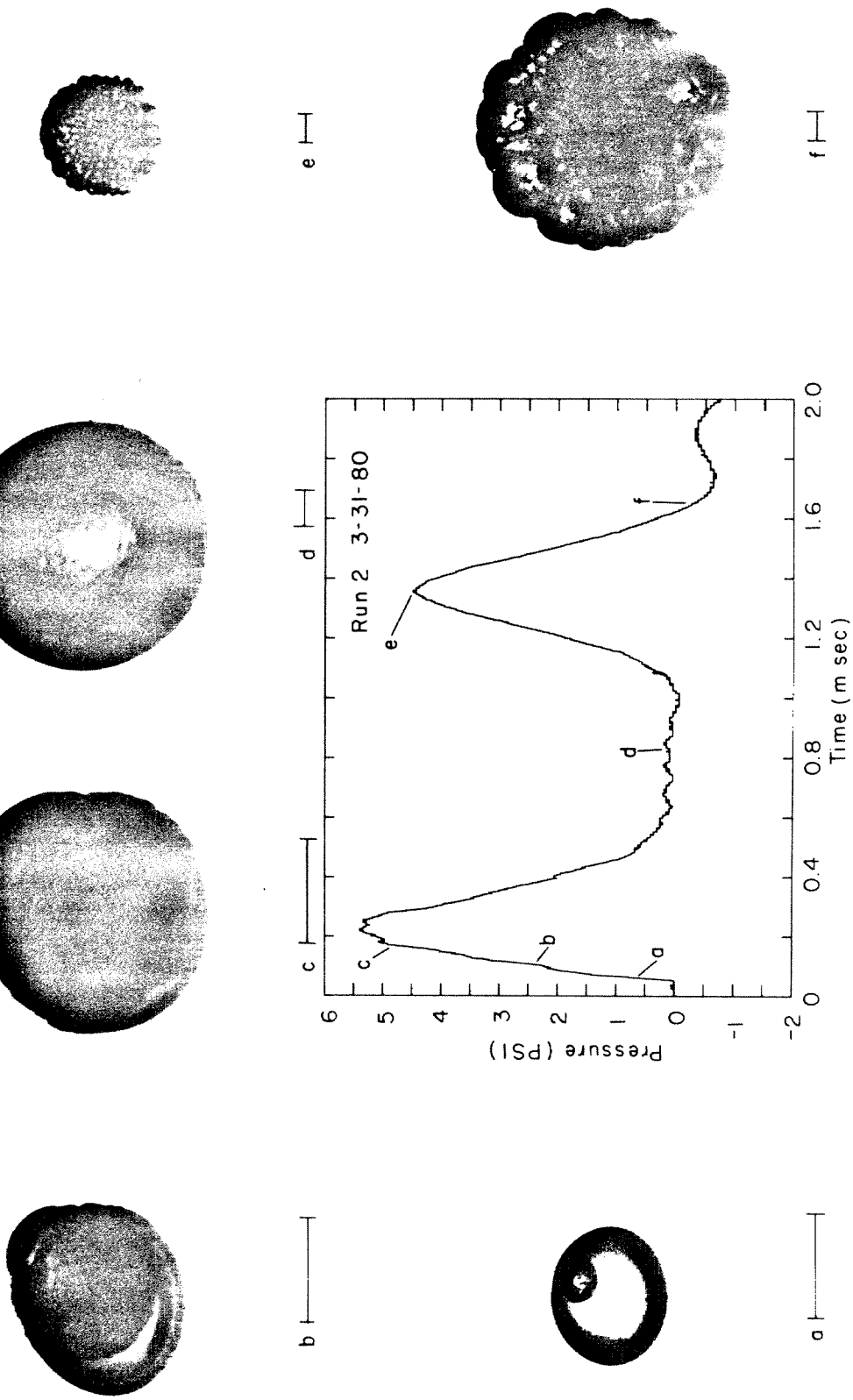

FIG. 3.1 OVERVIEW OF BUTANE DROPLET VAPOR EXPLOSIONS AT THE SUPERHEAT LIMIT.

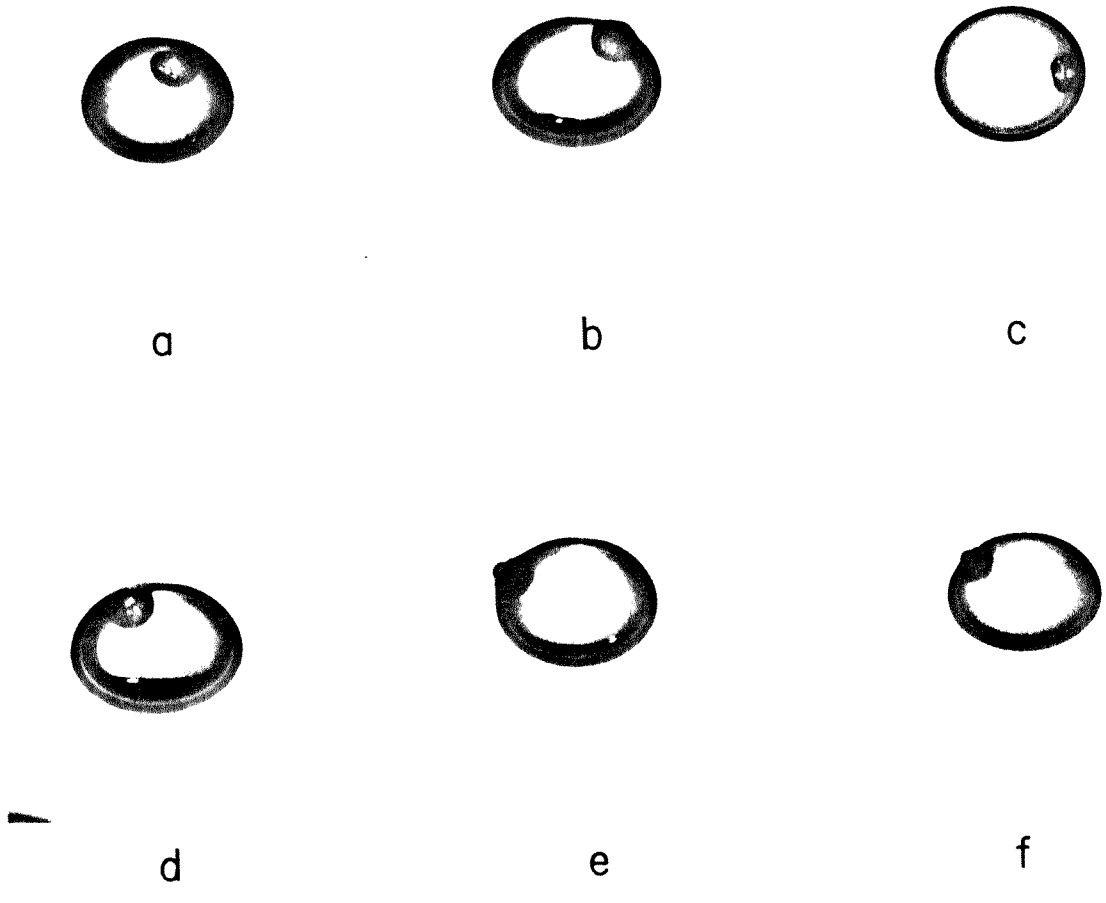

FIG. 3.2 VAPOR BUBBLES IN DROPS AT EARLIEST OBSERVED TIMES (9-12 μsec; ⊢——⊣, 1 mm).

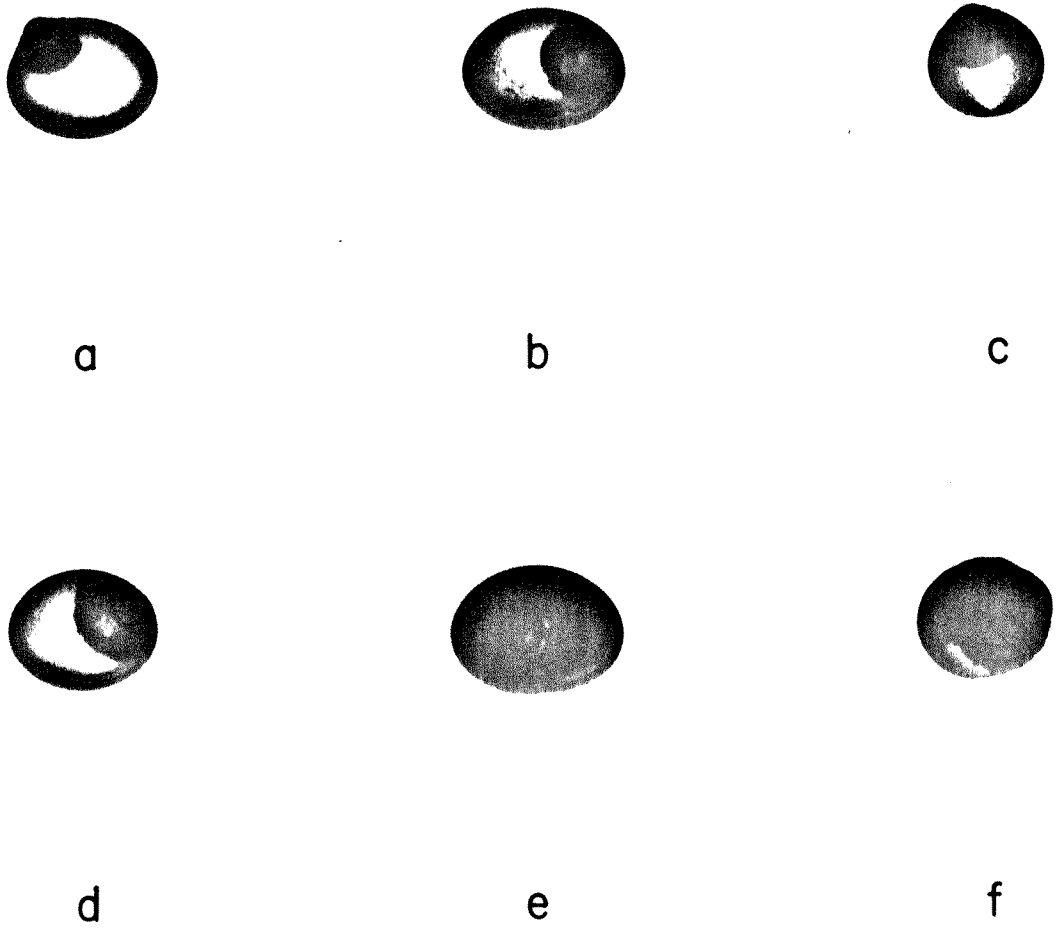

FIG. 3.3 GROWING VAPOR BUBBLES, SHOWING DEVELOPING JET STRUCTURE AND ROUGHENED EVAPORATING SURFACES (17-34 μsec; ⊢——⊣, 1 mm).

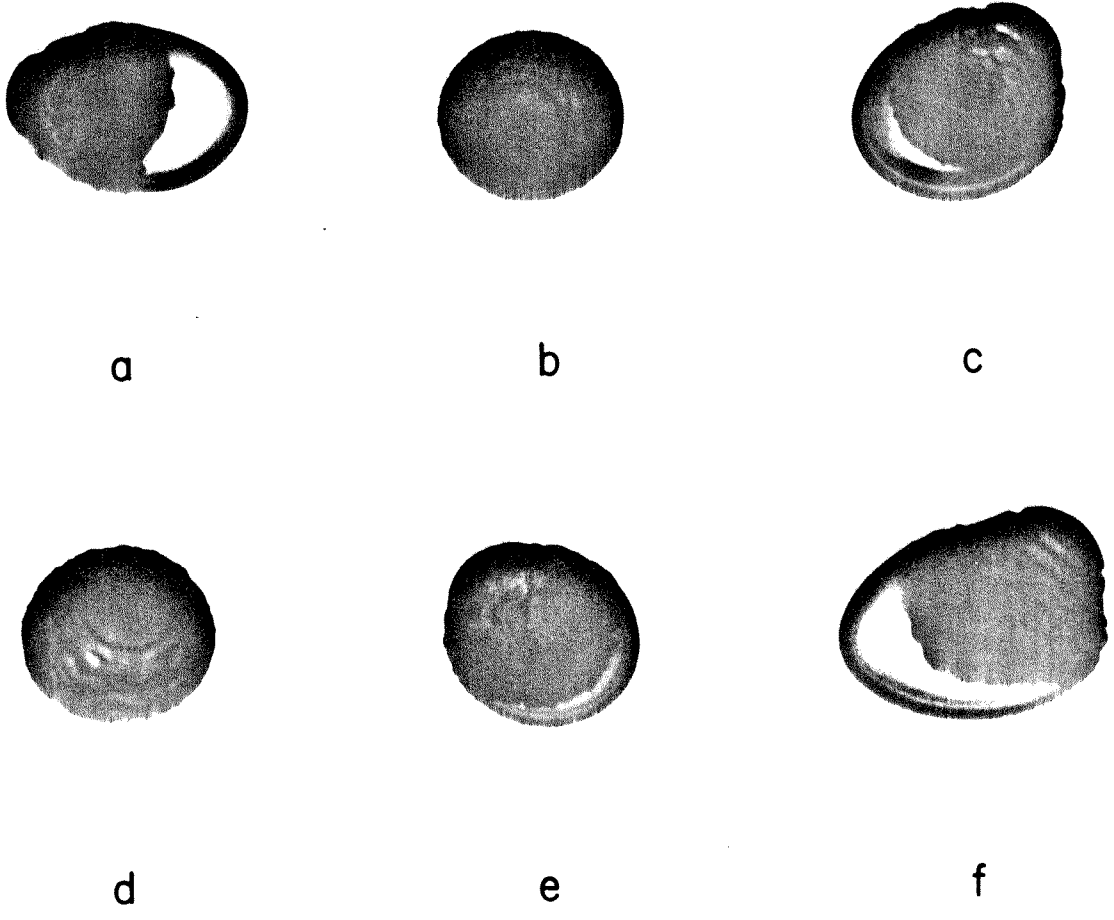

FIG. 3.4 FULLY DEVELOPED BUBBLES, SHOWING ROUGHENED EVAPORATING SURFACES, CIRCUMFERENTIAL WAVES AND REMAINING LIQUID BUTANE (55-65 μsec; ⊢——⊣, 1 mm).

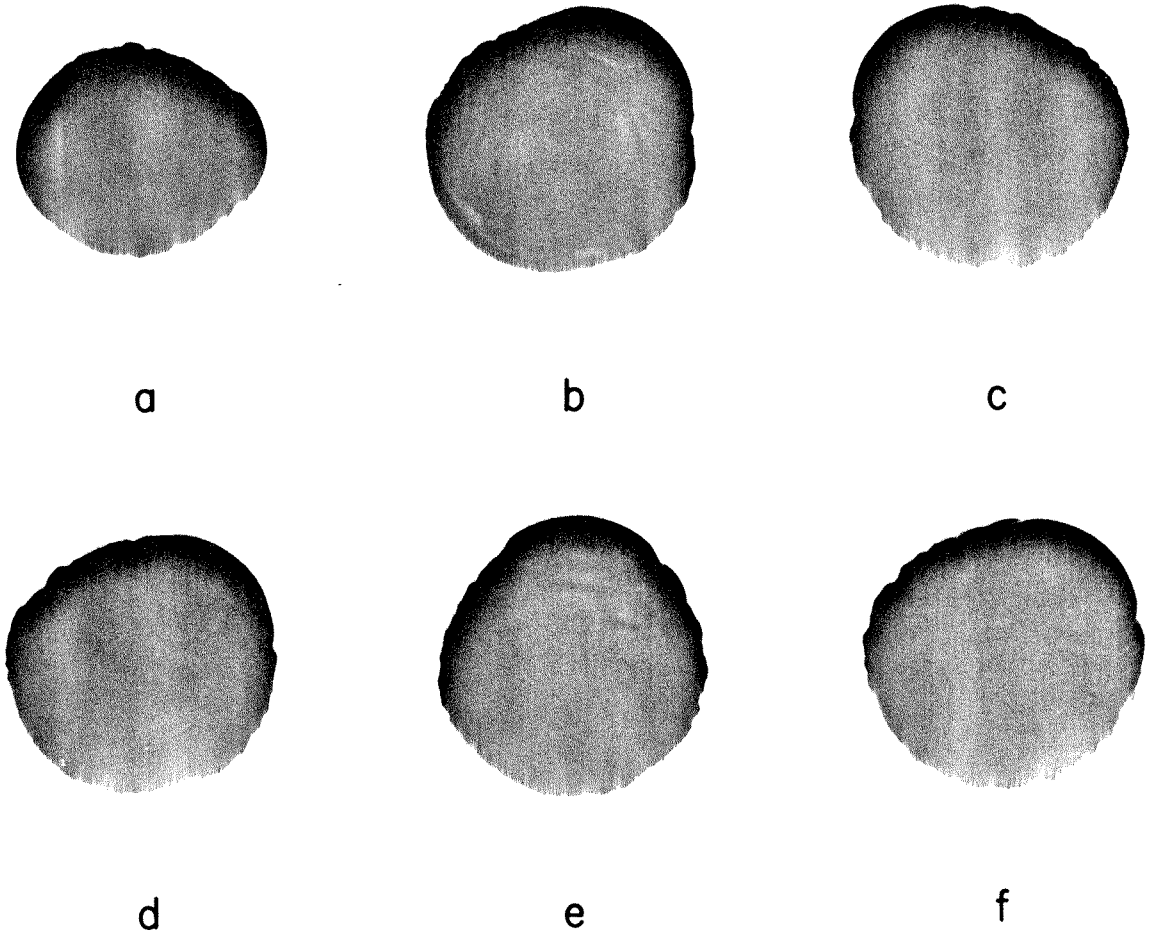

FIG. 3.5 BUBBLES AT OR NEAR THE END OF THE EVAPORATIVE STAGE (69-94 μsec; ⊢——⊣, 1 mm).

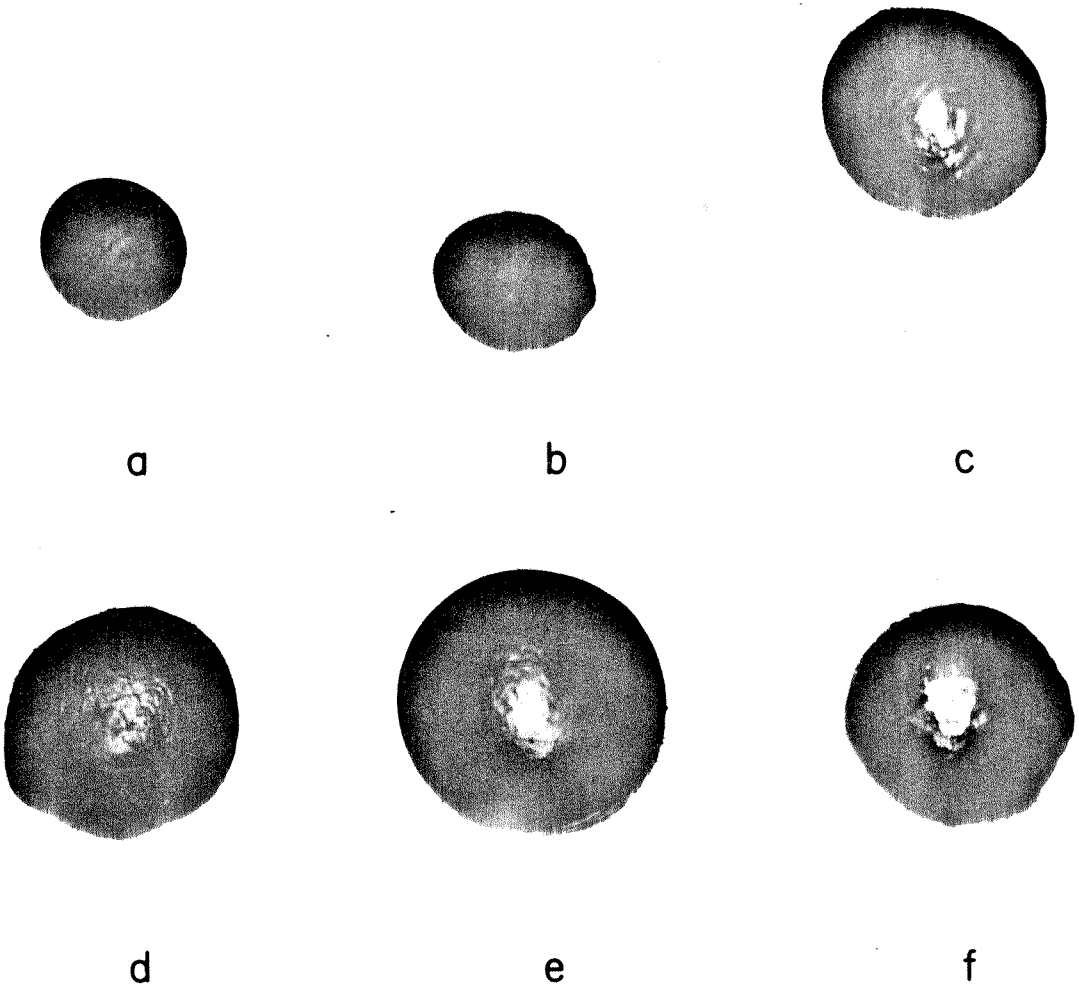

FIG. 3.6 NONEVAPORATING BUBBLE EXPANSION (a) - (d), FIRST VOLUME MAXIMUM (e) AND CONTRACTION (f) (.17-1.06 msec; ⊢⊣, 1mm).

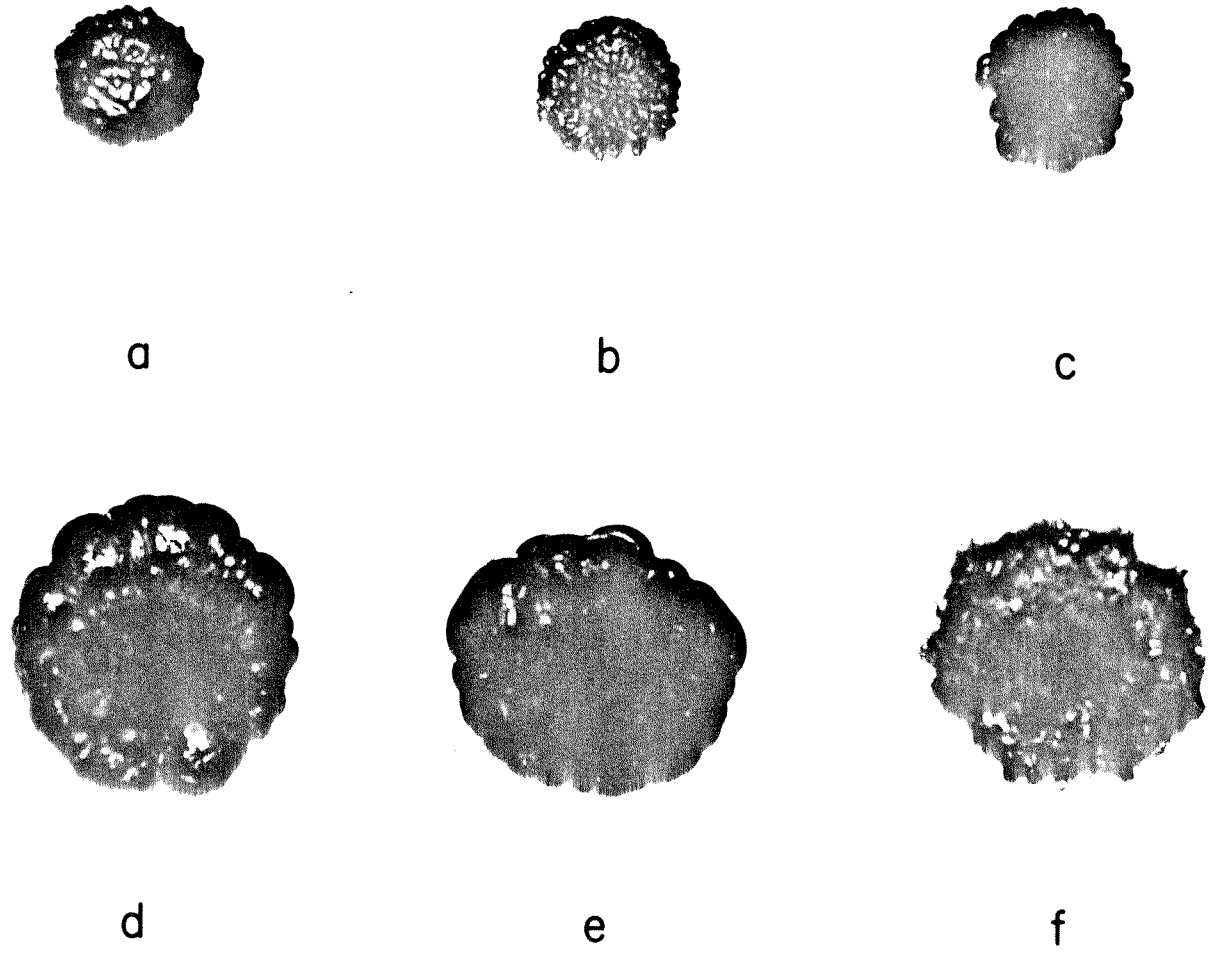

FIG. 3.7 INSTABILITY DEVELOPMENT BEFORE (a), AND AFTER (c) - (f) THE FIRST VOLUME MINIMUM (b) (1-2 msec; ⊢⊣, 1 mm).

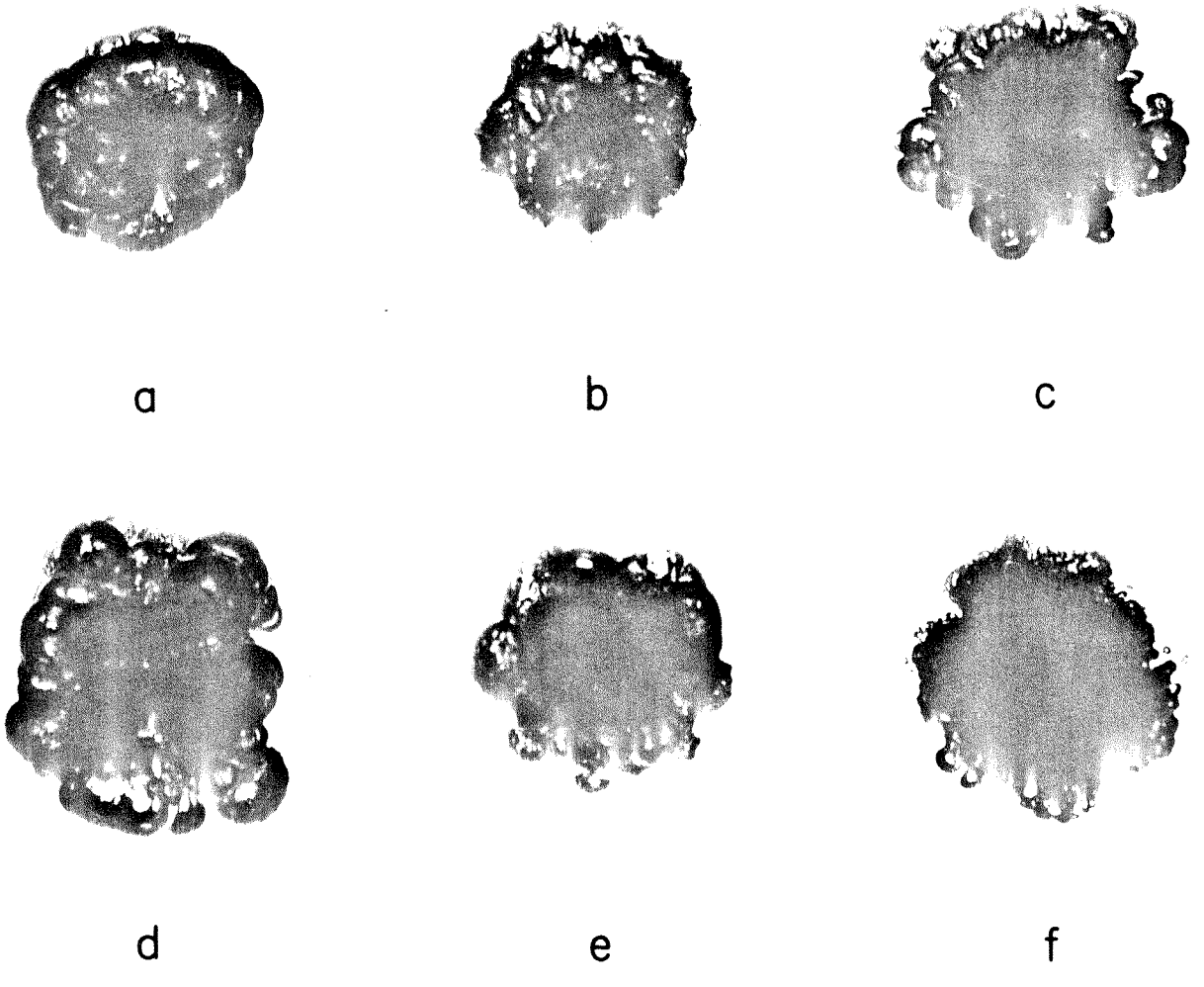

FIG. 3.8 BUBBLE OSCILLATION AND BREAKUP AFTER THE FIRST VOLUME MINIMUM (1.5-6.5 msec; ⊢⊣, 1 mm).

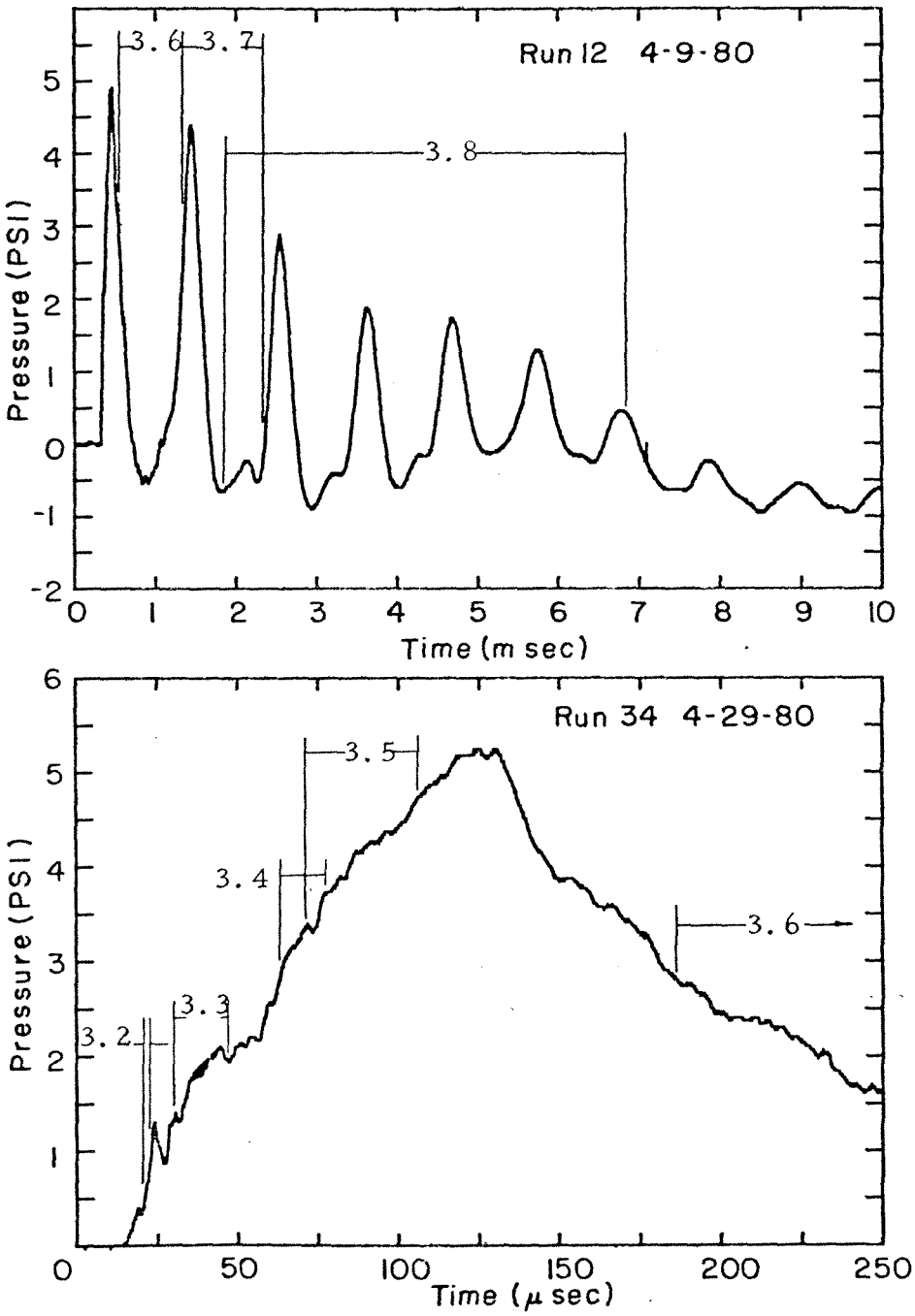

FIG. 3.9 TIME INTERVALS COVERED BY THE MAIN SERIES OF PRINTS, NUMBERS REFER TO THE FIGURES OF CHAPTER 3.

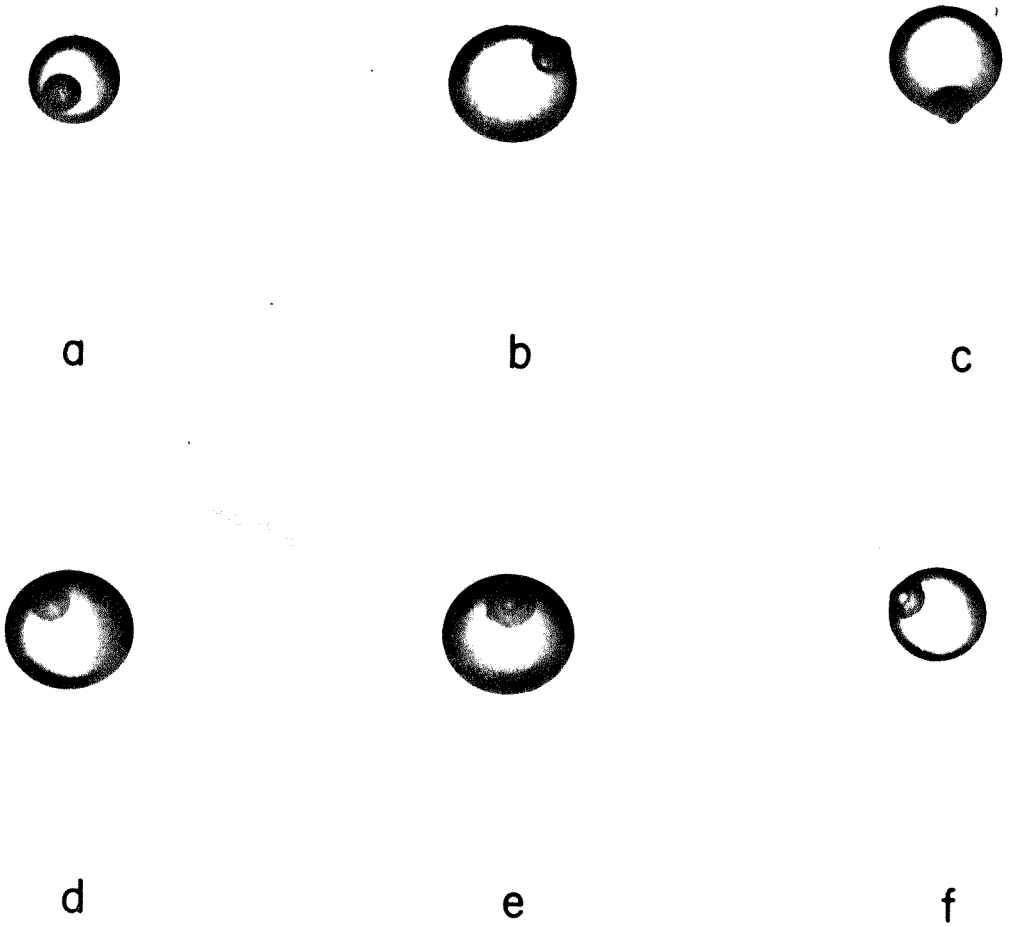

FIG. 3.10 VAPOR BUBBLES IN DROPS AT EARLIEST OBSERVED TIMES, SMALLER INITIAL DROPS (8-9 μsec; ├——┤, 1 mm).

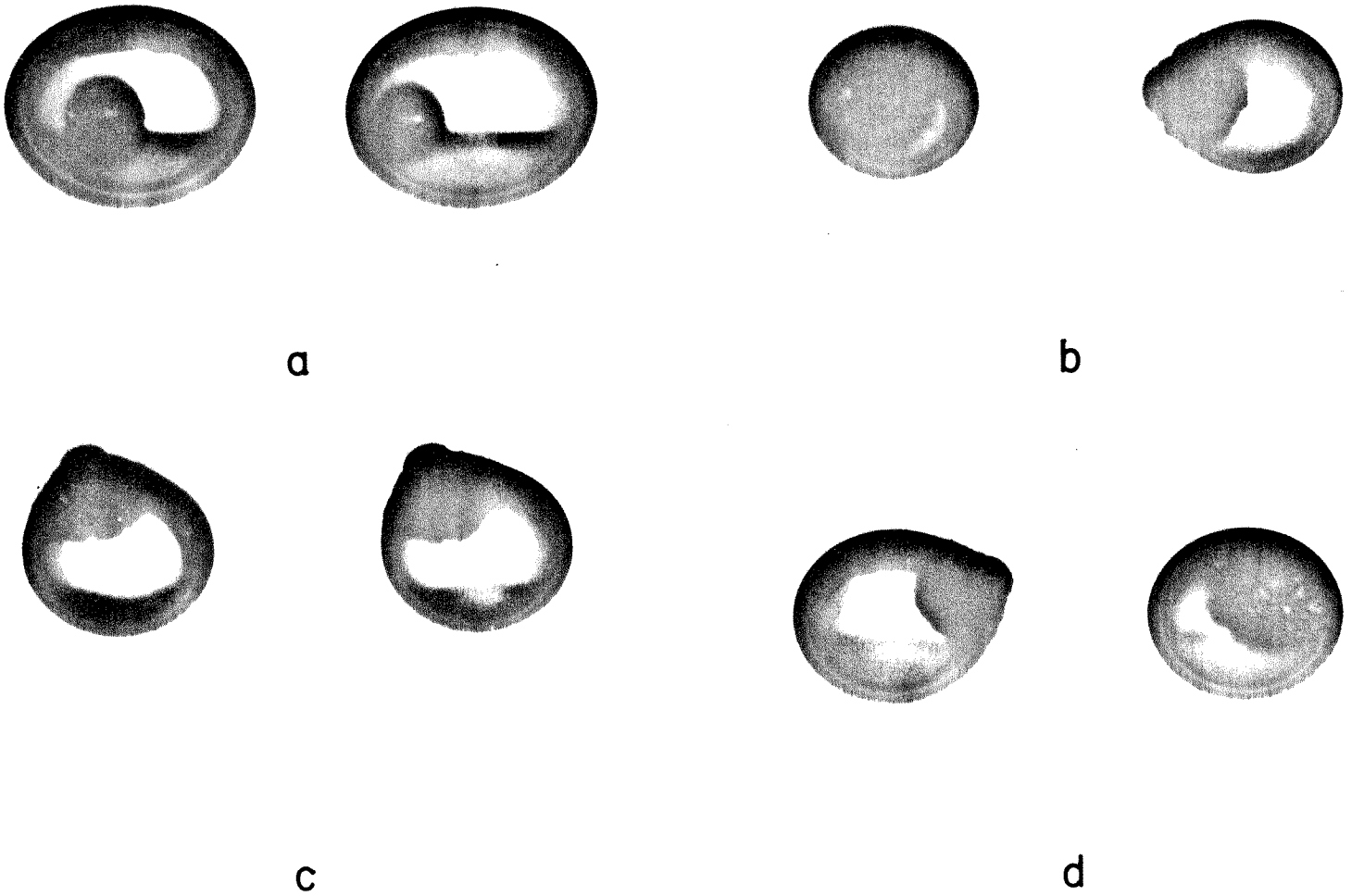

FIG. 3.11 DUAL VIEW FLASHLAMP PHOTOGRAPHS (⊢——⊣, 1mm.)

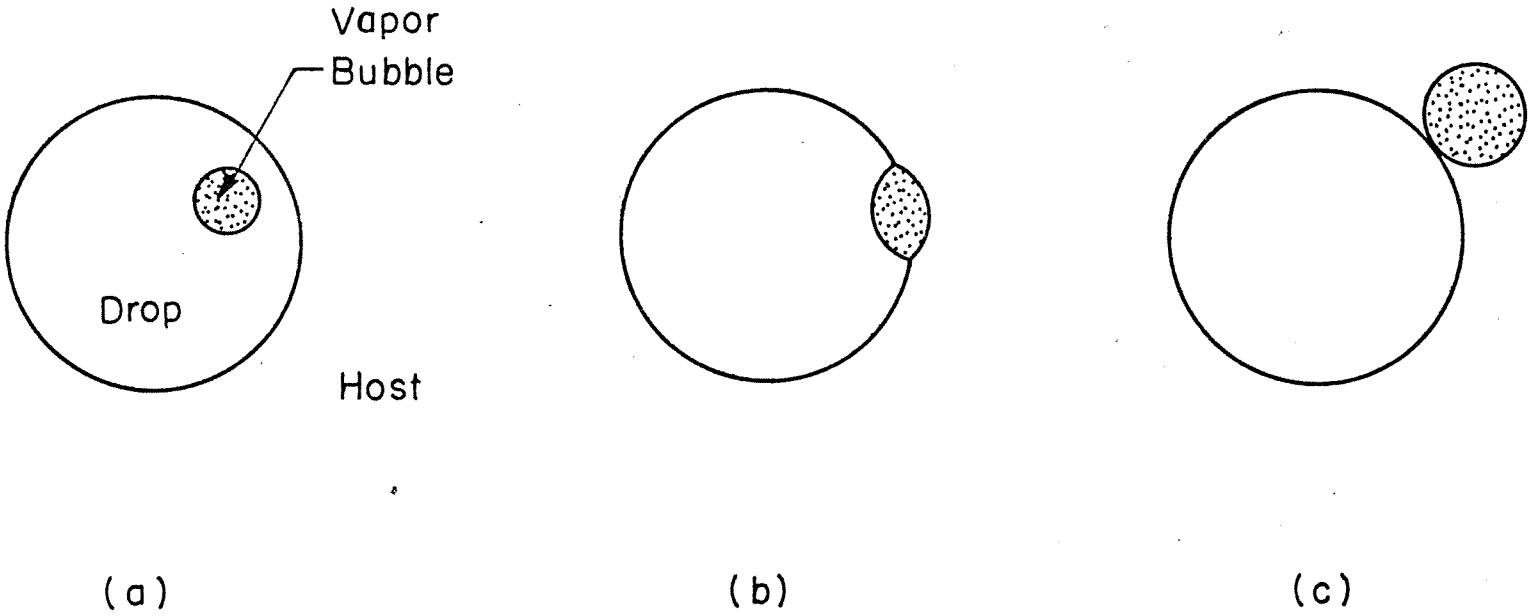

FIG. 3.12 DIFFERENT MODES OF DROPLET NUCLEATION

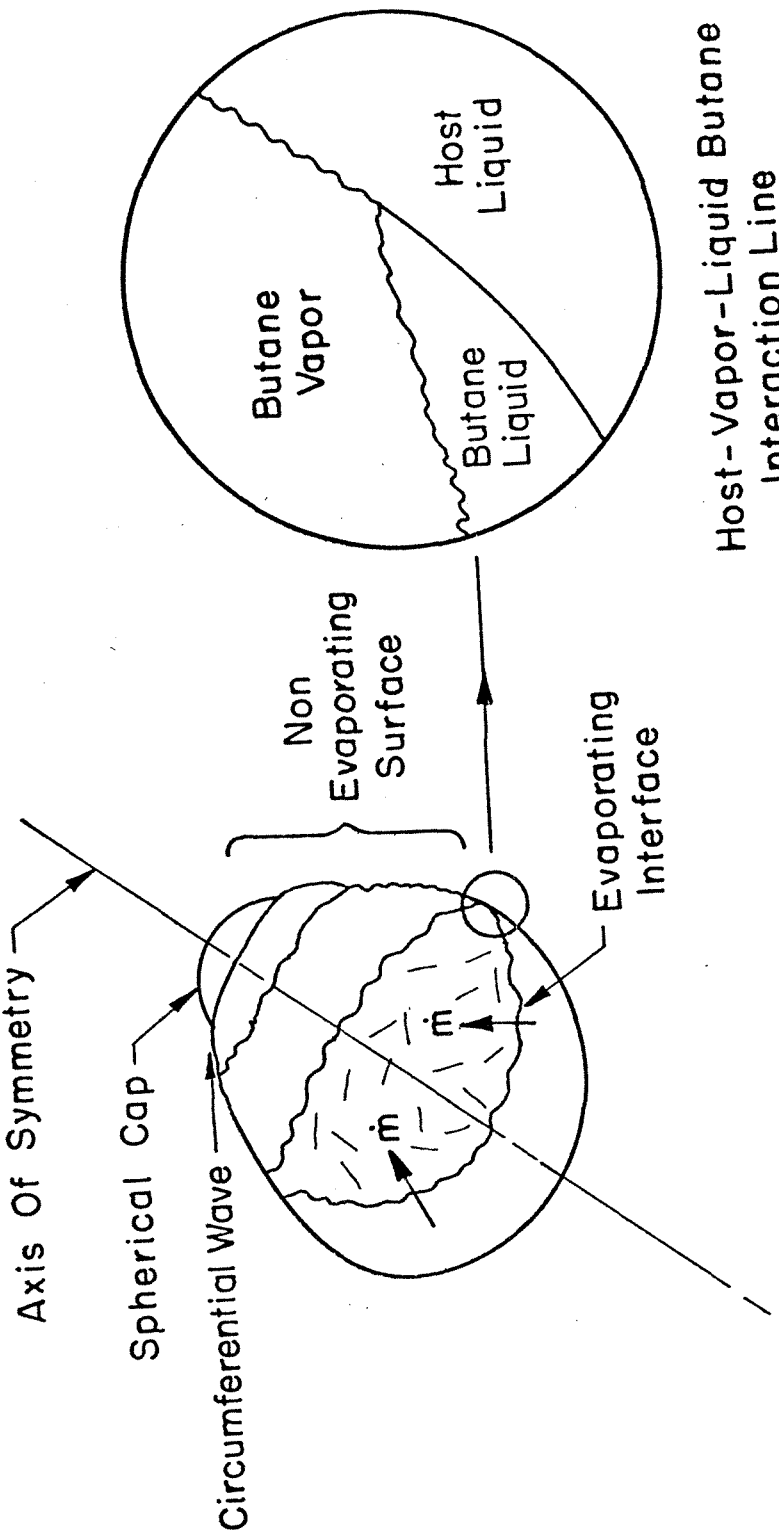

FIG. 3.13 DEVELOPING BUBBLE STRUCTURE

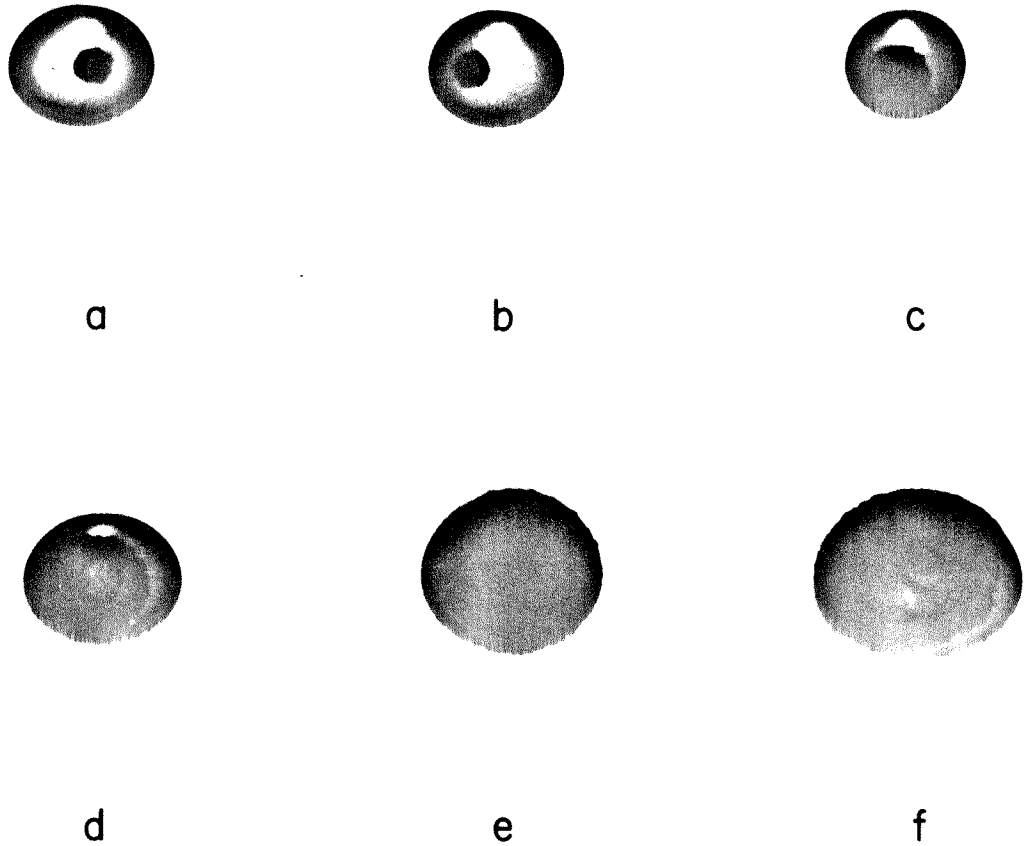

FIG. 3.14 "REAR" VIEW OF DEVELOPING BUBBLE STRUCTURE (9-55 μ sec)

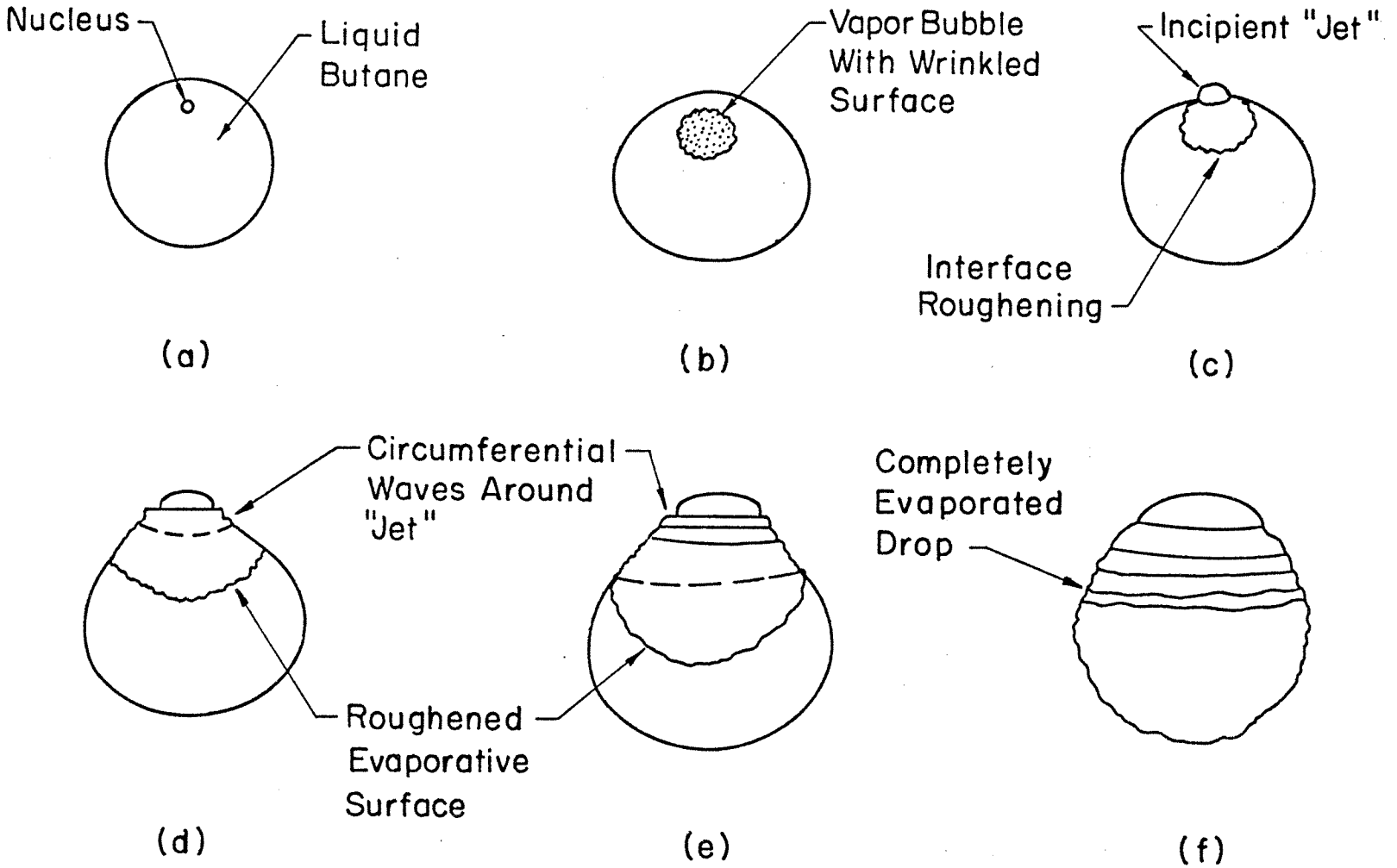

FIG. 3.15 SCHEMATIC OVERVIEW OF EVAPORATIVE STAGE

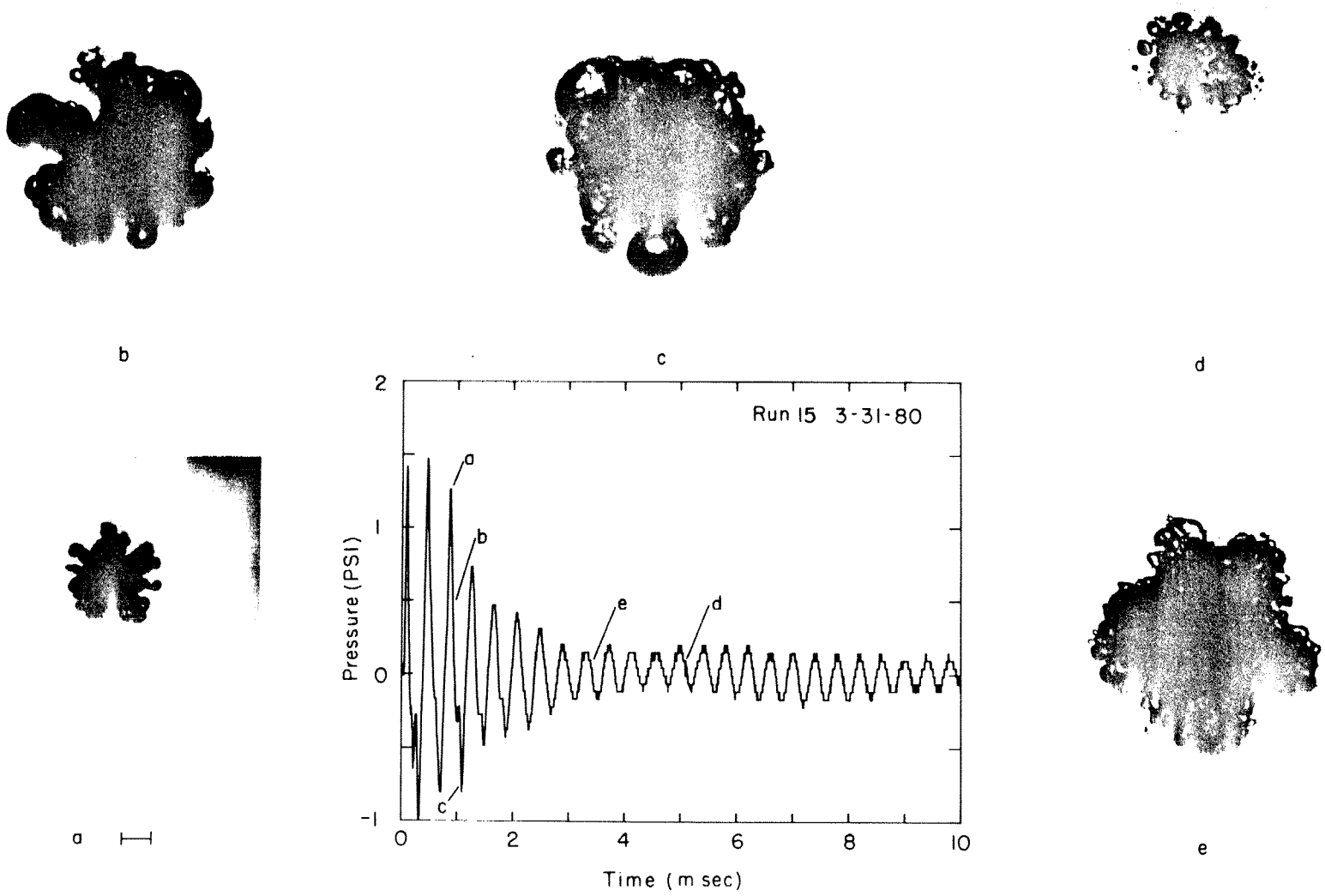

FIG. 3.16 BUBBLE OSCILLATION, INSTABILITY AND COMPLETE BREAKUP, SMALLER INITIAL DROPS

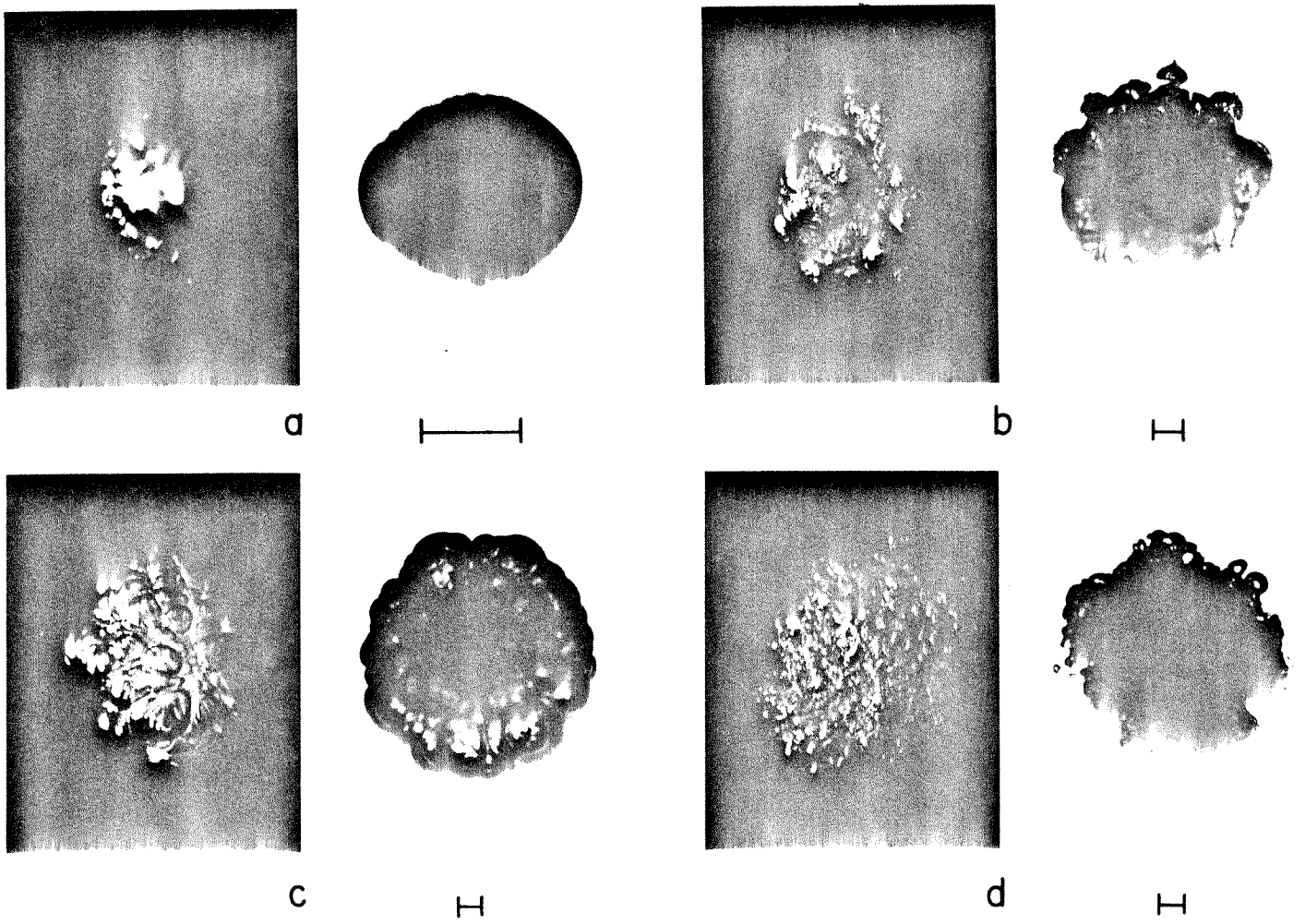

FIG. 3.17 DUAL-VIEW SPARK GAP PHOTOGRAPHS, DIRECT AND SCATTERED ILLUMINATION ((a) EVAPORATIVE STAGE; (b) - (d) OSCILLATING DEFORMED BUBBLES).

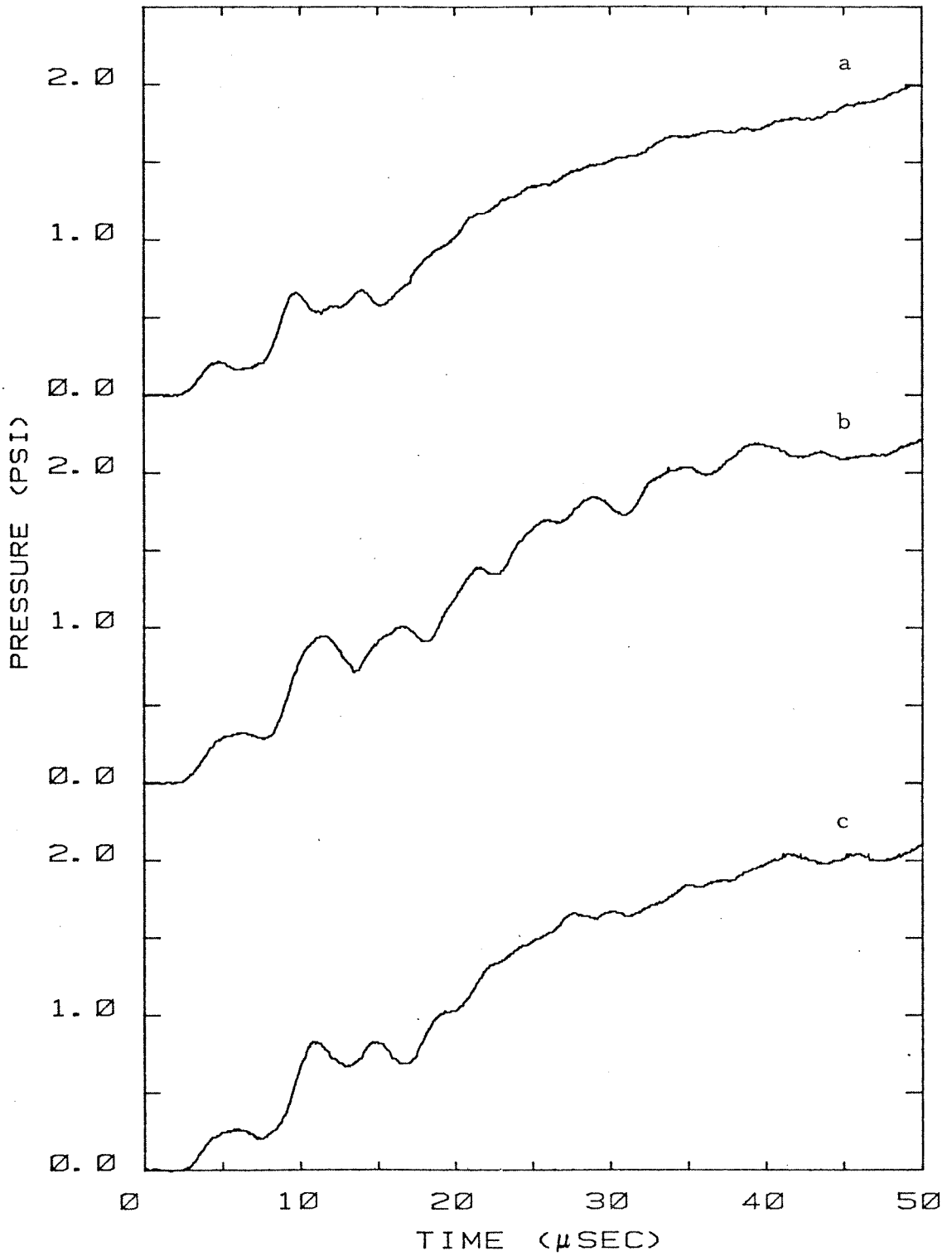

FIG. 3.18 DETAILS OF THE PRESSURE SIGNAL DURING THE FIRST 50 μsec OF EVAPORATION FOR 3 DIFFERENT EXPLOSIONS.

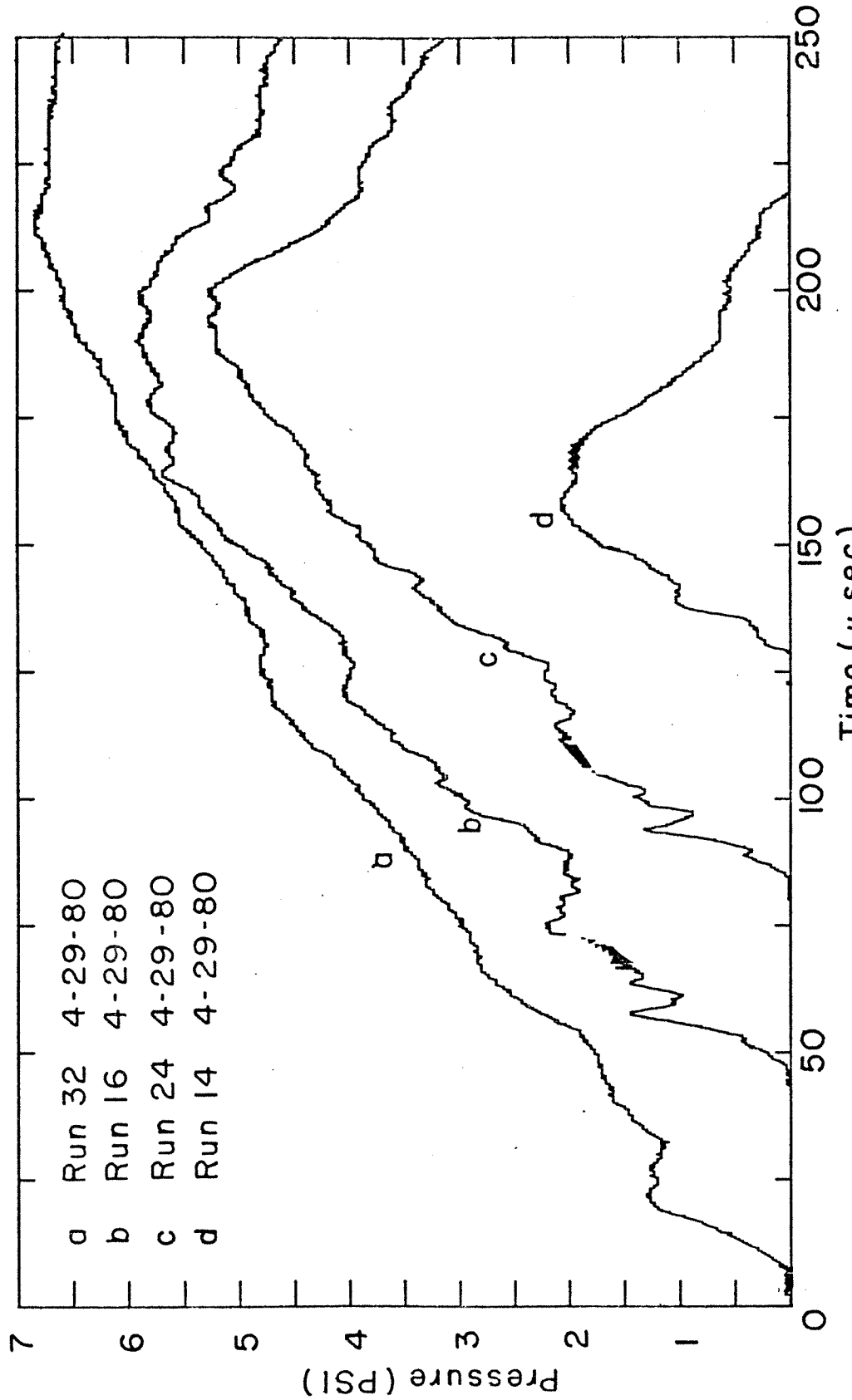

FIG. 3.19 PRESSURE SIGNAL DURING THE EVAPORATIVE STAGE OF 4 DIFFERENT EXPLOSIONS.

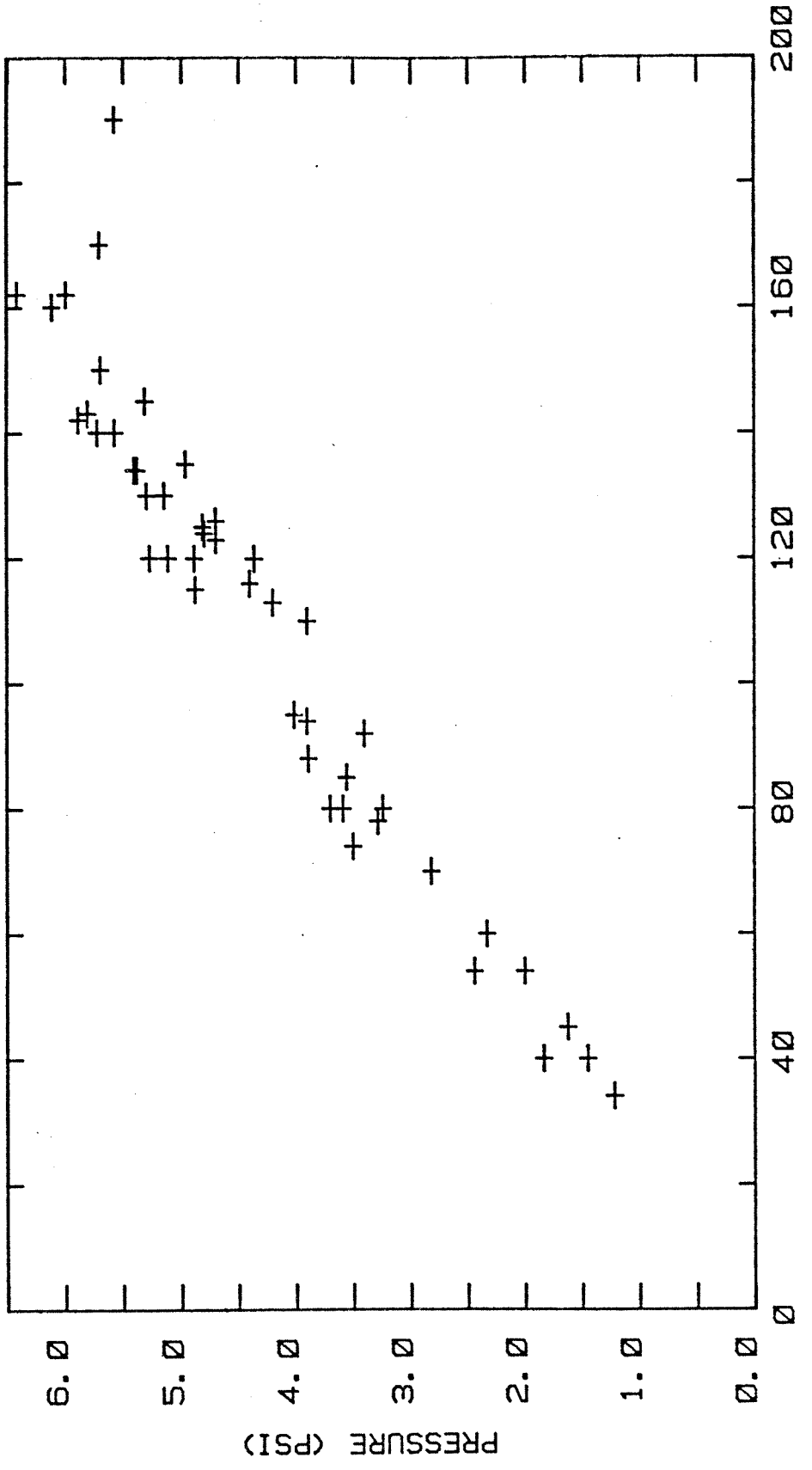

FIG. 3.20 MAXIMUM PRESSURE PRODUCED BY EVAPORATION vs. THE LENGTH OF THE EVAPORATIVE STAGE.

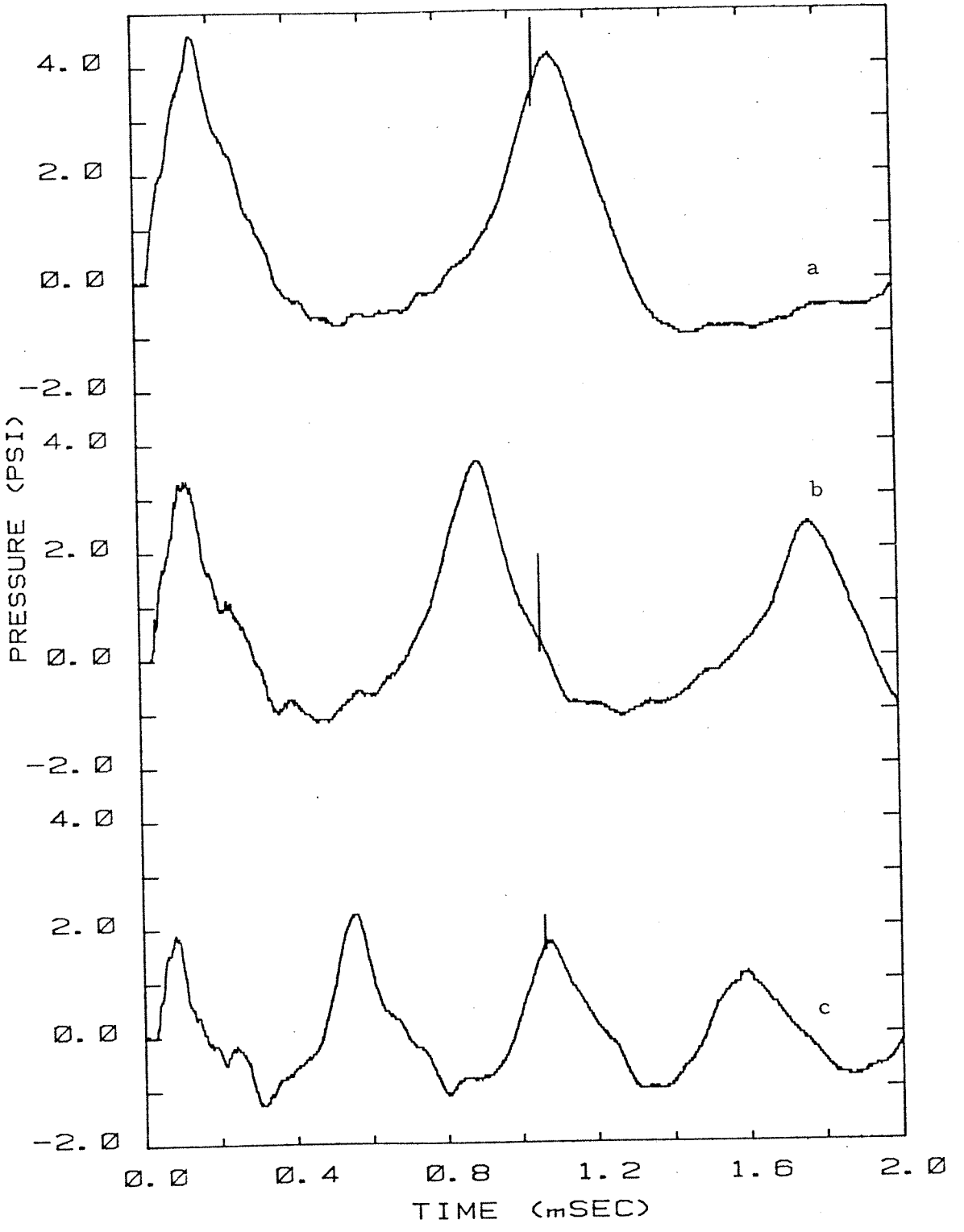

FIG. 3.21 COMPARISON OF 0-2 msec PRESSURE SIGNALS FROM 3 DIFFERENT EXPLOSIONS.

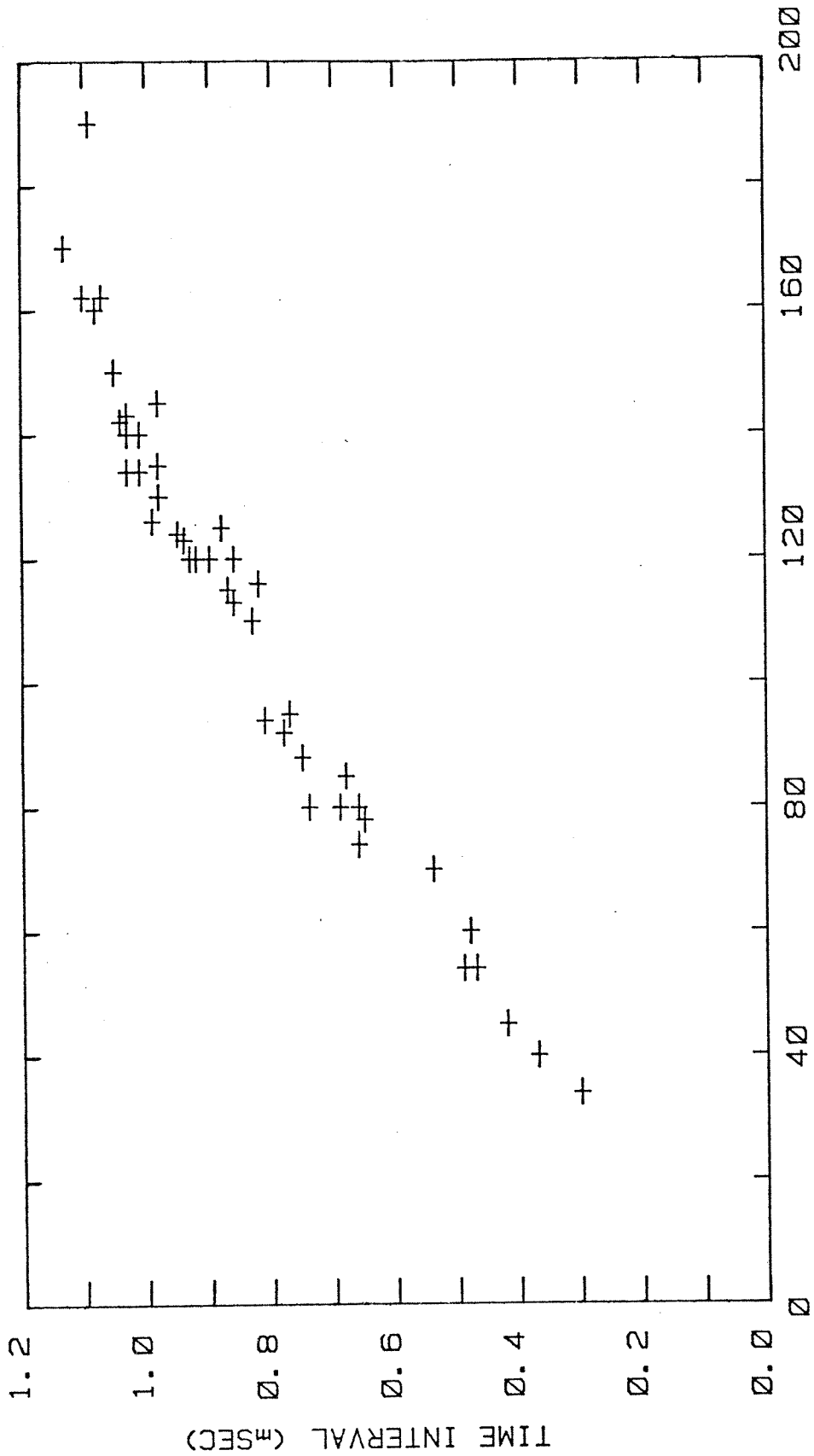

FIG. 3.22 INTERVAL BETWEEN THE END OF THE EVAPORATIVE STAGE AND THE FIRST BUBBLE PULSE vs. THE LENGTH OF THE EVAPORATIVE STAGE.

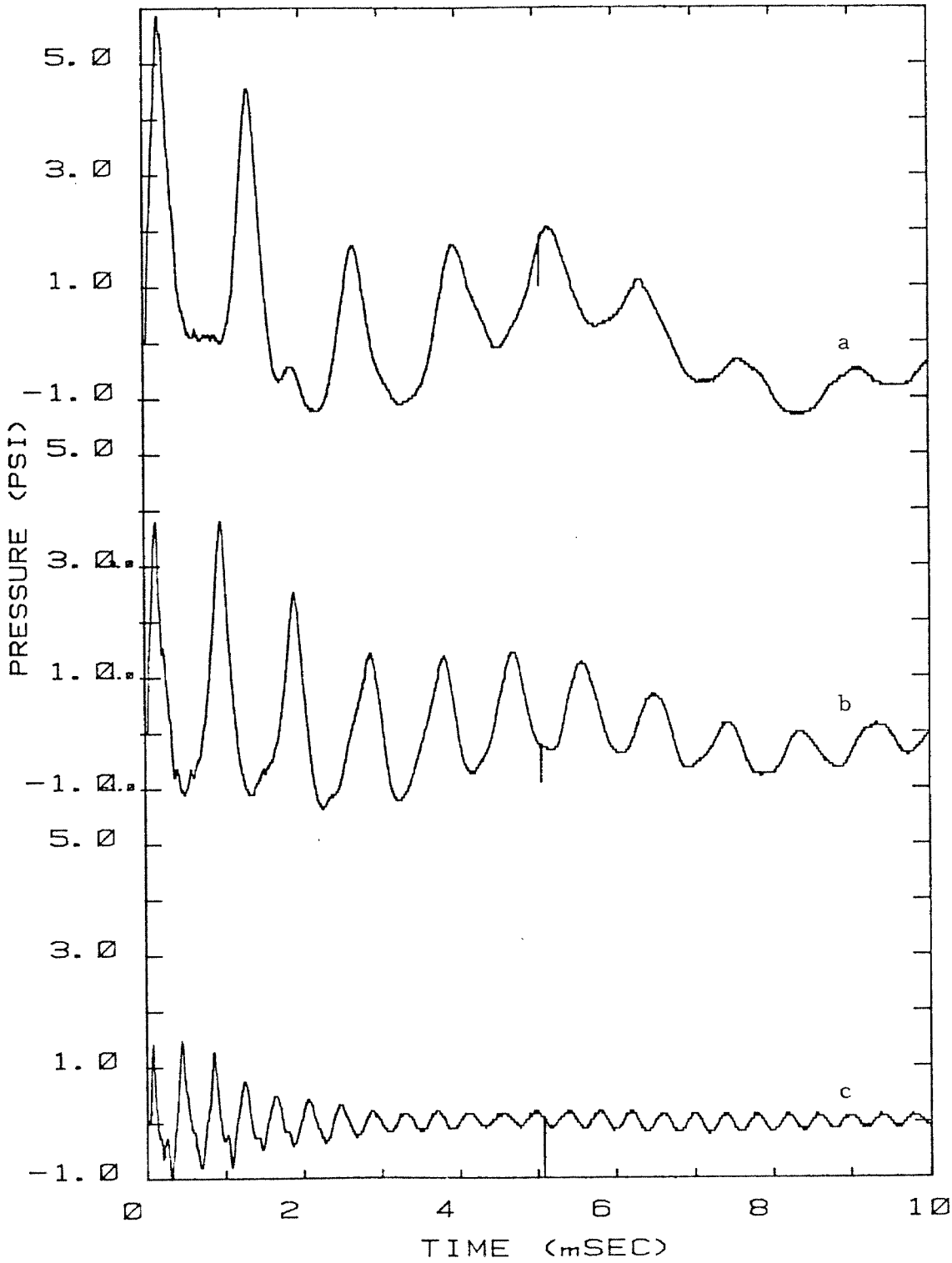

FIG. 3.23 COMPARISON OF 0-10 msec PRESSURE SIGNALS FROM 3 DIFFERENT EXPLOSIONS.

IV. BUBBLE GROWTH AND EVAPORATION RATE

4.1 Introduction

It is possible using the data obtained in these experiments to obtain quantitative information about the early stages of explosive evaporation. In particular, a first estimate can be made of the evaporative mass flux during the explosion. The pressure signal emitted by the explosion can be used to calculate an equivalent acoustic source, whose strength is the time derivative of the fluid volume displaced by the growing bubble. The net volume displaced by the bubble is determined by the balance between fluid flowing into the bubble (evaporative mass flux) and fluid pushed ahead of the growing bubble. Digital analysis of selected photographs has been used to determine the bubble volume and mean evaporating interface area as a function of time. Thus, knowing the net fluid volume displaced by the bubble (from the pressure signal) and the physical volume of the bubble (from the photographs), the total mass flux into the bubble can be determined as a function of time. Further, knowing the mean evaporating surface area, the mean evaporative mass flux can be calculated.

In this chapter, the physical basis of the calculation outlined above is derived, the methods of data reduction are described and results using data from the first 30 μsec of the explosions observed in the present study are presented. Unfortunately, due to the sparseness of the bubble volume data, a rigorous and detailed comparison to the predictions of the standard model of bubble growth cannot be made. However, a general comparison is possible; there is clear indication that the mass flux is much larger than predicted by

available theories, as might be expected in view of our observations of highly wrinkled evaporative interfaces.

4.2 Principles of the Mass Flux Calculation

The calculation of the equivalent acoustic source for the initial phase of the explosion is greatly simplified for two reasons. First, the growing bubble can be considered a compact source; that is, the wavelengths λ of the radiated sound are all much larger than the characteristic size of the bubble. For example, an oscillation with period 3 μsec would have a 4.5 mm wavelength (in glycol), which is typically 10 bubble diameters at times of order 15 μsec. Second, the pressure transducer is in the far field of the bubble; that is, the characteristic size of the bubble R is much smaller than the bubble-to-transducer distance r, $r/R \gg 1$. For example, the exploding drops (therefore bubbles) were nominally 25 mm from the transducer for these measurements; this distance is $\sim$ 50 bubble radii at 15 μsec.

Under the simplifications given above, the first approximation to the acoustic potential φ is a simple source of strength Q, located at the center of the bubble (Landau and Lifshitz 1959, Lighthill 1978)

$$\varphi(r,t) = -\frac{Q(t - r/c)}{4\pi r} \quad .$$

Source strength $Q(t)$ is defined to be volume of fluid displaced per unit time by the source. The simplest quantity to compute is the total amount of fluid displaced up to a time t

$$\int_0^t Q(t')dt' \quad . \qquad (4\text{-}1)$$

This is just the difference between the physical volume of the bubble (the displaced volume if there is no mass flux)

$$V(t) = \int_{\text{bubble}} dv \tag{4-2}$$

and the volume formerly occupied (while in the liquid state) by the vapor presently in the bubble

$$\frac{1}{\rho_L} \int_{\text{bubble}} \rho_v \, dv \quad . \tag{4-3}$$

The liquid density ρ_L (butane) has been assumed uniform throughout the drop. Recognizing that (4-3) can be simply expressed in terms of the total amount of mass $M(t)$, in the drop at time t, the overall displaced volume is

$$\int_0^t Q(t')dt' = V(t) - \frac{M(t)}{\rho_L} \quad . \tag{4-4}$$

Differentiating and rearranging, the key equation is obtained

$$\frac{dM}{dt} = \rho_L \frac{dV}{dt} - \rho_L Q \quad . \tag{4-5}$$

The final step in this calculation is to relate the measured pressure signal to the effective source strength Q. If the region surrounding the bubble was filled only with host fluid of density ρ_∞, from acoustics the perturbation pressure p' due to the source would simply be

$$p' = - \rho_\infty \varphi_t \quad . \tag{4-6}$$

In fact, during the evaporative stage, the bubble is surrounded by both liquid butane remaining from the original drop and the host

liquid. Due to the differing densities and acoustic impedances of the liquid glycol and butane, the butane-glycol interface at the drop surface may alter the radiation from the bubble, making (4-6) invalid. However, it is possible to show that the interface's effect is negligible except possibly for a short period of time just after the initiation of bubble growth. The basis of this approximation is that, under the compact source conditions assumed earlier, true acoustic waves exist only in the far field of the source and in the near field the fluid moves as if it were incompressible (Landau and Lifshitz 1959).

This fundamental property of compact sources implies that actual acoustic wave reflection from the drop surface only occurs at the very earliest times of bubble growth, when the drop surface can be considered in the far field of the bubble radiation. At later times, but still small compared to the total test time, the liquid butane and butane-glycol interface are within the near field of the bubble radiation. Since the dynamics of the incompressible motion in the near field do not appreciably deform the liquid butane-glycol interface (as shown in Figures 3.2 and 3.3), the kinematics of the motion will be the same as if the liquid butane and glycol densities were equal. In conclusion, for times greater than 3-5 μsec, the volume displacement of the bubble will be transmitted unaltered to the far field of the host, where the pressure can be calculated by (4-6), substituting the host density for ρ_∞.

The actual pressure detected by the transducer at point r is denoted $\Delta p(t)$ and can depend on p' in a complex way (as discussed in Section 2.4.1). However, before the first secondary waves

arrive ($t < 30$ μsec), the pressure Δp, on the transducer face, is just $\alpha p'$, where α is the coefficient of reflection for waves normally incident on the transducer-mount combination ($\alpha = 1.83$ for an aluminum-glycol interface). Integrating equation 4-6, the relation between measured pressure and source strength is obtained

$$Q(t) = \frac{4\pi r}{\alpha \rho_\infty} \int_0^t \Delta p(t' + r/c)dt' \quad . \qquad (4\text{-}7)$$

The far-field and compact-source assumptions imply that a detailed description of the source is not required and cannot be obtained from this analysis. Only the integral properties, V, M and Q, of the source are involved and any dependence of the emitted pressure on the source (bubble) orientation is ignored. The reasonableness of such a treatment is borne out by the experimental observations of similar pressure signals from bubbles at very different orientations to the transducer.

4.3 Data Reduction

Ideally, the pressure signal and bubble volume should be recorded simultaneously throughout each explosion in order to properly calculate the mass flux. However, in the present experiment, the bubble volume was only measured (at most) at one time in each explosion. In the spirit of ensemble averaging (and with a belief that the initial bubble growth is similar for all explosions), volume data obtained at different times in separate explosions was combined to define an effective bubble volume history. This volume, together with an ensemble-averaged pressure, was used in equations 4-5 and 4-7 to calculate the average mass flux.

The method used to calculate bubble volumes (and mean evaporating interface area) from photographs and the resulting volume history is presented in Section 4.3.1. The processing of the pressure signals and the ensemble average signal is presented in Section 4.3.2.

4.3.1 Photographs

Bubble volume and mean evaporating surface area were numerically calculated, approximating the bubble as a body of revolution, from the coordinates describing the outline of the bubble on the photograph. The calculation was simplified by analyzing only those bubbles whose axis of symmetry was in or near the plane of the photograph, i.e., the bubble must appear as in cross-section to the viewer.

A total of 22 different bubbles, representing stages of the explosion from 8.3 to 91 μsec, were analyzed. Using a graphics digitizer (HP9872), the perpendicular distance to the bubble outline, on both sides of the estimated symmetry axis Z, was recorded at evenly spaced points. The averages of the distances at a given location z on the symmetry axis was taken to be the curve $R(z)$ which described the profile of the approximating body of revolution. Typically, 30 to 50 points were recorded for a single bubble, smaller increments being used for smaller bubbles. The measured magnification of the overall reproduction process was used to convert distances on photographs to the actual bubble dimensions.

Effective bubble volume V and mean evaporating surface area A were both calculated from these data using the trapezoidal rule approximation to the standard integrals for a body of revolution

$$V = \int \pi R^2(z)dz \quad ,$$

$$A = \int 2\pi R(z)\,(1 + (\frac{dR}{dz})^2)^{1/2}\, dz \quad .$$

The derivative $\frac{dR}{dz}$, in the area integral, was approximated by the first difference. The limits of integration for the area integral were chosen so that only the area of the bubble surface estimated to be in contact with the liquid butane was calculated. No attempt was made to correct for optical distortion (lensing effect of the drop) or out-of-plane symmetry axes; these errors are estimated to be of the same order as the intrinsic error of this technique due to the natural asymmetry of the bubbles.

The results for the bubble volume V, the mean evaporative interface area A and the mean bubble radius $\overline{R} = (\frac{3V}{4\pi})^{1/3}$ are given in Table 4.1. The limits of the evaporating interface were not well defined for some of the larger drops, so values of the area were not calculated. One remarkable feature of these results is the nearly linear growth of the mean radius $\overline{R}$ with time over the entire interval (Figure 4.1), with a mean velocity of 14.3 m/sec. For the purposes of calculating the mass flux, a restricted set of the data (times < 30 μsec) was fit to a simple power law

$$\{\frac{V}{A}\} = bt^a \quad . \tag{4-8}$$

Coefficients a and b were determined by a least squares fit to the logarithm of equation 4-8. The results are:

$$V = 6.443 \times 10^{-8}\ t^{2.649}\ cm^3 \quad ; \tag{4-9}$$

$$A = 1.472 \times 10^{-4}\ t^{1.362}\ cm^2 \quad , \tag{4-10}$$

the units of t are μsec. Equations 4-9 and 4-10 are plotted, together with the individual data points, in Figures 4.2 and 4.3, respectively.

Unfortunately, it is not V, but $\frac{dV}{dt}$, which is needed in order to calculate the mass flux. In those calculations, the crude estimate obtained by analytically differentiating equation 4-9 was used. This procedure produces a definite (but unknown) bias in the result, the actual $\frac{dV}{dt}$ is certainly less smooth than this estimate.

4.3.2 Pressure Signals

Pressures at a distance of ~ 2.5 cm from the drops were measured by a PCB transducer in configuration C, Figure 2.3. The transducer was mounted in an aluminum plug 2.3" in diameter; diffracted waves from the plug's edges limited the test time to the initial 30 μsec of the explosion. During this time, it was assumed the pressure on the transducer face was the pressure produced by normal reflection of the incident wave.

The transducer output was digitized and stored in the Nicolet oscilloscope at a sampling rate of 20 MHz. Overall frequency response was limited by the transducer (which has a natural resonance at 500 KHz) to a bandwidth of 1 MHz. The initial zero level of the signal was subtracted, an overall scaling factor (a product of detector sensitivity and amplifier gain) computed and the raw data converted to psi on the transducer face. Each signal was inspected to determine the exact location (within ± 0.1 μsec) of the beginning of the first pressure increase due to the explosion. This location was used as the absolute origin of time ("time zero") in the computation and averaging of the signals.

A total of 7 pressure signals were processed by this scheme and averaged together (all signals were aligned so that every "time zero" coincided) to yield an ensemble average pressure signal, shown in Figure 4.4. This is the average signal which is used to compute the average source strength from equation 4-7. Comparing the average signal with the individual signals in Figure 3.19, some common features stand out. In particular, the characteristic steps at 5 and 10 μsec appear distinctly in the average signal and can be seen to various extents in all of the individual signals. However, the oscillatory structure which is superposed on the general pressure rise after 10 μsec in many individual signals is not universal and is washed out in the averaging process.

4.4 Results

The stage of the explosion considered in these calculations is displayed in Figure 4.5. In this figure, a series of photographs (some of which were used in the volume calculations) and a representative pressure trace illustrate bubble growth from 16 to 40 μsec. Actually, the most intriguing features of the pressure trace are the steps or bumps occurring at the very earliest times, during the first 15 μsecs. From the discussion in Section 4.2, it is clear that these rapid changes in radiated pressure are due principally to rapid changes in the volume growth rate or evaporative mass flux. It is tempting to relate this unsteadiness in the pressure with evaporative instabilities which could cause large and rapid changes in the mass flux. The possibility of such an instability has already been suggested in connection with the interface wrinkling (Section 3.3.3). However, since no photographs have been obtained before 8 μsec,

very little volume data is available to support any conclusions about the mass flux at these early times.

Lacking a better alternative, the analytical fits to the data, equations 4-9 and 4-10, were used to calculate the mass flux from $t = 0$ onward. This is, in effect, a backward extrapolation of the smoothed volume data. Therefore, any rapid changes of pressure appear to arise only from rapid changes of mass flux, whereas, in reality, both mass flux and volume contribute to the pressure signal.

Results have been calculated up to 50 μsec, despite the injunctions against using the pressure data past 30 μsec. This was done to show that effects of secondary waves are gradual and no discontinuity occurs when they first appear. The volume derivative calculated from equation 4-9 is shown in Figure 4.6. This is to be compared with the average source strength, shown in Figure 4.7. The difference between these two terms is the volume of liquid butane that has been evaporated. Using these data in equations 4-5 and 4-6, the total mass M in the bubble and its derivative $\frac{dM}{dt}$ have been computed and are plotted in Figure 4.8. Notice that the bumps in the pressure produce only a slight waviness in $\frac{dM}{dt}$ and have no visible effect on M.

Mean evaporative mass flux $\dot{m}$ was calculated by

$$\dot{m} = \frac{1}{A} \frac{dM}{dt} \quad , \tag{4-11}$$

where A is given by equation 4-10. As shown in Figure 4.9, the mass flux rises very rapidly (most of the increase occurs in the first microsecond) and after several wiggles levels off at about 400 gm/cm^2 sec. The nature of the wiggles and their possible relation to bubble growth is considered in the next section.

An evaporative mass flux of 400 gm/cm^2 sec is large under any circumstances! Mass fluxes typical of low superheat bubble growth experiments (e.g. Table 3.2) are of the order 10^{-1} to 10^{-3} gm/cm^2 sec. Other common examples of evaporation (tea kettles, power plant steam generators, etc.) have similarly low mass fluxes. Only in extreme situations, such as vacuum distillation (Hickman 1972) or laser ablation of metals (Ready 1965), does the mass flux reach $\sim 10^2$ gm/cm^2 sec.

There is a simple argument which confirms that this large value of the mass flux nevertheless is not unreasonable. Suppose the liquid to be evaporated at constant rate through the surface of a sphere growing at a constant radial velocity $\dot{R}$. The net rate of consumption of liquid mass would be

$$\frac{dM}{dt} = \dot{m}A = \dot{m}4\pi\dot{R}^2 t^2 \quad . \tag{4-12}$$

Integrating, the time t to evaporate a mass of liquid originally contained in a sphere of radius R_o is found to be

$$t = \frac{R_o}{\left(\frac{\dot{m}}{\rho_L}\dot{R}^2\right)^{1/3}} \quad . \tag{4-13}$$

Substituting the values $\dot{m}$ = 400 gm/cm^2 sec, ρ_L = 0.43 gm/cm^3 and $\dot{R} = 1.4 \times 10^3$ cm/sec, a 0.5 mm radius drop is found to evaporate completely in the quite reasonable time of 50 μsec. In reality, only a portion of bubble surface is evaporating and the estimate given here is a lower bound to the actual time required for evaporation.

4.5 Comparison with the Classical Model

In this section, the predictions of the "classical model" of vapor bubble growth (introduced in Section 1.2.3) are compared with the experimentally measured and inferred results. Strictly speaking, this comparison is possible only for that small interval of time ($\sim$ 10 μsec) where it has been conjectured (Section 3.3.1) that the bubble is completely surrounded by the drop liquid. As the bubble grows and interacts with the host fluid, a smaller fraction of the bubble surface is actually evaporating in the experimental case than in the idealized bubbles of the theory. Therefore, the predictions of the theory should overestimate bubble growth for $t > 10$ μsec; in fact, it is found that the growth is vastly underestimated at these later times. The extent to which this occurs is demonstrated by comparing bubble volumes, then mass fluxes and finally pressure signals over the first 30 μsec of growth. It should be kept in mind that experimental results for the effective bubble volume, in the first 10 μsec, are an extrapolation of the actual data, which were all obtained at later times.

From this point on, the "classical" theory of bubble growth will mean the latest and most complete version of that theory as presented by Prosperetti and Plesset (1978). This theory describes the growth of a smooth, spherical vapor bubble from a critical nucleus in a uniformly superheated liquid. Bubble growth is conveniently divided into three stages: first, a surface-tension-controlled stage in which the bubble grows from a critical nucleus, radius R_o; second, an inertia-controlled stage in which the bubble surface grows with a characteristic velocity $\dot{R}_o$ (determined by the vapor pressure

and density of the superheated fluid); third, an asymptotic stage in which bubble growth is dominated by heat transfer and is characterized by a $R \sim t^{1/2}$ dependence. Once the bubble has grown out of the surface-tension-dominated stage, the growth is approximately described (under the assumptions of the theory) by a universal equation in scaled variables. The approximations involved in deriving this universal equation are: a) the surface tension is negligible; b) the vapor pressure $p_v(T)$ is a linear function of temperature T; c) both latent heat and vapor density are constants, independent of the evaporating surface temperature. The scale length and time are the radius of the bubble R^* and the time t^* at which the cross-over from inertia to asymptotic stages occurs.

Two additional parameters μ and τ, characterizing bubble growth, are defined;

$$\mu = \left(\frac{R_c}{R^*}\right)^{1/2} , \quad \tau = \frac{R_o}{R^*} t^* \approx \frac{R_o}{\dot{R}_o} . \tag{4-14}$$

Parameter μ determines the relative importance of the inertial stage of growth. A decreasing function of superheat, $\mu \approx 1$ for low superheats (predominantly heat-transfer-controlled growth) and decreases to $\sim 10^{-3}$ at superheat-limit conditions (predominantly inertia-controlled growth). Parameter τ is the characteristic time required for the bubble to escape the surface-tension-controlled stage and is also a decreasing function of superheat. Parameter values and scale lengths are given in Table 4.2; these have all been calculated from the equilibrium properties of saturated n-butane by the prescription given in Prosperetti and Plesset. Since the properties of the saturated liquid and vapor play such an important role in this theory,

selected properties of saturated n-butane are given in Table 4.3. These properties were calculated from the following thermodynamic correlations and empirical formulas: vapor pressure, Riedel equation (Reid et al 1977); latent heat, Watson relation (Reid et al 1977); surface tension, corresponding-states correlation (Reid et al 1977); vapor density, Thompson correlation (Thompson and Sullivan 1979); liquid density, Rackett equation (Rackett 1970).

In this theory, the vapor in the bubble is assumed to be uniform and in equilibrium with the liquid surface; thus, there are only two independent variables, bubble radius R and surface temperature T_s. The approximations in the theory determine all other quantities as a function of R, T_s and their derivatives. For convenience, approximate analytical expressions for R and T_s were used in this comparison, instead of exactly computing the Prosperetti-Plesset model for this particular case. These analytic expressions are equations (8) and (13) of Mikic et al (1970) with the modified evaluation of scaling constants suggested in Prosperetti and Plesset, who show that these expressions are in reasonable agreement with the solutions to the universal bubble growth equation. The thermodynamic properties of saturated butane used in this comparison were obtained from the analytic formulas mentioned above in connection with Table 4.3.

Figures 4.10 and 4.11 compare the predicted bubble volume and volume growth with the fit to the experimental data over the first 30 μsec. Predicted V and $\frac{dV}{dt}$ are initially larger and then drop far beneath the experimental values. As pointed out at the beginning of this section, the large discrepancy at later times is due

to the inadequacy of the classical model rather than any invalidity of the comparison. An alternative comparison is shown in Figure 4.1 where both the bubble radius computed by the classical model and the limiting inertial growth rate ($\dot{R}_o$ = 40 m/sec) are shown together with the experimental effective radius data. Note that the predicted growth very rapidly deviates from the inertial limit and only the asymptotic diffusion-limited stage is apparent on the time scale of Figure 4.1.

The predicted evaporative mass flux $\dot{m}$ is approximated in the theory as

$$\rho_V(T_s)\,\frac{dR}{dt} \quad , \tag{4-15}$$

(a term involving $\frac{d\rho_V}{dt}$ has been neglected here; including this term can only decrease the predicted mass flux) where $\rho_V(T_s)$ is the saturated vapor density at temperature T_s. Figure 4.12 compares this prediction with the experimental results for this first 10 μsec of bubble growth. It is in the mass flux comparison that the differences between theory and experiment are most clearly demonstrated. Predicted and inferred mass fluxes at 10 μsec differ by 10^2. This situation only worsens with increasing time, since the theory predicts that $\dot{R}$ and T_s decrease monotonically; hence, by equation 4-15, so must $\dot{m}$. Further, this predicted behavior of $\dot{m}$ rules out any oscillatory behavior with time. This is not necessarily the case with the emitted pressure wave, discussed next.

Within the framework of the theory, the pressure pulse produced by the bubble can be calculated from incompressible bubble dynamics. While this appears inconsistent with the acoustic treatment of the experimental pressure, it can be shown that, in the far

field of a compact source, the pressure calculated from acoustics agrees with that calculated from potential flow (except for the retarded time in the acoustic result, which has already been compensated for in the data processing). The far field pressure at a distance r from the bubble center can be written

$$p' = \frac{R}{r} \left(p_V(T_s) - p_\infty + \frac{1}{2} \rho_\infty \dot{R}^2\right) \quad . \tag{4-16}$$

The combination of an increasing bubble radius and a decreasing temperature and velocity suggests that the pressure can have a maximum. The pressure calculated by equation 4-16 (divided by α to simulate reflection at the transducer) is compared to the ensemble average pressure in Figure 4.13. A broad maximum occurs at 3 μsec; in view of the approximations used in this comparison and in view of the foregoing comparisons of experiment with theory the coincidence of the peak value with the measured signal is strictly fortuitous. Under the assumptions of the theory only one maximum can occur in the predicted pressure so the subsequent bumps and much greater rate of increase measured experimentally are unexplained by the theory.

REFERENCES

Hickman, K. 1972 "Torpid Phenomena and Pump Oils", J. Vac. Sci. Tech. 9, 960.

Landau, L.D. and Lifshitz, E.M. 1959 Fluid Mechanics, Pergamon, New York.

Lighthill, J. 1978 Waves in Fluids, Cambridge University Press, Cambridge.

Mikic, B.B., Rohsenow, W.M. and Griffith, P. 1970 "On Bubble Growth Rates", Int. J. Heat Mass Transfer 13, 657.

Prosperetti, A. and Plesset, M.S. 1978 "Vapor-Bubble Growth in a Superheated Liquid", J. Fluid Mech. 85, 349.

Rackett, H.G. 1970 "Equation of State for Saturated Liquids", J. of Chem. Eng. Data 15, 514.

Ready, J.F. 1965 "Effects Due to Absorption of Laser Radiation", J. App. Phys. 36, 462.

Reid, R.C., Prausnitz, J.M. and Sherwood, T.K. 1977 The Properties of Liquids and Gases, McGraw-Hill Book Co., New York.

Thompson, P.A. and Sullivan, D.A. 1979 "A Simple Formula for Saturated-Vapor Volume", Ind. Eng. Chem. Fund. 18, 1.

TABLE 4.1

BUBBLE VOLUME, EQUIVALENT RADIUS AND EVAPORATING SURFACE AREA

Experiment (Date)	(Run #)	Time (μs)	V (mm^3)	$\overline{R}$ (mm)	A (mm^2)
3/22	2	8.3	1.88×10^{-2}	0.164	0.338
3/14	3	9.0	2.41	0.178	0.251
3/14	4	11.0	2.89	0.190	0.401
3/14	13	11.8	4.15	0.215	0.487
4/29	31	12.9	5.71	0.238	0.393
4/29	27	16.4	9.54×10^{-2}	0.283	0.530
4/28	12	20.2	0.257	0.394	0.864
4/28	20	24.0	0.292	0.411	0.900
4/28	13	25.2	0.335	0.431	1.43
4/29	5	27.3	0.455	0.477	1.65
4/28	17	28.5	0.423	0.466	1.34
4/29	10	30.4	0.589	0.520	1.82
4/29	21	32.5	0.571	0.515	1.66
4/29	17	34.1	0.754	0.565	1.63
4/29	20	39.6	1.02	0.625	
3/23	4	51	1.82	0.756	
3/23	2	52	2.09	0.793	
3/23	1	55	2.18	0.804	
3/7	12	65	2.97	0.892	
3/30	18	69.3	5.42	1.09	
3/23	19	88	10.1	1.34	
3/23	11	91	11.3	1.39	

TABLE 4.2

SCALE LENGTHS AND PARAMETERS IN THE PLESSET-PROSPERETTI THEORY EVALUATED FOR BUTANE AT THE SUPERHEAT LIMIT

Parameter	Description	Value
R_o	Radius of critical nucleous	4×10^{-7} cm
$\dot{R}_o$	Characteristic radial velocity of interface in inertia stage	4×10^{3} cm/sec
R^*	Scaling length, radius of bubble at crossover from inertia to asymptotic stage	1×10^{-1} cm
t^*	Scaling time, time required to reach crossover from inertial to asymptotic stage	2×10^{-5} sec
τ	The time required for the bubble to crossover from surface tension to inertia stage ($= a^{-1}$ defined by Prosperetti and Plesset)	1×10^{-10} sec
μ	$(\frac{R_o}{R^*})^{1/2}$	2×10^{-3}

TABLE 4.3

PROPERTIES OF SATURATED N-BUTANE

Temperature °C	Vapor Pressure (Bars)	Vapor Density gm/cc	Liquid Density gm/cc	Latent Heat J/gm	Surface Tension dynes/cm	Specific Volume Difference cc/gm
0.00	1.03	2.73×10^{-3}	5.98×10^{-1}	3.85×10^{2}	1.48×10^{1}	3.65×10^{3}
5.00	1.24	3.26	5.93	3.80	1.42	3.04
1.00×10^{1}	1.49	3.88	5.87	3.75	1.36	2.56
1.50	1.77	4.58	5.81	3.70	1.30	2.17
2.00	2.09	5.37	5.76	3.65	1.25	1.84
2.50	2.45	6.26	5.70	3.59	1.19	1.58
3.00	2.86	7.27	5.64	3.54	1.13	1.36
3.50	3.32	8.40	5.58	3.48	1.07	1.17
4.00	3.82	9.65	5.52	3.42	1.02	1.02
4.50	4.39	1.10×10^{-2}	5.45	3.37	9.64×10^{0}	8.86×10^{1}
5.00	5.01	1.26	5.39	3.30	9.09	7.75
5.50	5.70	1.43	5.32	3.24	8.55	6.79
6.00	6.46	1.62	5.26	3.18	8.01	5.97
6.50	7.28	1.83	5.19	3.11	7.48	5.26
7.00	8.18	2.06	5.12	3.04	6.96	4.65
7.50	9.16	2.32	5.04	2.97	6.44	4.11
8.00	1.02×10^{1}	2.60	4.97	2.89	5.94	3.64
8.50	1.14	2.91	4.89	2.82	5.43	3.23
9.00	1.26	3.25	4.81	2.73	4.94	2.86
9.50	1.39	3.63	4.72	2.64	4.46	2.53
1.00×10^{2}	1.54	4.06	4.63	2.56	3.98	2.25
1.05	1.69	4.53	4.54	2.46	3.52	1.99

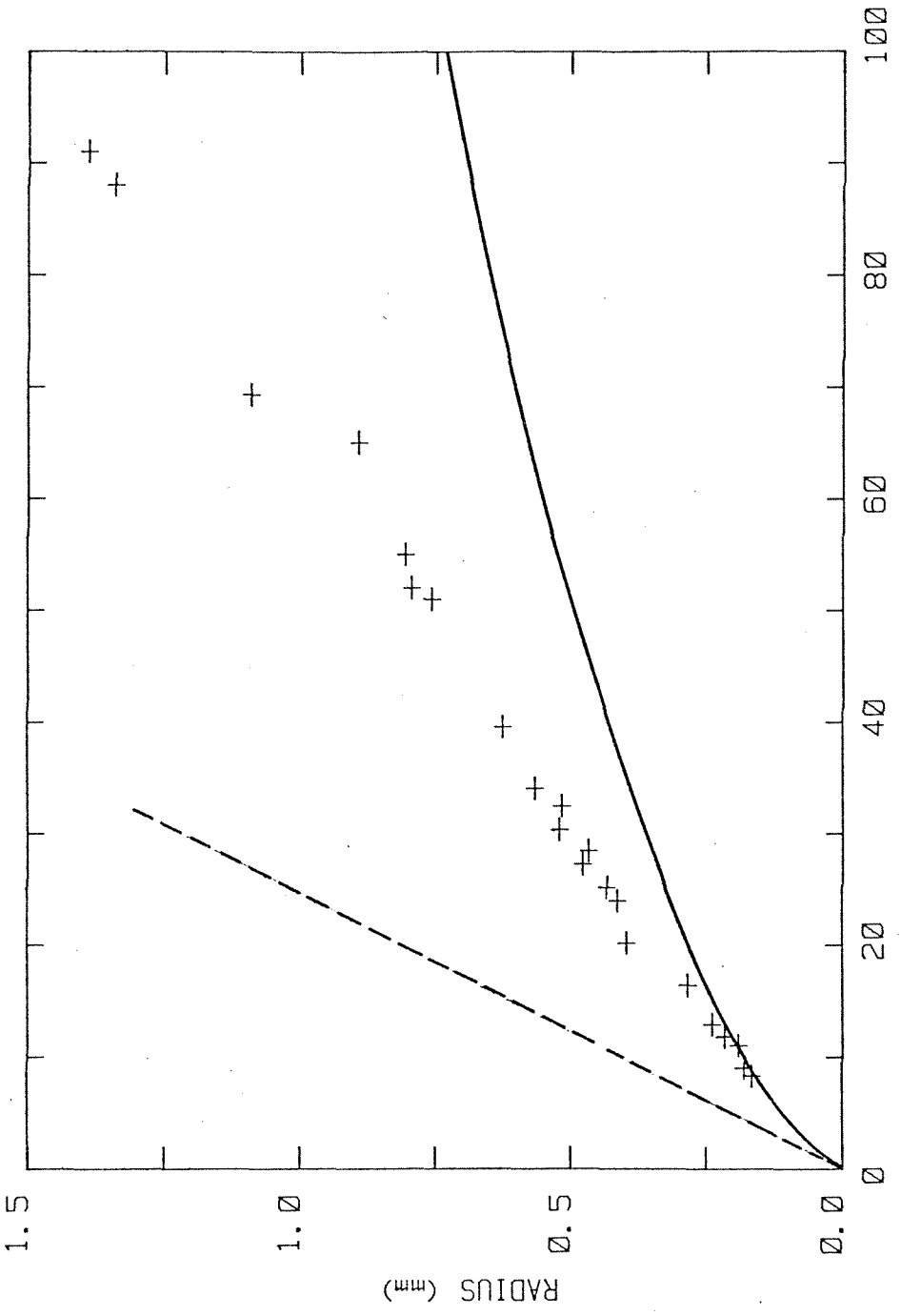

FIG. 4.1 EFFECTIVE BUBBLE RADIUS AS A FUNCTION OF TIME (+, EXPERIMENT; ——, CLASSICAL THEORY; ----, CLASSICAL INERTIAL GROWTH RATE, 40 M/S).

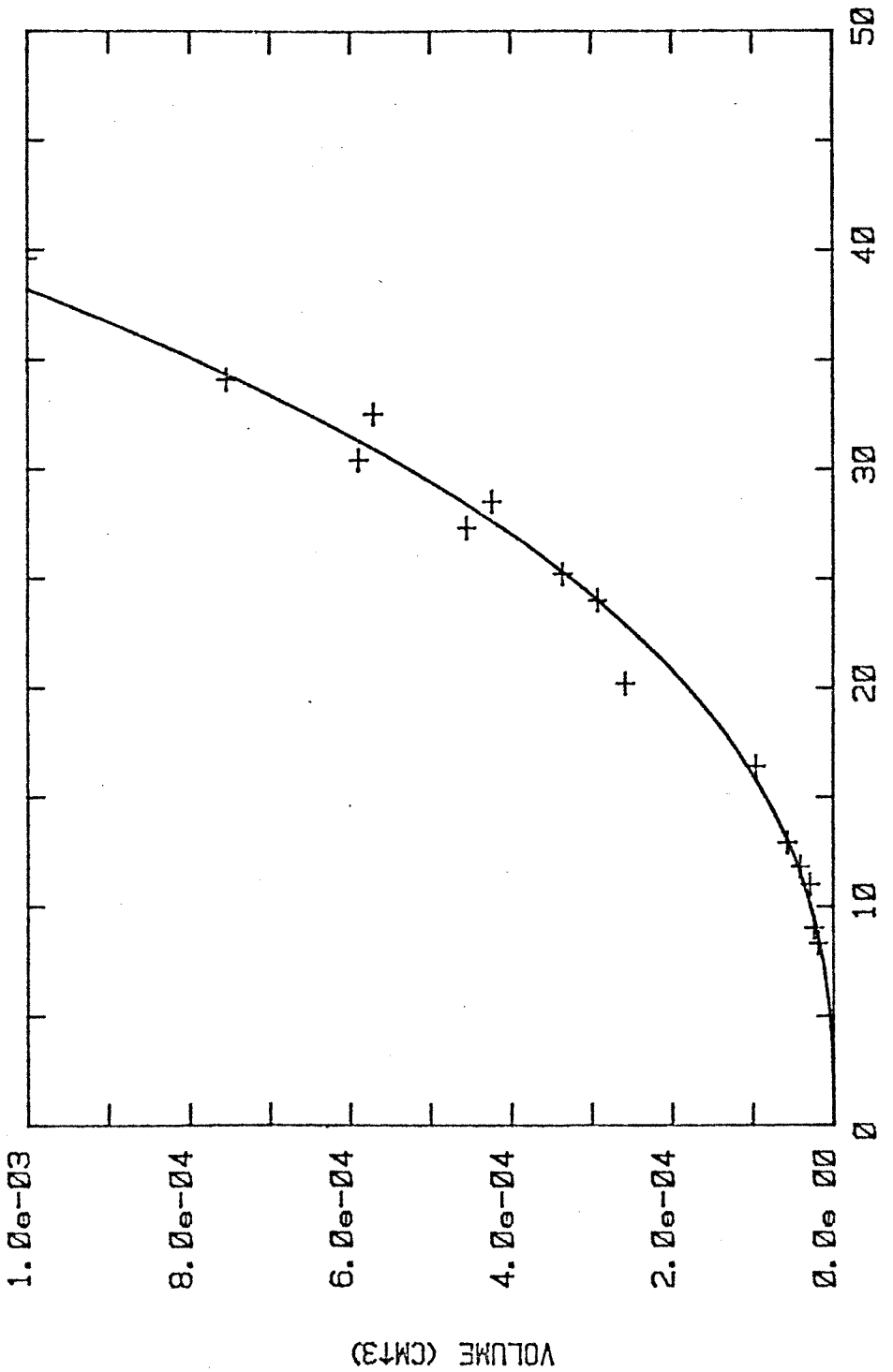

FIG. 4.2 EFFECTIVE BUBBLE VOLUME AS A FUNCTION OF TIME.

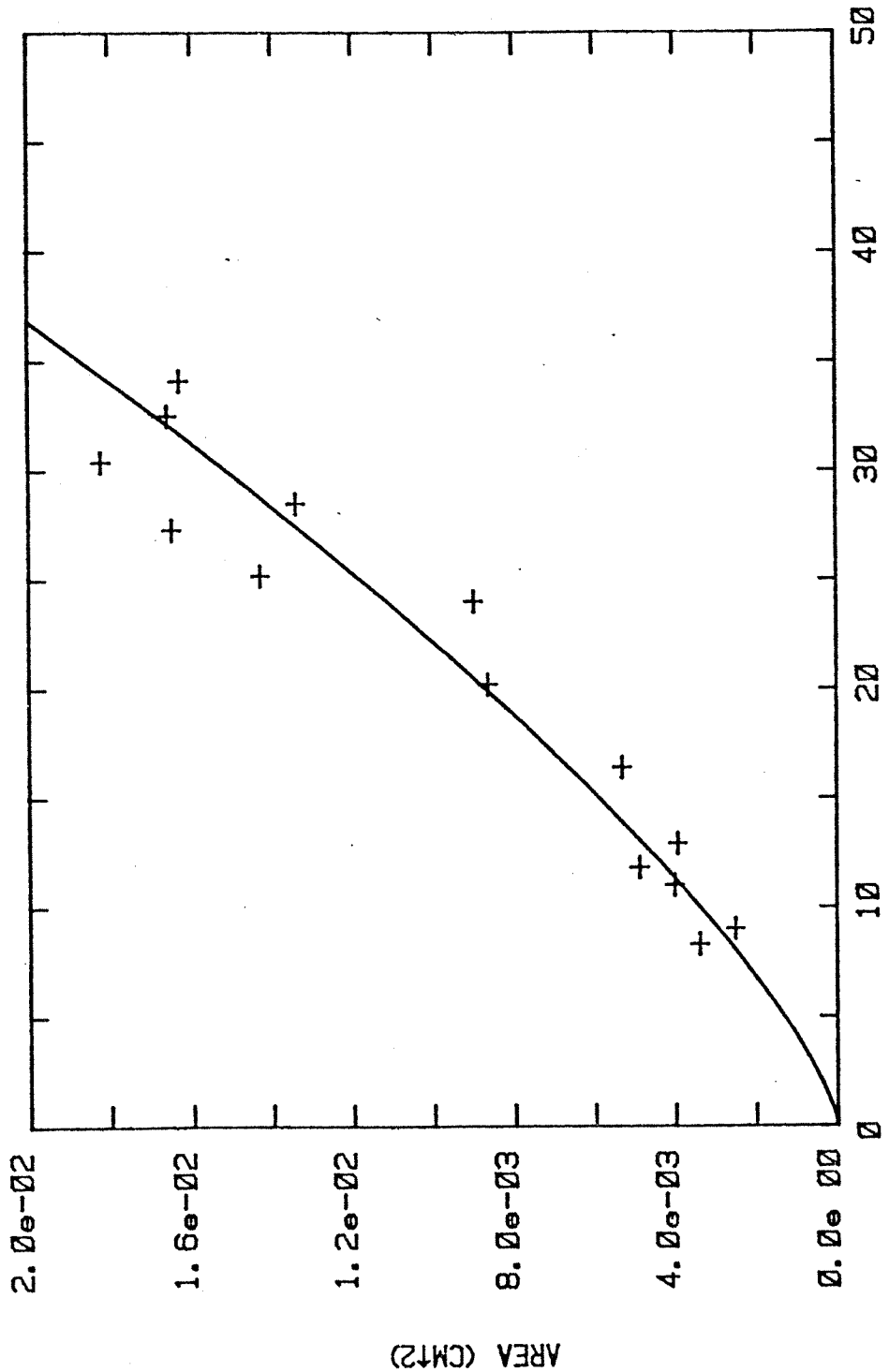

FIG. 4.3. AVERAGE EVAPORATING SURFACE AREA AS A FUNCTION OF TIME.

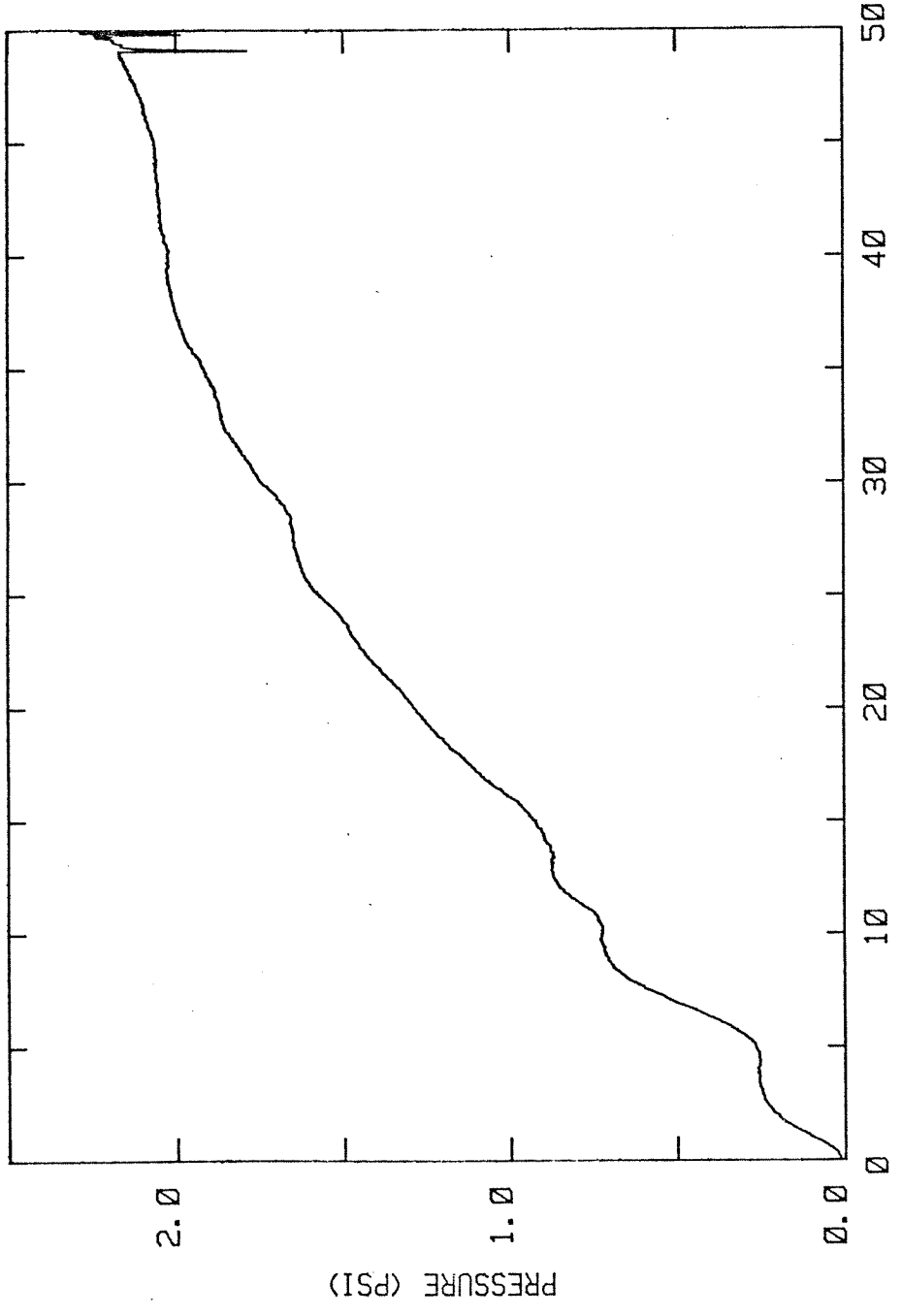

FIG. 4.4 ENSEMBLE-AVERAGE PRESSURE SIGNAL.

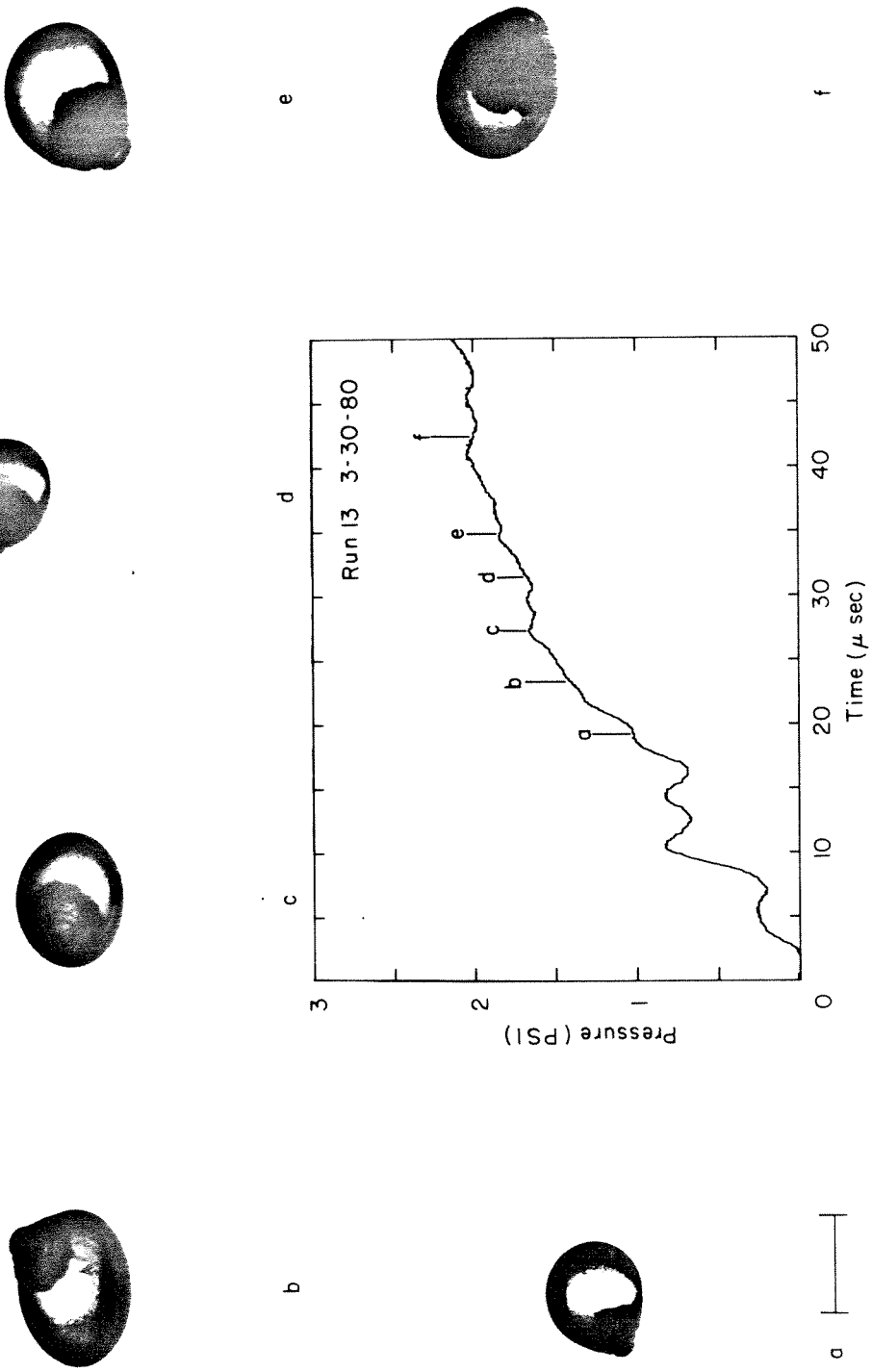

FIG. 4.5 BUBBLE GROWTH IN EARLY EVAPORATIVE STAGE.

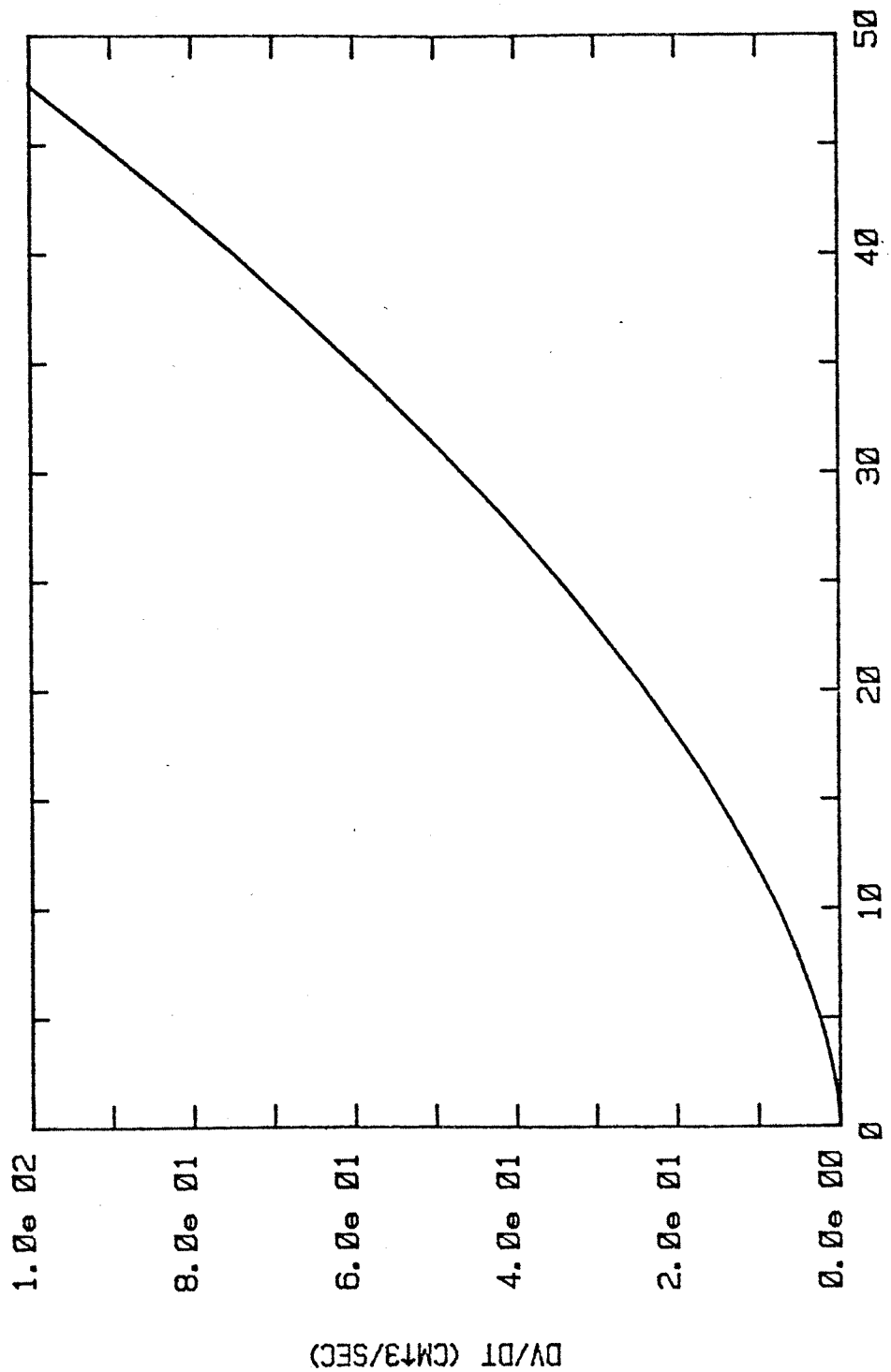

FIG. 4.6. ANALYTICAL DERIVATIVE OF VOLUME FIT.

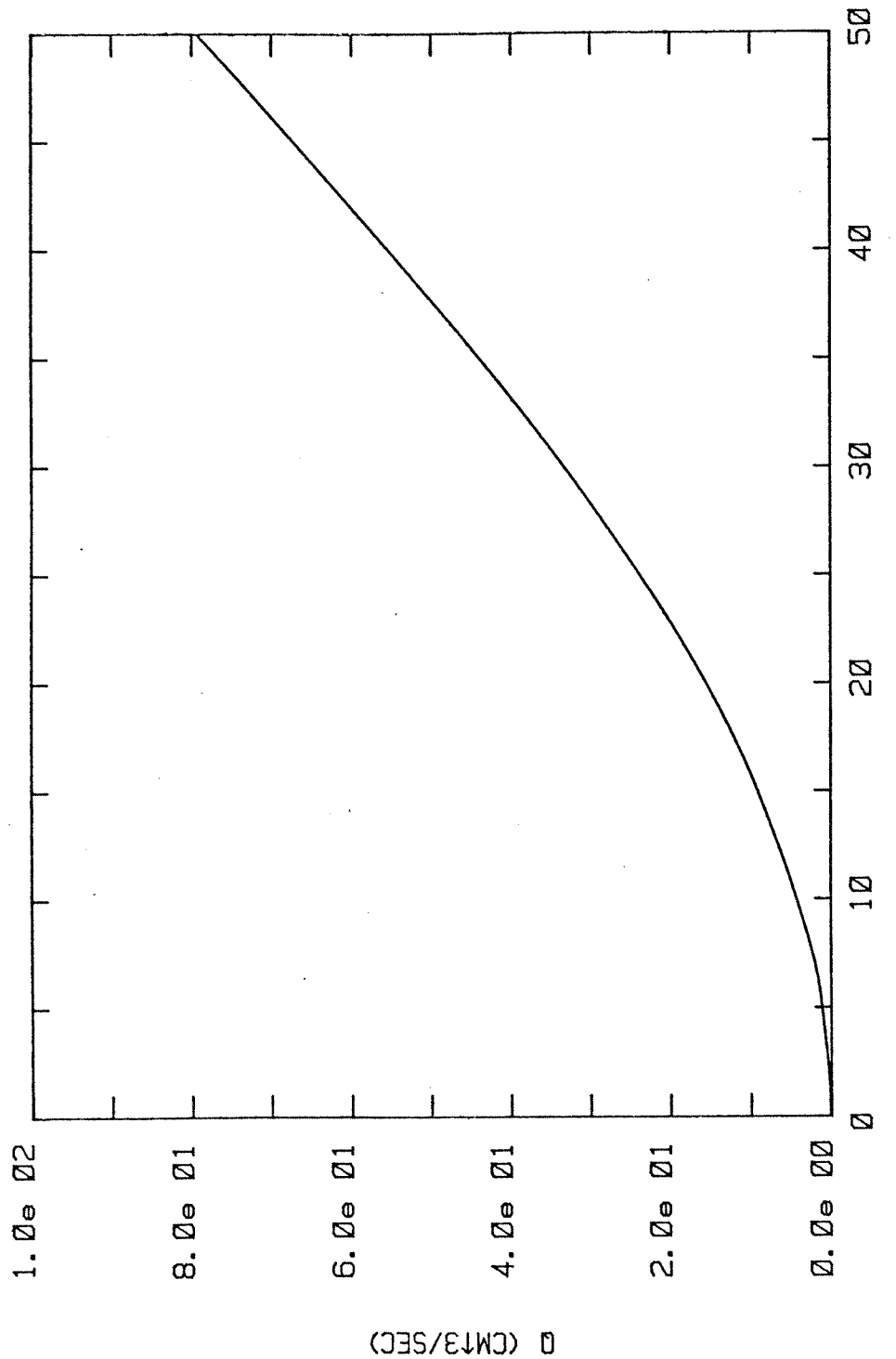

FIG. 4.7 AVERAGE SOURCE STRENGTH Q.

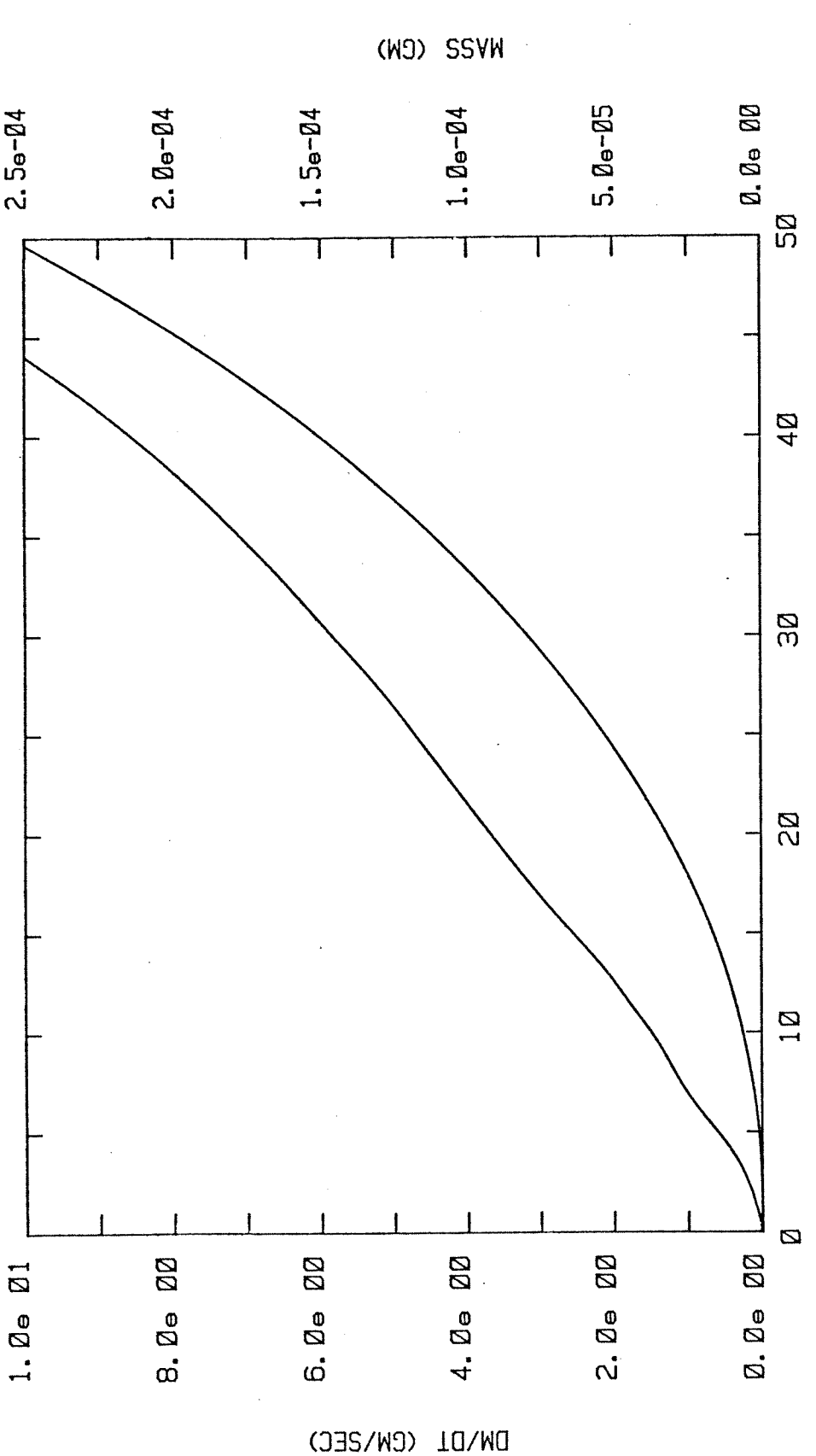

FIG. 4.8 TOTAL MASS IN BUBBLE, M AND ITS DERIVATIVE dM/dt.

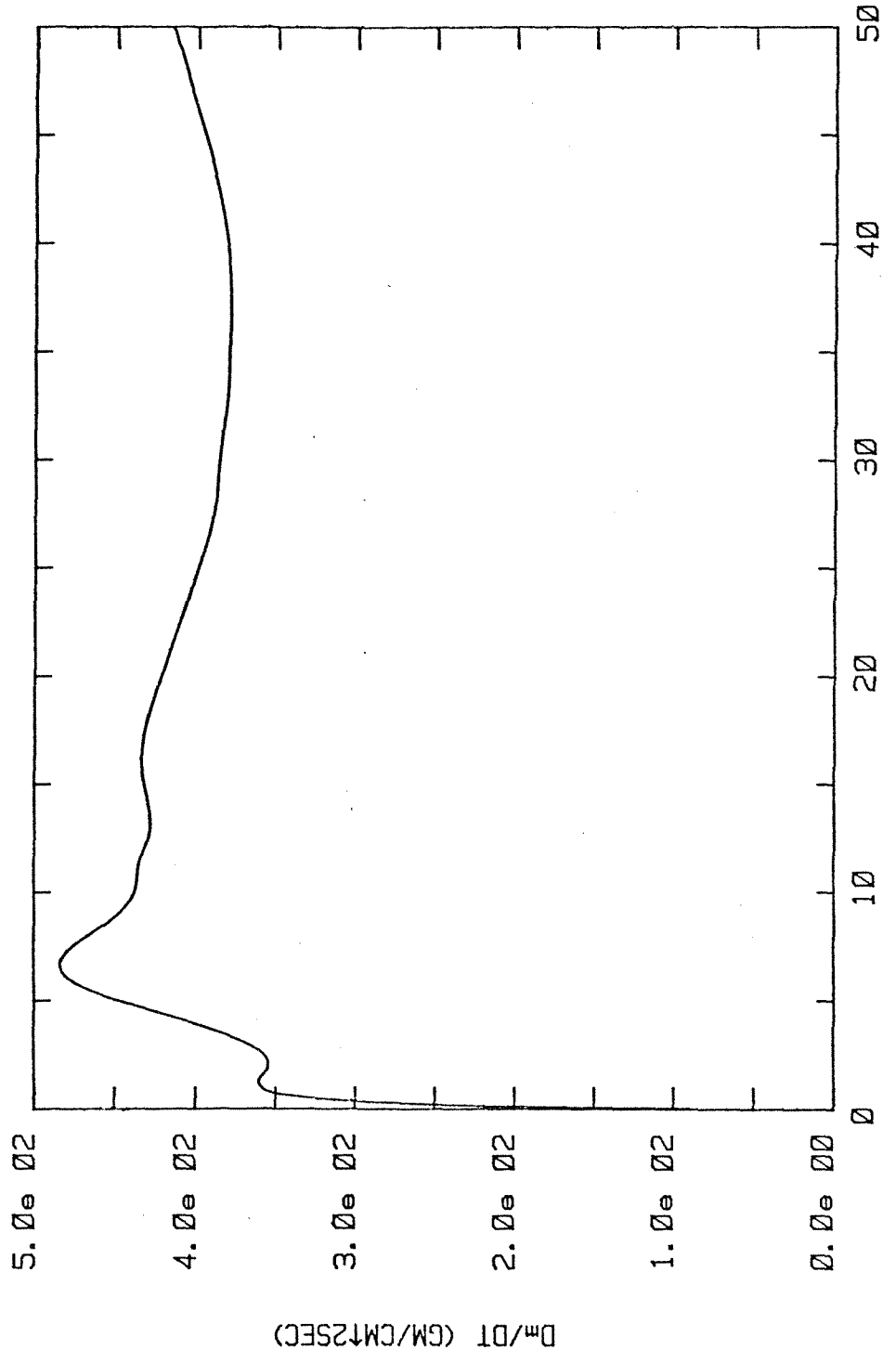

FIG. 4.9 AVERAGE EVAPORATIVE MASS FLUX, $\dot{m}$.

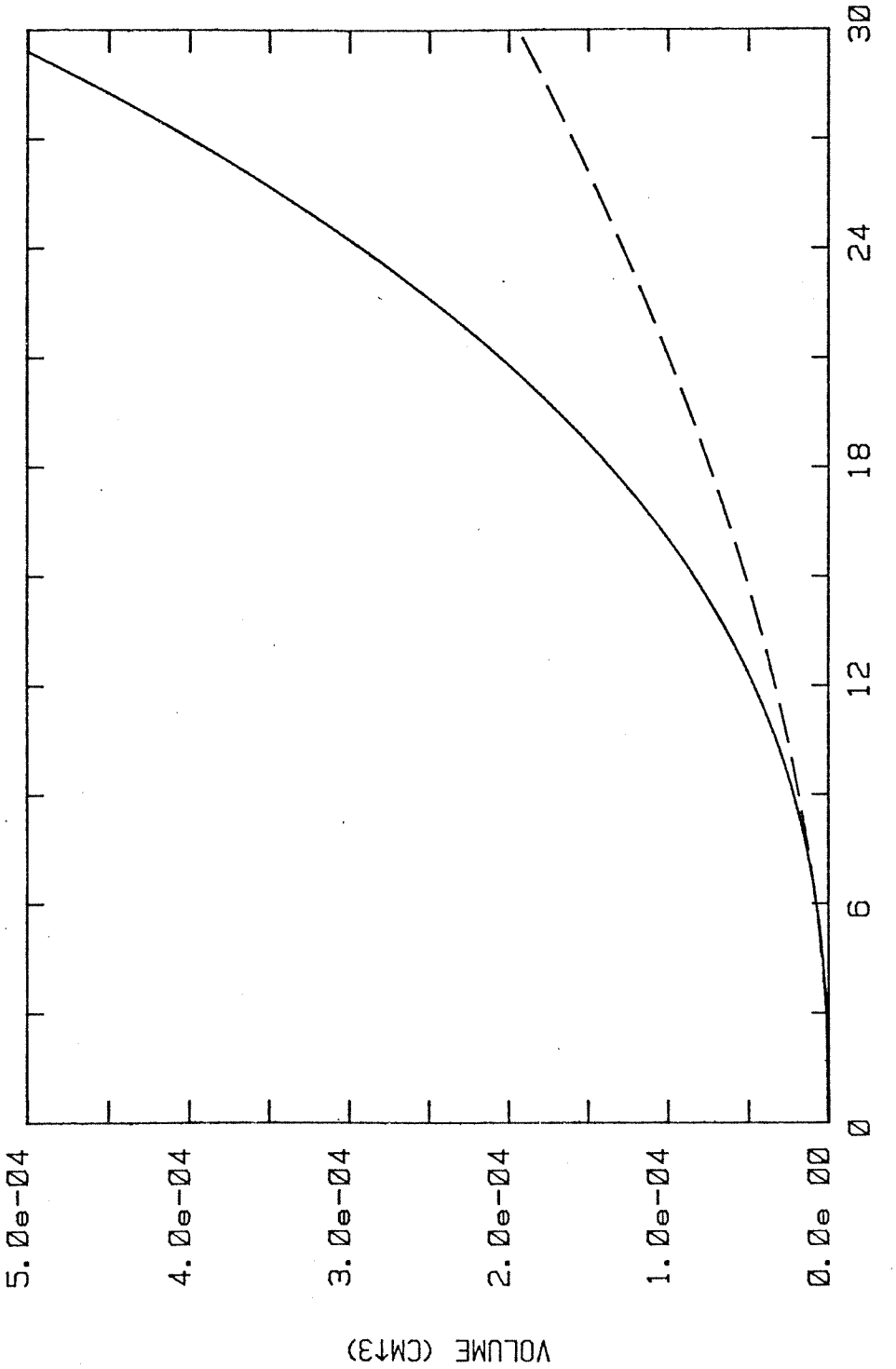

FIG. 4.10 BUBBLE VOLUME AS A FUNCTION OF TIME (____, EQUATION 4-9; ---, CLASSICAL MODEL).

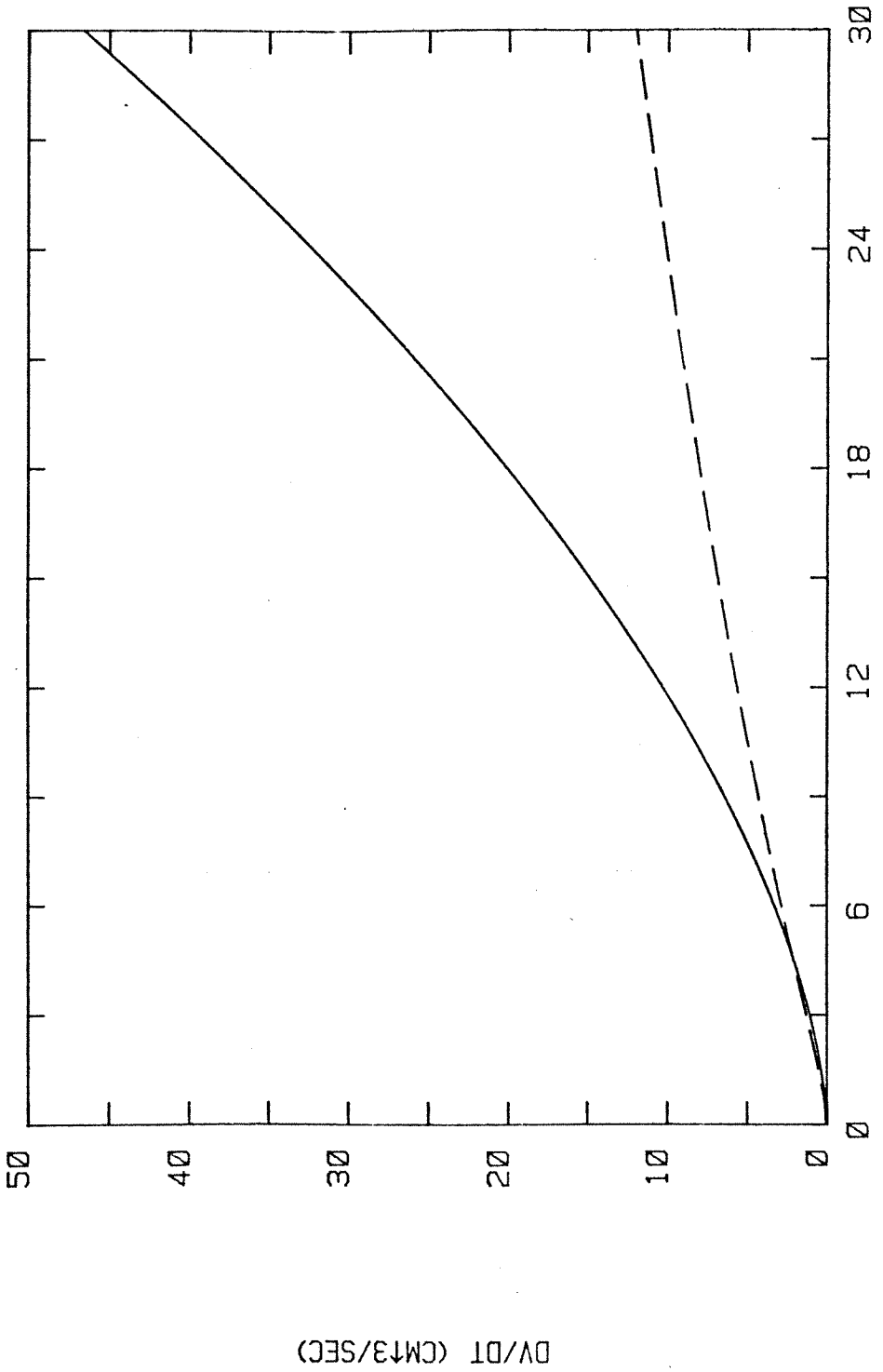

FIG. 4.11 BUBBLE VOLUME DERIVATIVE AS A FUNCTION OF TIME (____, EQUATION 4-9; ---, CLASSICAL MODEL).

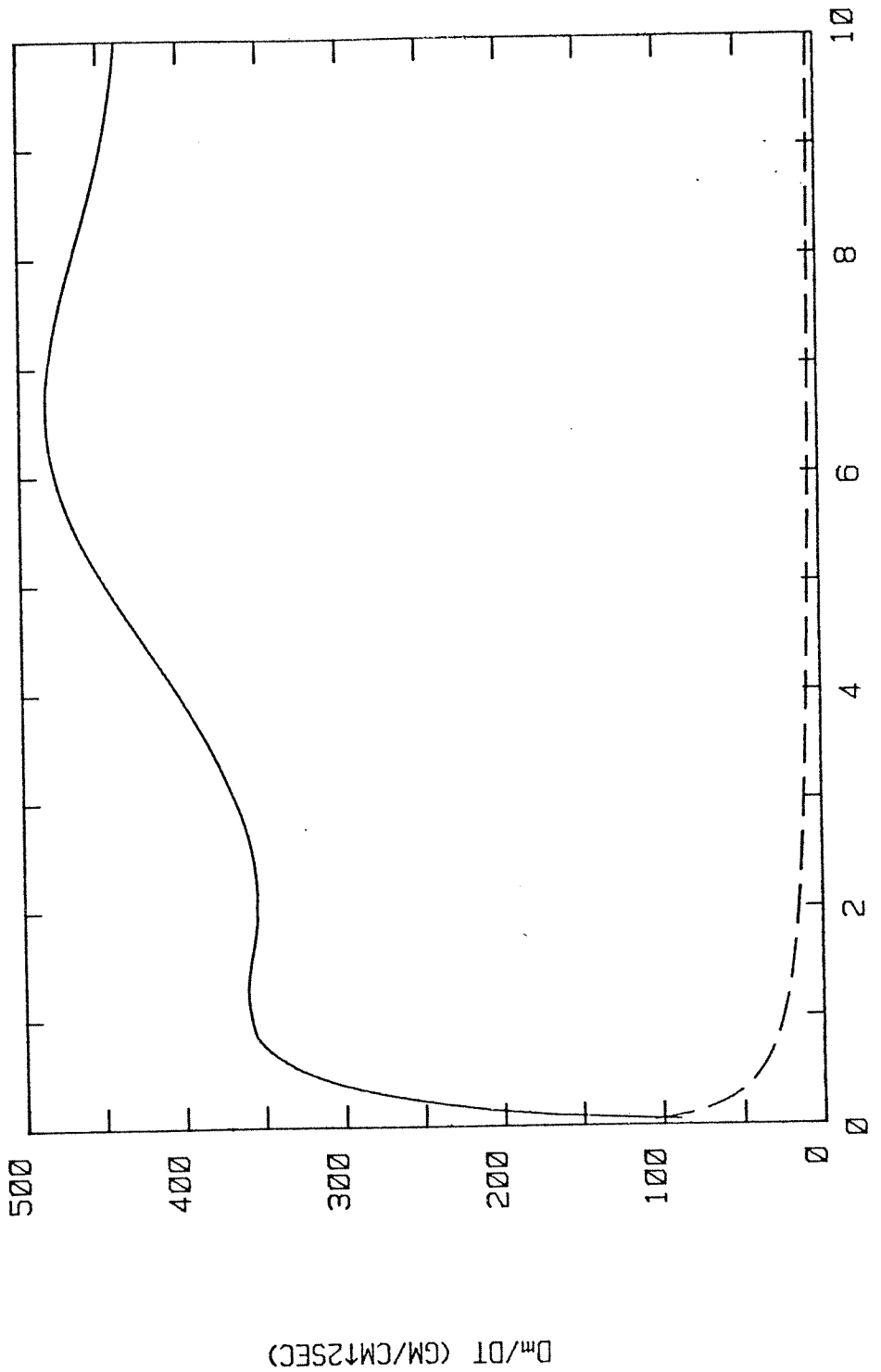

FIG. 4.12 AVERAGE EVAPORATIVE MASS FLUX AS A FUNCTION OF TIME (____, CALCULATED FROM EXPERIMENT; ---; CLASSICAL MODEL).

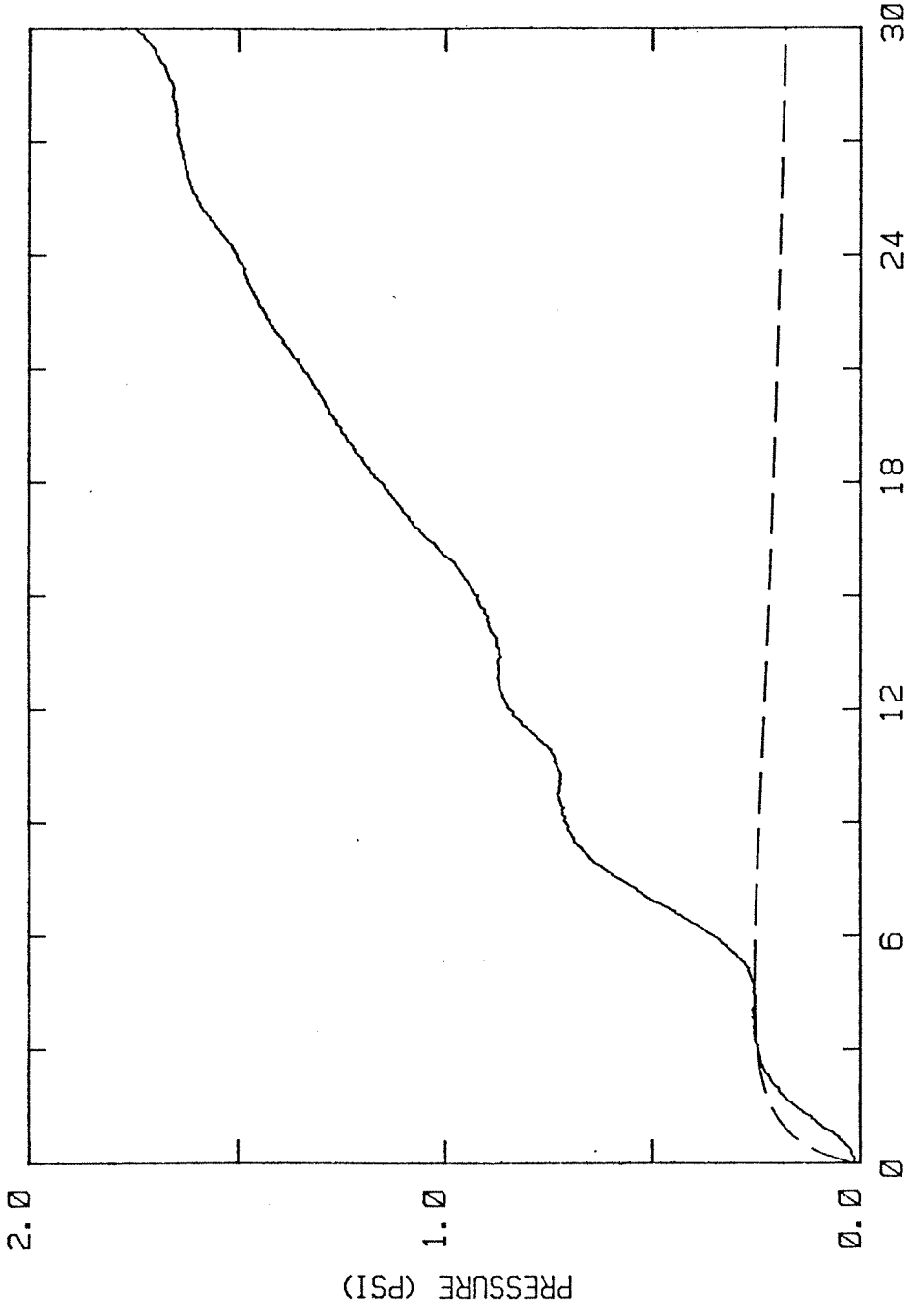

FIG. 4.13 PRESSURE SIGNAL 2.5 CM FROM BUBBLE (____, EXPERIMENT; ---, CLASSICAL MODEL, EQUATION 4-16).

V. LIQUID-VAPOR INTERFACE INSTABILITY

5.1 Introduction

The wrinkling of the evaporative surface observed in the present investigation presents a challenging problem: What is the underlying physical mechanism responsible for this phenomenon? In this chapter one possible mechanism, Landau instability, is proposed and the implications for the classical model of bubble growth are examined. Only the possible inception of surface distortion by this mechanism is considered and the more difficult nonlinear problem of the structure and dynamics of the persistent roughening is not addressed.

All bubble surfaces observed in the present study were wrinkled to some extent, including those bubbles seen at the earliest times. Unfortunately, since no bubbles younger than 8 μsec could be observed in these experiments, it was impossible to determine definitely whether the bubble surface was ever smooth. However, the regular appearance and small amplitude of the disturbances at the earliest times suggests that the surface may once have been smooth. Further, the classical theory of nucleation implies that the bubble is smooth at the very instant it is created from a fluctuation. On this basis, it will be assumed that the surface is initially smooth, and the stability of this smooth surface to perturbations in shape will be investigated.

This chapter is organized as follows: Results of the previous investigations of the linear stability of a plane evaporating surface are summarized in Section 5.2. Stability criteria and the physical basis of Landau instability are discussed in Section 5.3. Accounting for the effects of sphericity in an ad hoc way, the possibility of

instability during vapor bubble growth (described by the classical model) is investigated and the relation to the experimental observations discussed in Section 5.4. Digital image enhancement of the photographs of bubble surfaces at the earliest times is described and an example is presented in Section 5.5. Finally, the results of the stability analysis are summarized and some concluding remarks about the validity of the calculation are made in Section 5.6.

5.2 Review of Possible Instabilities

The linear stability of an idealized, steadily evaporating, plane liquid surface has been investigated by both Palmer (1976) and Miller (1973). Palmer identifies four distinct types of instability which explicitly are caused by evaporative flux:

a) Differential vapor recoil. Variations in surface temperature produce variations in the evaporation rate. The consequent variation in the recoil force due to the evaporative flux produces surface deformations, which, in turn, promote convection and so sustain the variations in surface temperature.

b) Inertial or Landau instability. Distortions of the evaporating surface produce vorticity in the vapor, which is convected downstream. The vorticity field feeds back to the interface to amplify the initial distortions of the surface, producing more vorticity.

c) Viscous dissipation. Distortions of the evaporating surface produce a variation in dissipation rate along the surface. The heating caused by dissipation promotes increased evaporation, which in turn sustains the surface deformation.

d) Moving boundary instability. Distortions of the evaporating surface are accompanied by changes in thickness of the adjacent

boundary layer, which in turn causes local variations in the heat flux into the surface. These heat flux variations result in evaporation rate changes which positively feedback to increase surface distortions.

All of these mechanisms can be stabilized to some extent by the action of surface tension, stabilizing accelerations, viscous dissipation and thermal diffusivity. Therefore, in each case the driving force, the evaporative mass flux, must exceed a threshold level before the instability occurs. These instabilities are not peculiar to evaporating liquid surfaces. Most have been proposed previously in various other contexts such as combustion, chemical reaction and solidification, i.e. any discontinuous change of phase in which fluid dynamics and/or heat release is important.

Conditions under which individual mechanisms dominate are extensively discussed by Palmer. However, the particular case of the initial stages of bubble growth at the superheat limit was not discussed, but, as outlined below, it can be inferred that the most likely instability is the inertial or Landau instability.

The inertial mechanism is the simplest possibility; it does not depend on a specific model of evaporation or require an intrinsic variation in surface temperature to support it. Neither viscosity nor thermal conductivity are essential; only a difference in density between liquid and vapor phases is required to produce vorticity. Further, the particular conditions of evaporation under consideration are not very favorable to the functioning of the other mechanisms. For the liquid-vapor density ratios found at the superheat limit, vapor recoil instability exists only in a very narrow range of conditions. The

moving boundary instability is manifested on very long wavelengths, which are effectively stabilized by the deceleration of the bubble surface. Viscosity is a very inefficient mechanism for producing instability and has a much higher threshold than the other mechanisms.

In addition to instabilities which are driven only by evaporation, there exist several other well known instabilities which are always possible at liquid-vapor interfaces. These include: e) Rayleigh-Taylor (driven by imposed accelerations); f) Kelvin-Helmholtz (due to a shear or discontinuity in the velocity parallel to the interface); g) Marangoni (due to convection induced by the temperature dependence of surface tension). The initial state of the unperturbed interface precludes possibility f) and the accelerations present in bubble growth are stabilizing, eliminating e). Surface tension gradients do not initially exist, but could arise as the result of other instabilities: In general, Marangoni type effects could be coupled to inertial (or any other) instabilities, but are not expected to be a primary source of instability at large evaporation rates.

Both Miller and Palmer suggest the possibility of an inertial type instability occurring for rapid evaporation. Indeed, Miller concludes that "the density difference effect could be of importance during rapid growth of cavitation bubbles under low pressure or tension." The conclusion of this chapter is to support that statement and generalize it to the possibility of instability in bubble growth from highly superheated liquids, especially at the superheat limit.

5.3 Physics of the Landau Instability

The inertial or Landau instability was first discussed by Landau (1944) in the context of laminar flames. An analysis (first made in

that paper) of the stability of a flame over a liquid will be applied here, without modification, to the stability of evaporating interfaces. At the level of approximation in the problem, the only difference between combustion and pure evaporation would be in the vapor density, which can be arbitrarily chosen anyway.

Heuristically, instability can be traced back to the generation of vorticity, in the initially irrotational flow, by the deformations of the interface.[1] This vorticity is convected downstream and is of such sign to induce velocities at the interface which amplify the surface distortions, further increasing the vorticity production. The situation is schematically indicated in Figure 5.1 for a two-dimensional flow. As indicated, spatial gradients in the perturbed (time dependent) pressure interact with density gradients (actually, the density jump across the interface) to produce the vorticity at the interface (this is just the baroclinic torque, $\nabla p \times \nabla \rho$, mechanism of producing vorticity). The vorticity field alternates in sign, with the period of the surface deformation, in the direction transverse to the flow and undergoes an exponential decay as it is convected downstream.

In the absence of any other forces on the interface, the surface is found to be unstable to deformations of any wavelength, smaller wavelengths having larger amplification rates. The effect of surface tension is to stabilize the interface to disturbances of short enough wavelength. The magnitude of the cutoff wavelength λ_c can be

---

[1] The author is indebted to Professor Frank Marble for the vorticity explanation presented here and the original suggestion that Landau instability was important.

estimated by equating the characteristic force/unit area on the interface due to surface tension σ

$$\frac{\sigma}{\lambda_c} \quad , \tag{5-1}$$

to the characteristic force developed by the instability

$$\dot{m}^2 \left(\frac{1}{\rho_v} - \frac{1}{\rho_\ell}\right) \quad . \tag{5-2}$$

The ratio of these two forces can be used to define a dimensionless parameter which will be referred to as the Inertia number N_I;

$$N_I = \delta \frac{\dot{m}^2}{\sigma} \left(\frac{1}{\rho_v} - \frac{1}{\rho_\ell}\right) \quad , \tag{5-3}$$

where δ is some scale length (which we will take for convenience to be 1 cm). In terms of the dimensionless wavenumber

$$K = \frac{2\pi\delta}{\lambda} \quad , \tag{5-4}$$

the precise criterion is: the interface is unstable when $K < N_I$, stable when $K > N_I$ and neutrally stable for $K = N_I$.

The effect of stable accelerations (accelerations of the liquid toward the vapor) is to damp out deformations of a long enough wavelength. The ratio of the accelerative forces to the surface tension forces is characterized by a dimensionless parameter referred to as the Weber number N_W;

$$N_W = g \frac{\Delta\rho\delta^2}{\sigma} \quad , \tag{5-5}$$

where $g = -\ddot{R}$, the deceleration of the bubble surface (N_W is often also known as the Bond or Eötvös number). With the inclusion of accelerations the stability criterion is modified to:

$$\frac{N_W}{K} + K > N_I \quad , \quad \underline{\text{Stable}} \quad ;$$

$$\frac{N_W}{K} + K = N_I \quad , \quad \underline{\text{Neutrally Stable}} \quad ;$$

$$\frac{N_W}{K} + K < N_I \quad , \quad \underline{\text{Unstable}} \quad .$$

It follows directly from the first inequality that for $N_I < 2\sqrt{N_W}$, the interface is absolutely stable to disturbances of all wavenumbers.

In the linearized analysis, unstable disturbances grow exponentially in time, i.e. all amplitudes $\propto e^{\Omega t}$. The growth rate Ω can be written in dimensionless form $\omega = T\Omega$, where the characteristic time $T = \frac{\delta}{\dot{m}}(\rho_v + \rho_\ell)$. From the analysis of Landau, which is repeated in the more accessible Landau and Lifshitz (1959), the dispersion relation $\omega = \omega(K, N_I, N_W, N_\rho)$, where $N_\rho = \rho_\ell/\rho_v$, can be written out directly

$$\omega^2 + 2\omega K + \frac{1-N_\rho}{N_\rho}\left(K^2 - \frac{N_W K + K^3}{N_I}\right) = 0 \quad . \qquad (5\text{-}6)$$

The stability criteria mentioned above, the most unstable wavenumber K^* and the corresponding amplification rate ω^* can all be derived from this relation. For sufficiently unstable flows ($N_I >> 2\sqrt{N_W}$), $K^* \propto N_I$, where the constant of proportionality varies between $\frac{1}{2}$ and $\frac{2}{3}$ as N_ρ varies between 1 and ∞; corresponding amplification rates are $\omega^* \sim N_I(N_\rho - 1)$. Curves of constant growth rate, the neutral stability boundary and the most unstable wavenumber K^* are plotted on the K vs. N_I plane in Figure 5.2 (N_ρ and N_W are held constant).

There is an even more compact, but not necessarily simpler,

choice of dimensionless parameters. If $K/\sqrt{N_W}$ and $N_I/\sqrt{N_W}$ are used as the new variables, then the parameters can be combined and the dispersion relation written,

$$\omega = \omega(K/\sqrt{N_W},\ N_I/\sqrt{N_W},\ N_\rho) \quad . \tag{5-7}$$

No further consideration or use of (5-7) will be made.

5.4 Application to the Classical Model of Bubble Growth

The theory developed by Landau is based on an initially plane interface in a steady flow. Strictly speaking, application of the results to nonsteady spherical interfaces could only be justified if the disturbance wavelength is much smaller than the bubble radius and the disturbance growth rate is much faster than the rate characterizing bubble growth. It is not known in advance whether these conditions will always be met and the success of the application will be judged afterwards. Intuitively, the effect of sphericity is to suppress all disturbances with wavelengths of the order of or larger than the bubble dimensions. To account for this effect an arbitrary cutoff wavenumber k_R, corresponding to a wavelength of one drop radius, will be introduced. The possible unstable modes will be calculated as though the interface were plane, but only disturbances of wavenumber $k > k_R$ will be considered as actual unstable modes of the spherical interface. In particular, if all possible unstable modes have wavenumbers $k < k_R$, then the spherical interface will be considered stable.

The cutoff wavenumber method of correcting the planar instability theory for the effects of spherical geometry can be tested for the special case of nonevaporating bubbles, for which the spherical

case (described in Appendix C) has been worked out exactly. The exact theory does indeed predict the usual Taylor instability ($\ddot{R} > 0$) will be suppressed if the bubble radius is small enough. As assumed in the evaporating case, the exact criterion for damping in the non-evaporating case can be stated in terms of a cutoff wavenumber based on the radius; more precisely, the cutoff wavelength is ~ 1.7 R. For this particular example, the cutoff wavenumber idea does account for the major effect of the spherical geometry, although more subtle effects such as algebraic growth of instabilities associated with the radial motion of the surface cannot be treated by this method.

Neglecting the effect of accelerations, the Inertia number N_I and the normalized cutoff wavenumber K_R have been calculated as a function of time during bubble growth. The approximate formulas of universal bubble growth (Mikic et al, 1970) described in Section 4.5 were used in this calculation. The path of the system is shown on the $K - N_I$ plot, Figure 5.3; the region of possible instability lies in the shaded area below $K = N_I$ and above K_R. This calculation does indeed indicate that in the interval $\sim 10^{-9}$ sec to 2×10^{-5} sec bubble growth would be unstable. Outside of this range the bubble radius is smaller than the shortest possible instability wavelength, $K_R > N_I$. If accelerations are included, the main effect is to decrease the length of the interval over which the motion is unstable to $10^{-9} - 2 \times 10^{-6}$ sec. The accelerations referred to here are actually decelerations of the interface ($\ddot{R} < 0$) as the bubble transitions from the inertial to asymptotic stage; the order of magnitude of $\ddot{R}$ is 10^8 cm/sec^2 (10^5 g). In Table 5.1, the Inertia number, Weber number, cutoff wavenumbers, growth rate and most unstable

wavenumbers are tabulated as a function of time during bubble growth. The growth rates and most unstable wavenumbers have been calculated for the purely surface-tension-stabilized interface.

Also shown on Figure 5.3 is the region corresponding to the conditions at the interface of the regularly wrinkled bubbles observed experimentally at the earliest times. The range in K of this region corresponds to the range of disturbance scale sizes observed in the earliest photographs (this point is considered in more detail in the next section); the range of values of N_I correspond to the inferred mass flux of 400 gm/cm^2 sec and the possible range of surface tensions in metastable butane (3-16) dynes/cm) and vapor densities (0.05-0.1 gm/cm^3) that may occur in the experiments.

A possible interpretation of the experimental data can be made by recognizing that the linear instability must have occurred well before 8-10 μsec. All the experimental data refer then to the fully developed, nonlinear stage of the instability. This is consistent with the results of Chapter 4 (e.g. Figure 4.9), which suggests large and rapid changes in the mass flux occur in the first 1-2 μsec. Assuming that the most unstable wavelength chosen by the linear amplification process is "frozen in" when the growth reaches the nonlinear stage, the range of wavelengths observed at 8 μsec and the ad hoc model of instability (excluding accelerations) imply that linear instability could have occurred about 1.0 μsec. However, the effect of accelerations is to terminate the instability at 0.3 μsec. Corresponding instability wavenumbers at this time are 2-10 times larger than those observed at 8-10 μsec, implying that a large decrease in wavenumber must have occurred during the nonlinear stage if the present explanation is, in fact, correct. Further work is in progress on the exact linear instability theory in an effort to clarify this situation.

Thus, the bubble could have grown according to the classical model until about 0.3 μsec, at which time the linear instability occurred and consequently, the mass flux increased. Following the onset of instability, the mass flux and bubble growth rate rapidly increased until the instability growth saturated at a mass flux 10^2 larger than in the absence of instability. This rapid increase of mass flux corresponds to a sharp veer to the right of the (N_I, K_R) trajectory (on Figure 5.3 from the classical path at about 0.3 μsec to the region experimentally observed at 8 - 10 μsec.

5.5 Image Processing and Experimental Evidence of Instability

As proposed above, the experimental observations of a roughened evaporating surface and an abnormally large evaporative mass flux could both be explained by a fundamental instability of the evaporating interface. Photographs of the bubble at the earliest times (e.g. Figures 3.2 and 3.10) are the most direct experimental evidence that this instability developed from an initially smooth surface. Bubble surfaces in these photographs appear covered by a fairly regular pattern, that could be produced by surface deflections or waves. Such waves may have originally been formed in the first few microseconds of bubble growth by the linear instability process described in the preceeding sections. This idea is the motiviation for comparing (in Figure 5.3) the length scale of the intensity variations making up the pattern on the bubble surface to the most unstable wavelength of the linear instability theory. An order of magnitude of the length scale can be obtained simply by estimating the average distance between dark (or light) patches on the pattern. For example, the bubble seen in print (a), Figure 3.10 has a 150 μm radius and the length scale of the pattern is 20-40 μm.

To obtain a clearer idea of the organization (if any) present in the pattern and a better estimate for the length scale, several bubble images taken at the earliest times were digitized and computer processed to enhance the pattern.[2] An example of the results can be seen in Figure 5.4; print (a) is a contrast enhanced (stretched) but otherwise unprocessed image of the bubble seen in print (a), Figure 3.10; print (b) is the enhanced version. The processing used to enhance the image was: a) the original gray level data, contained in a 64 x 64 array of pixels, was expanded to a 512 x 512 array using linear interpolation; b) a 3 x 3 median filter (each pixel gray level is replaced by the median level of the surrounding 3 x 3 square of pixels) was applied; c) a high pass filter, with a cutoff length of 13 pixels, was applied; d) finally, the contrast scale was stretched (linearly) to accentuate the difference between light and dark areas of the pattern.

The enhanced image shows that the pattern covers the entire bubble, and in particular that it occurs at the periphery, where the unprocessed version appears uniform. The regularity of the pattern is much more striking in the enhanced image, but there is substantial asymmetry and randomness. This is consistent with the possibility that linear instability occurred at about 0.3 μsec whereas the experimental observations are made at 8 μsec, well into the nonlinear regime. The possibility exists that a more rigorously defined length scale could be computed from digital data representing the picture, e.g. a characteristic length could be determined from the 2-D autocorrelation of the image. However, the complexity of the image (i.e. the presence of the circular boundary of the bubble and the nonuniform background due to the lensing effect of the bubble) prevents

[2]The author would like to thank Daryl Madura and the staff of the Medical Imaging Analysis Facility of the Jet Propulsion Laboratory for performing this work.

a simple interpretation of the autocorrelation function and the best estimate of scale size remains that determined above by human judgement.

5.6 Summary

The purpose of this chapter was to investigate the possibility that the evaporating bubble surface is fundamentally unstable at the conditions of the superheat limit found in the present study. Out of 7 possible instabilities, the Landau or inertial instability was chosen as being the most likely to occur. Landau's original analysis of a flame over a plane liquid surface was supplemented by an ad hoc sphericity condition and the resulting theory applied to the classical model of bubble growth. Taking into account the stabilizing effects of both surface tension and deceleration, the bubble surface was found to be unstable for the portion 8×10^{-9} to 3×10^{-7} sec of the initial growth.

Experimentally, the observations made in the present study at 8 μsec show regular disturbances with a scale length (20-40 μm) on the order of the unstable wavelengths predicted by the linear theory to occur at about 0.3 μsec. An explanation consistent with all the available evidence and the theory is that the observed instability at 8 μsec is far into the nonlinear stage and the linear stage of the instability did occur in the first 1-2 μsec of bubble growth. Observed length scales are 2-10 times those predicted by the linear instability theory; this may be due to the nonlinear growth process and is a point requiring further investigation.

Of course, the calculation carried out in Section 5.4 does not rigorously prove that Landau instability will occur. Indeed, the ad

hoc method of including sphericity suggests that only modes represented by a small band of wavenumbers ($K_R < K < N_I$) can be unstable at any time. Further, the growth rates of these unstable modes are such that interaction between the bubble growth and instability development must be important. Inspection of Table 5.1 reveals that the product of instability growth rate and time is nearly a constant over the unstable region. Algebraic growth, rather than exponential growth, would characterize such a process. However, both the narrow band of unstable modes and the algebraic instability are plausible effects that are known to occur in the related instability of nonevaporating spherical surfaces discussed earlier and in Appendix C.

In addition to the difficulties associated with the approximate nature of the calculation, there is the possibility that the bubble growth could be unstable from the very outset. The surface-tension-controlled stage of bubble growth, which is not included in the universal growth model used in this calculation, is characterized by positive, Taylor unstable, accelerations ($\ddot{R} > 0$). Since the duration ($\sim \tau = 10^{-10}$ sec) of this stage is short, the accelerations can be enormous, $\ddot{R} \sim 10^{12}$ cm/sec^2. The possibility of instability at the earliest stage due to these accelerations alone can be investigated using the exact linear stability theory (reviewed in Appendix C) developed for the surfaces of nonevaporating, but unsteady, bubbles. In fact, under the conditions at the superheat limit of butane given by the conventional theory of nucleation, this exact theory predicts no instability will occur. This is due to the cutoff effect of the bubble radius; the most unstable wavelength for a plane interface

under the same conditions is 10^2 larger than the critical nucleus radius $R_o = 4 \times 10^{-7}$ cm.

REFERENCES

Landau, L.D. 1944 "On the Theory of Slow Combustion", Acta Physiochimica U.R.S.S. 19, 77.

Landau, L.D. and Lifshitz, E.M. 1959 Fluid Mechanics, Pergamon Press, New York, 479.

Miller, C.A. 1973 "Stability of Moving Surfaces in Fluid Systems with Heat and Mass Transport - II. Combined Effects of Transport and Density Difference Between Phases", AIChE Journal 19, 909.

Palmer, H.J. 1976 "The Hydrodynamic Stability of Rapidly Evaporating Liquids at Reduced Pressure", J. Fluid Mech. 75, 487.

TABLE 5.1

LANDAU INSTABILITY PARAMETERS FOR BUBBLE GROWTH

t (μsec)	K_R	N_W	N_I	K^*	Ω (sec^{-1})
0	1.7×10^7	∞	2.1×10^5	1.4×10^5	-
0.02	7.9×10^4	6.7×10^8	1.1×10^5	7.3×10^4	1.6×10^8
0.2	8.6×10^3	1.4×10^8	4.5×10^4	3.0×10^4	2.7×10^7
2.0	1.1×10^3	1.6×10^7	4.9×10^3	3.3×10^3	2.5×10^6
20.0	1.4×10^2	8.4×10^5	1.2×10^2	8.0×10^1	-
200.0	5.4×10^1	2.9×10^4	1.2×10^1	8.0	-

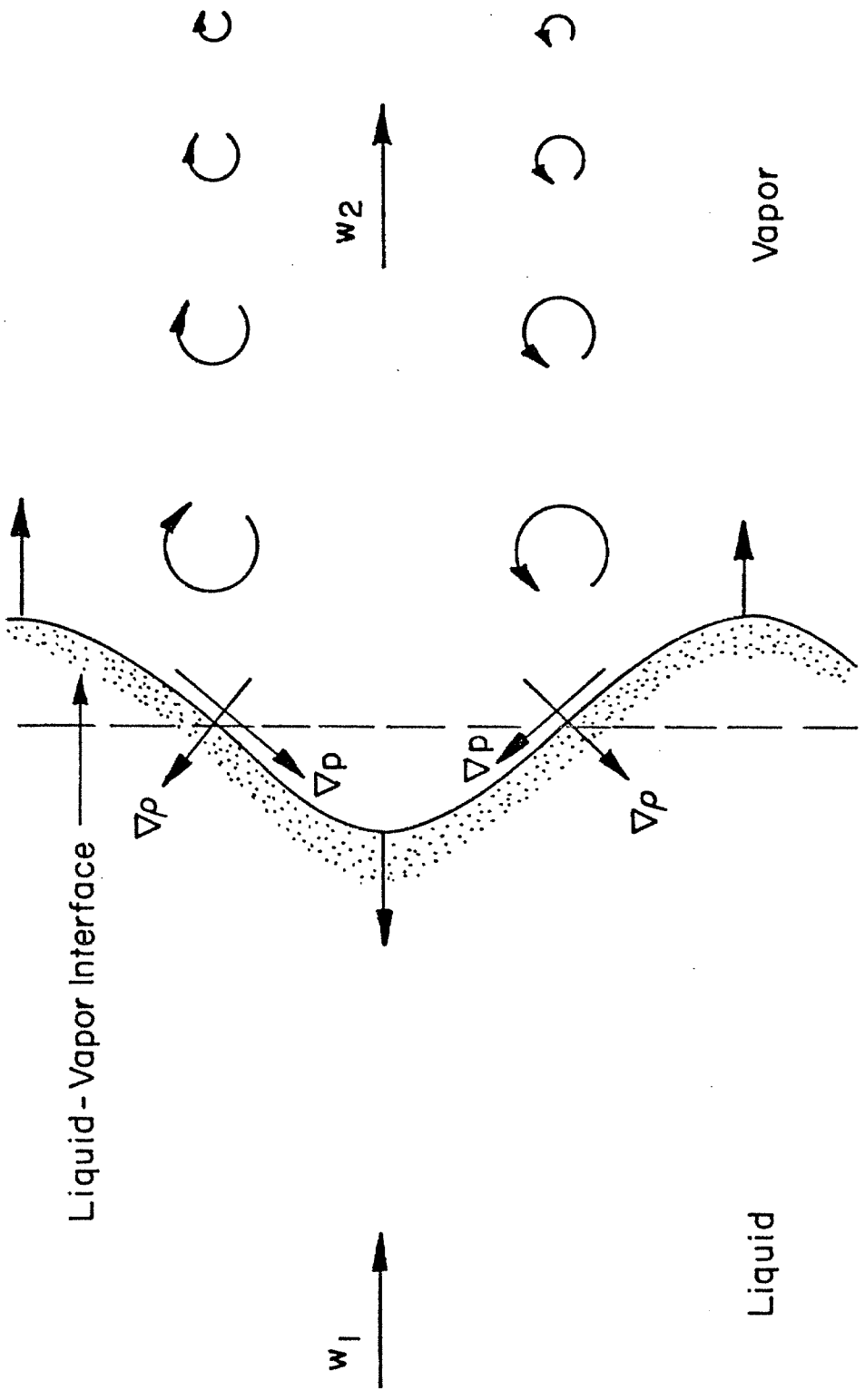

FIG.5.1 VORTICITY GENERATION MECHANISM OF LANDAU INSTABILITY OF EVAPORATING INTERFACE

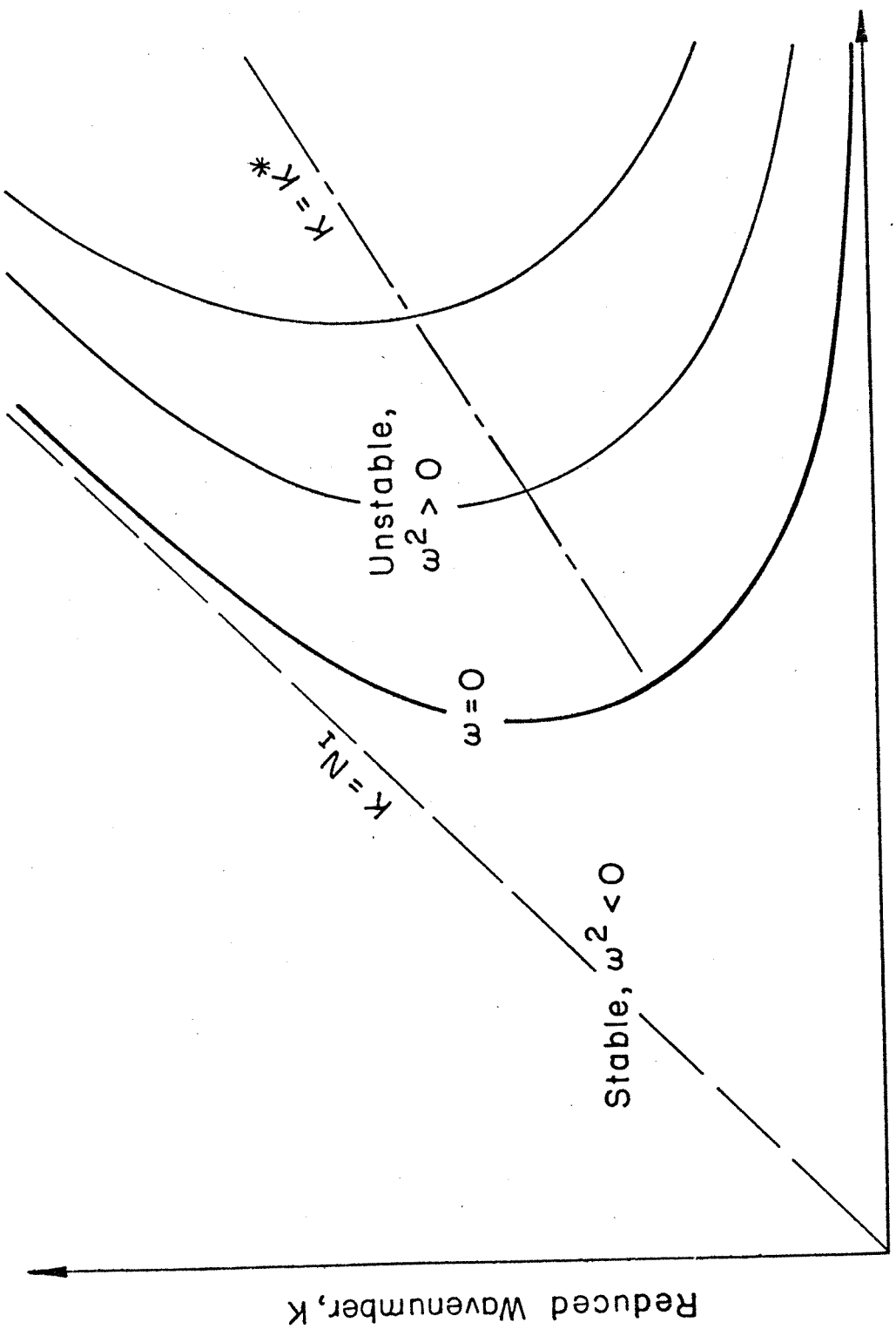

FIG. 5.2 STABILITY PLOT FOR LANDAU INSTABILITY, INCLUDING BOTH SURFACE TENSION AND ACCELERATION

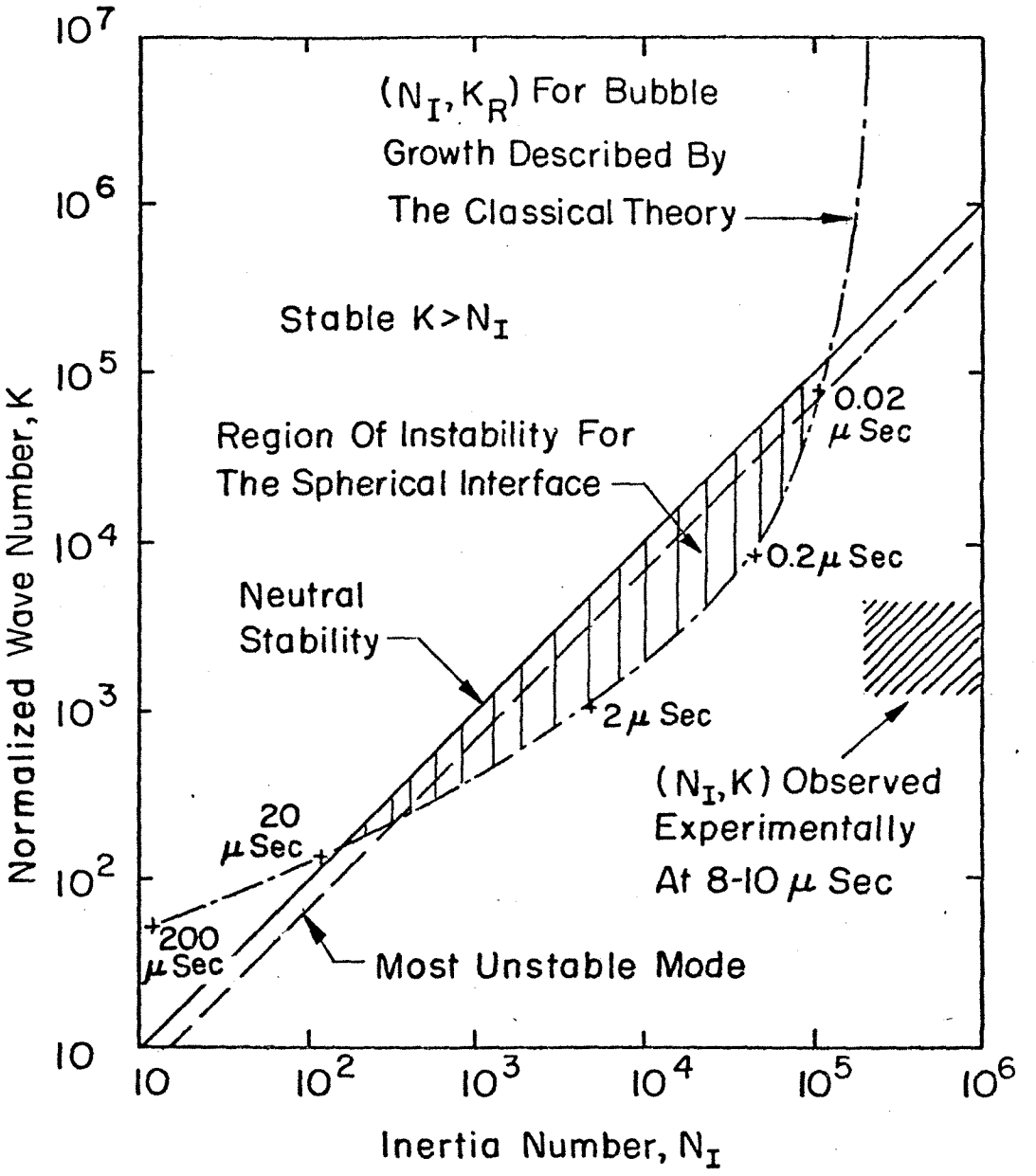

FIG. 5.3 REGION OF INSTABILITY FOR BUBBLE GROWTH DESCRIBED BY THE CLASSICAL MODEL AND COMPARISON TO THE EXPERIMENTAL OBSERVATIONS AT 8 – 10 μ SEC

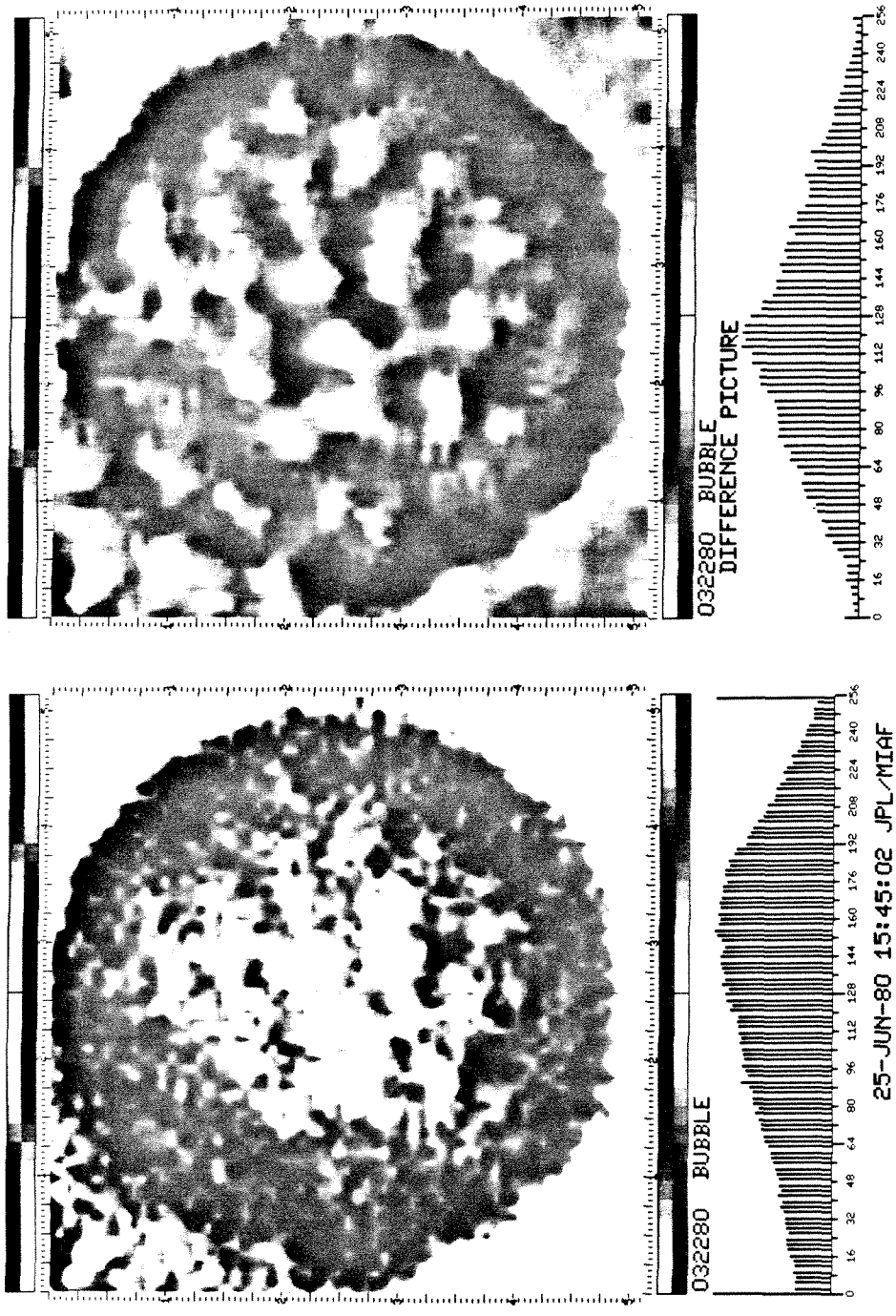

FIG. 5.4 COMPARISON OF UNPROCESSED(a)AND PROCESSED (b) BUBBLE IMAGES

VI. A ONE-DIMENSIONAL ANALOG OF THE CLASSICAL MODEL AND SOME LIMITATIONS AT THE SUPERHEAT LIMIT

6.1 Introduction

Throughout the previous chapters, frequent reference has been made to the "classical model" of bubble growth and its failure to adequately describe the experimental observations made in the present work. One possible limitation of the classical model was considered in Chapter 5; namely, that the evaporating bubble surface is intrinsically unstable at large evaporation rates. Aside from this fundamental limitation, there are others due to the approximate character of the theory and the possible violation of key assumptions at the extreme conditions encountered at the superheat limit. Key assumptions which may not be valid under conditions of rapid evaporation include: equilibrium of liquid and vapor at the evaporating surface; neglect of the dynamics of the vapor inside the bubble; and the neglect of the flux of liquid toward the interface in the calculation of heat transfer in the liquid.

No attempt will be made here to comprehensively discuss any of these issues or develop a less restrictive theory. However, to illustrate the issues we will set up and solve a simplified one-dimensional version of the classical model. This simplified model uses compressible dynamics (acoustics) instead of the usual incompressible bubble dynamics, but otherwise uses the same kind of approximations, and the solution has the same character, as the classical spherical bubble growth. In the context of this geometrically simplified model, the limitations of one particular approximation, namely the neglect of differential liquid-interface motion in the heat transfer problem, will be examined.

Under the conditions of very rapid evaporation, the flux of liquid into the evaporating surface also represents a substantial convection of thermal energy into the thermal boundary layer adjacent to the surface. This convective heat transfer has a fundamentally different character than the usually assumed diffusive heat transfer. In particular, such convection can support a steady-state evaporation process under the appropriate conditions. Clearly, this implies the possibility of a completely different picture of bubble growth in highly superheated liquids than previously obtained from the classical, diffusion-limited theory.

6.2 One-Dimensional Version of the Classical Model

In this section the one-dimensional analog of the classical model of bubble growth is developed and, under certain approximations, solved analytically. By one-dimensional analog is meant the growth of a region of vapor ("planar bubble") bounded by two parallel evaporating surfaces adjoined by infinite regions of superheated liquid. Obviously, the problem is symmetric so that only half of the bubble and one evaporating surface has to be considered. All motion, heat transfer and variation of physical properties occurs only in the direction normal to the evaporating surface.

The coordinate system and basic notation is shown in Figure 6.1; vapor fills the region between the center of the bubble $x = 0$, and the right hand evaporating surface $x = X(t)$. To the right of the evaporating surface, $X(t)$, is superheated liquid moving with velocity $u(x,t)$. At the bubble surface, the velocity in the liquid will be denoted u_s,

$$u_s(t) = u(X(t), t) \quad .$$

The initial undisturbed conditions in the liquid are $p = p_\infty$, $T = T_\infty$ and $u(x, 0) = 0$. The interface starts at the origin $x = 0$ at time $t = 0$ and subsequently moves to the right with a velocity $\dot{X}(t)$, pushing the liquid ahead of the interface and radiating pressure waves. At the interface, there is a net evaporative mass flux $\dot{m}$ from the liquid into the vapor. Therefore, the liquid velocity at the interface, u_s, will be less than the interface velocity $\dot{X}$ by an amount determined by the conservation of mass,

$$\dot{m} = \rho_\ell(\dot{X} - u_s) \quad ,$$

where ρ_ℓ is the liquid density. The "differential liquid-interface motion" referred to in the introduction of this chapter is merely this difference between $\dot{X}$ and u_s.

The liquid is assumed to be slightly compressible so that disturbances generated at the evaporating interface are propagated out into the undisturbed liquid with the speed of sound c. Other than this, the approximations of the classical model as set forth by Prosperetti and Plesset (1978) are used to describe the vapor dynamics, evaporation process and heat transfer. The most important of these are given below for completeness:

a) Conditions in the vapor are uniform and are taken to be those of the saturated vapor at the temperature of the bubble surface T_s, i.e. throughout the bubble the vapor density is $\rho_v(T_s)$ and the vapor pressure is $p_v(T_s)$. The dynamics of the vapor inside the bubble and at the interface are neglected.

b) Boundary conditions at the interface are simplified by assuming: the pressure difference due to the momentum flux is negligible, $p_v(T_s) = p_s$; the interface-liquid velocity difference due to

mass flux is negligible, $u_s \doteq \dot{X}$; and the enthalpy difference between liquid and vapor is the same as for the equilibrium liquid-vapor surface, i.e. the kinetic energy of the flow is assumed to be negligible and the heat flux $\dot{q}$ into the interface is determined only by the mass flux $\dot{m}$ and the latent heat L,

$$\dot{q} = L\dot{m} \quad . \tag{6-1}$$

c) The heat transfer problem is simplified by assuming that only the conduction in the liquid is important

$$\dot{q} = - k_\ell \frac{dT_s}{dx} \tag{6-2}$$

and convection is negligible, i.e., there is no differential interface-liquid motion. Further, the heat transfer is all assumed to take place in a thin thermal boundary layer of thickness δ adjacent to the evaporating surface.

Later, additional approximations will be made in order to obtain an analytical solution to the problem. These approximations are the same as those used by Prosperetti and Plesset (1978) in deriving the universal model of bubble growth mentioned earlier in Chapter 4.

Before going into the details of the model a simplified physical picture of bubble growth (from the classical point of view) will be given. This picture is valid for both spherical and planar cases except that a stage of spherical growth dominated by surface tension has been omitted. The motion of the bubble is determined by two processes: first, the rate at which fluid can be pushed out ahead of the growing bubble, and, second, the rate at which vapor can be evaporated into the bubble. The first rate is determined by the

inertia of the liquid (i.e. for spherical bubbles, potential flow) and the driving force exerted on the liquid (i.e., the vapor pressure in the bubble). The second rate is determined by heat transfer at the bubble surface and the requirement that the vapor always be in equilibrium with the liquid. The crucial coupling between these two rates occurs at the bubble surface, whose temperature determines the magnitude of the driving force (vapor pressure) and in turn, is determined by the heat transfer accompanying the evaporative mass flux.

At early times in the bubble growth, little heat transfer has taken place and the bubble surface temperature is just slightly lower than ambient. This initial period is referred to as the "inertial stage" since the vapor pressure is roughly constant and pushes the bubble surface out as fast as liquid dynamics (inertia) will allow. As bubble growth proceeds, the cumulative effects of heat transfer reduce the interface temperature; hence, the vapor pressure falls and the bubble growth rate decreases. Asymptotically, as $t \to \infty$, the bubble pressure tends toward p_∞ and the growth is strictly diffusion-limited, then the bubble "radius" $R(t)$ (or, in the one-dimensional case, $X(t)$) $\sim t^{1/2}$.

The details of the model are logically separated into two parts: first, the heat transfer will be discussed in Section 6.2.1; second, the liquid dynamics (acoustics) will be discussed in Section 6.2.2. The model equations will be summarized and the approximate universal equation solved in Section 6.2.3.

6.2.1 Heat Transfer

The heat transfer problem is to determine the interface

temperature T_s as a function of the heat flux into the interface. Under the assumptions of this model only the diffusive transport is important, and then only within a thin boundary layer adjacent to the interface where the liquid velocity is constant. In interface-fixed coordinates the boundary layer problem is identical to the one-dimensional transport of heat in an initially uniform semi-infinite solid, with the flux prescribed as a function of time on the boundary. It is a standard problem whose solution can be found in Carslaw and Jaeger (1959, p. 76), and, in terms of the temperature gradient $\frac{dT_s}{dx}$ at the interface,

$$T_s = T_\infty - \left(\frac{\kappa_\ell}{\pi}\right)^{1/2} \int_0^t \frac{\frac{dT_s}{dx}(\tau)}{\sqrt{t-\tau}}\, d\tau \quad . \tag{6-3}$$

This solution is identical to the limit $R \to \infty$ of the solution to the spherical case (Plesset and Zwick 1952), a solution universally used in the conventional models of bubble growth.

In order to connect this solution to the bubble growth, equations 6-1 and 6-2 must be used to determine the temperature gradient at the interface as a function of the mass flux. Mass flux can then be related to the bubble size $X(t)$ by the overall mass balance of the bubble

$$\dot{m} = \frac{d}{dt}\left(X\rho_v(T_s)\right) \quad . \tag{6-4}$$

6.2.2 Liquid Dynamics

The acoustic formulation of the problem is used in the one-dimensional case since incompressible dynamics of a semi-infinite

one-dimensional fluid are trivial. Only waves propagating away from the interface into the liquid are considered. From acoustics, the perturbation pressure p' is related to the fluid velocity perturbation δu by

$$p' = \rho c \delta u \quad , \tag{6-5}$$

where ρc is the acoustic impedance of the liquid. Under the assumptions (b) of this model, in the liquid adjacent to the interface the perturbation pressure is $p' = p_v(T_s) - p_\infty$ and the velocity is $\delta u = \dot{X}$. Altogether, at the interface

$$p_v(T_s) - p_\infty = \rho c \dot{X} \quad , \tag{6-6}$$

which, together with equations 6-1 through 6-4 and the saturated vapor thermodynamics, $\rho_v(T_s)$ and $p_v(T_s)$, forms the complete set of equations for this model.

6.2.3 Summary of the Model and Its Approximate Solution

Combining the previous equations and simplifying, the following pair of equations for T_s and X result

$$\begin{aligned} T_s &= T_\infty - \left(\frac{k_\ell}{\pi}\right)^{1/2} \int_0^t \frac{L(T_s)}{k} \frac{\frac{d}{d\tau}\left(\rho_v(T_s)X\right)}{\sqrt{t-\tau}} \, d\tau \\ p_v(T_s) &- p_\infty = \rho c \dot{X} \quad . \end{aligned} \tag{6-7}$$

For general ρ_v, p_v and L these equations must be simultaneously solved by numerical integration. However, as shown by Prosperetti and Plesset (1978) for the analogous spherical model, further approximation yields a single, more tractable equation with solutions similar in form to those of (6-7). The necessary approximations are that the vapor pressure depends linearly on temperature

$$p_v(T_s) - p_v(T_\infty) = A(T_s - T_\infty) \quad , \tag{6-8}$$

and the vapor density and latent heat are constants independent of interface temperature. Similar to the spherical version of the problem, a scaling velocity $\dot{X}_o$ and characteristic time τ can be defined

$$\dot{X}_o = \frac{p_v(T_\infty) - p_\infty}{\rho c} \tag{6-9}$$

and

$$\tau = \frac{\pi}{k} \left(\frac{\rho c}{A}\right)^2 \left(\frac{k_\ell}{L\rho_v}\right)^2 \quad . \tag{6-10}$$

In terms of the dimensionless variables

$$\tilde{t} = t/\tau \qquad \text{and} \qquad \chi = \dot{X}/\dot{X}_o \quad ,$$

the approximate equation is

$$\chi(\tilde{t}) = 1 - \int_0^{\tilde{t}} \frac{\chi(\xi)}{\sqrt{\tilde{t} - \xi}} \, d\xi \quad . \tag{6-11}$$

A straightforward application of the Laplace transform technique yields the universal solution:

$$\chi = e^{\pi \tilde{t}} \operatorname{erfc} \sqrt{\pi \tilde{t}} \quad . \tag{6-12}$$

Integration determines the bubble surface position $X(t)$ and equations 6-6 and 6-8 determine the interface temperature from $\dot{X}$. All of the properties of the model solution that were mentioned in the discussion at the end of Section 6.2 can be verified from this solution and its expansions at early times,

$$\chi \sim 1 - 2\tilde{t}^{-1/2}$$

and late times,

$$\chi \sim \frac{1}{\pi} \tilde{t}^{-1/2} \quad .$$

6.3 Limitations of the Approximate Heat Transfer Solution

In this section, the heat transfer problem will be considered from a rather more abstract point of view as the one-dimensional transfer from a plane sink or source (representing the interface) to the fluid flowing into it from the right half plane. Fixing the location of the interface at $x = 0$, the governing equation in interface-fixed coordinates is

$$\left(\frac{\partial}{\partial t} - w(x,t)\,\frac{\partial}{\partial x} - \kappa\,\frac{\partial^2}{\partial x^2}\right) T = 0 \qquad (6\text{-}13)$$

where

$$w(x,t) = \dot{X}(t) - u(x+X(t),t) \ .$$

In the lab frame $\dot{X}$ and u are, respectively, the interface and liquid velocities.

For incompressible one-dimensional flow,

$$u = u(t) \qquad (6\text{-}14)$$

only. If we assume a slightly compressible flow, then u represents an acoustic disturbance and is, in general, a function of position also. To simplify the problem in this case, we suppose that the temperature variation is contained within a thermal boundary layer, within which the velocity u is taken to be uniform and equal to the velocity u_s at the interface, which is a function of time only, $u_s = u_s(t)$. In this case, the general equation is

$$\left(\frac{\partial}{\partial t} - w(t)\,\frac{\partial}{\partial x} - \kappa\,\frac{\partial^2}{\partial x^2}\right) T = 0 \qquad (6\text{-}15)$$

where

$$w(t) = \dot{X}(t) - u_s(t) \ .$$

Boundary conditions are that the temperature is uniform initially, there is no disturbance at infinity and the gradient is specified at

the source;

$$T(x,0) = T_\infty \quad ,$$
$$T(\infty,t) = T_\infty \quad , \qquad (6\text{-}16)$$
$$T_x(0,t) = g(t) \quad .$$

The problem then is to determine the temperature field or, more specifically, the temperature of the interface as a function of the gradient $T_x(0,t)$ at the interface. Solutions can be found for the simplified cases of constant or vanishing velocity w by Laplace transform and Green's function methods.

An order-of-magnitude analysis of the terms in equation 6-15 reveals the general properties of its solutions. The equation has the form of a transport equation with the basic property that the disturbance at the origin will be contained within a boundary layer of thickness $\delta(t)$. The proper form of δ and its dependence on time will be considered next in this section. Outside of this boundary layer diffusion is negligible and material is being transported to the origin without a change in temperature. In the special case treated here of uniform initial conditions (T = constant everywhere), the solution outside the boundary layer is trivial and the equations and boundary layer solution are the same as for the full problem.

The thickness $\delta(t)$ and the interface temperature $T_0(t)$ display either a quasi-steady or nonsteady behavior depending on the relative importance of the convective transport or diffusive (nonsteady) transport. At the interface, the following order-of- magnitudes estimates will be made for the various terms in equation (6-15)

$$\frac{\partial T}{\partial t} \sim \frac{T_0}{t} \quad ;$$

$$w \frac{\partial T}{\partial x} \sim \frac{U T_0}{\delta} \quad ;$$

$$\kappa \frac{\partial^2 T}{\partial x^2} \sim \frac{\kappa T_0}{\delta^2} \quad , \tag{6-17}$$

where U is a constant velocity characterizing $w(t)$. Inside the boundary layer the diffusion term $\frac{\partial^2 T}{\partial x^2}$ is always important and must be balanced by one or both of the other terms to obtain non-trivial solutions.

In the case where nonsteadiness dominates, the previous remarks imply that

$$\frac{1}{t} \sim \frac{\kappa}{\delta^2} >> \frac{U}{\delta} \quad . \tag{6-18}$$

The result $\delta \sim \sqrt{\kappa t}$ is typical of a diffusion-controlled process and as long as $w \sim t^{-n}$ where $n \geq \frac{1}{2}$, there will always exist a stage near $t = 0$ where this process dominates. The approximate equation governing this stage is

$$\frac{\partial T}{\partial t} - \kappa \frac{\partial^2 T}{\partial x} = 0 \quad . \tag{6-19}$$

It has the solution

$$T(x,t) = T_\infty - \left(\frac{\kappa}{\pi}\right)^{1/2} \int_0^t \frac{T_x(0,t)}{\sqrt{t-\tau}} \, e^{-\frac{x^2}{4\kappa(t-\tau)}} \, d\tau \quad . \tag{6-20}$$

Note that for $x = 0$, this is simply equation 6-3 which appeared in our one-dimensional analog of the classical model of bubble growth.

In the case where convection dominates, the relations between the scaling parameters must be

$$\frac{U}{\delta} \sim \frac{\kappa}{\delta^2} >> \frac{1}{t} \quad . \tag{6-21}$$

The thickness is now $\delta \sim \frac{\kappa}{U}$ and depends on time only if $w(t)$ is a strong function of time. This is a result typical of steady-state heat transfer such as in forced convection or a steady flame front. If the boundary condition $T_x(0,t)$ and velocity $w(t)$ are sufficiently well behaved functions of time, there will always be a stage where inequality (6-21) is satisfied for sufficiently large time t. The approximate equation governing the asymptotic stage is

$$- w \frac{\partial T}{\partial x} - \kappa \frac{\partial^2 T}{\partial x^2} = 0 \qquad (6\text{-}22)$$

which has the solution

$$T(0,t) = - \frac{\kappa T_x(0,t)}{w(t)} e^{- \frac{w(t)}{\kappa} x} . \qquad (6\text{-}23)$$

For the case in which the velocity $w(t)$ is constant and $T_x(0,t)$ is reasonably well behaved, there must be a crossover between the diffusive behavior at the early times and the asymptotic quasi-steady state. The time t^* at which this occurs is, say, when the thicknesses $\delta(t)$ for both cases are equal

$$\frac{\kappa}{U} = \sqrt{\kappa t^*}$$

or, $t^* = \kappa/U^2$. The analytical solution for the case $w(t) = w =$ constant substantiates these order-of-magnitude estimates, and expansion of that solution at early and late time yields solutions 6-20 and 6-23 respectively. The existence of the characteristic time t^* has previously not been pointed out in the context of heat transfer for the bubble growth problem.

At the low superheats typical of all previous bubble-growth experiments, the velocities $w(t)$ induced by the mass flux through the liquid-vapor interface were very small, thus the times t^* are

enormous compared to the duration of the experiment. For example, for water at 3.5° C superheat, $t^* = 10^6$ sec! Therefore, the commonly used diffusive approximation for the heat transfer (e.g. Plesset and Zwick 1952) with $w = 0$ agrees quite well with the low superheat experimental data. However, the time t^* in the present experiments with butane at the superheat limit is estimated to be on the order of 10^{-9} sec! This time is much smaller than the time $\tau = 2 \times 10^{-5}$ sec characterizing the length of the inertial stage, indicating that convective transport must play an important role in bubble growth. The neglect of this effect in the theory could account for some of the discrepancy with experimental observations. However, the presence of the highly roughened evaporative surface indicates that there are other, equally serious, problems with the model. In conclusion, the results of this section indicate the need for a more careful treatment of bubble growth at large superheats. Particularly, the role of convective heat transport should be reconsidered and the possibility of "steady-state" solutions investigated.

REFERENCES

Carslaw, H. and Jaeger, J. 1959 Conduction of Heat in Solids 2nd ed., Clarendon Press, Oxford.

Plesset, M. and Zwick, S. 1952 "A Nonsteady Heat Diffusion Problem with Spherical Symmetry", J. App. Phys. 23, 95.

Prosperetti, A. and Plesset, M. 1978 "Vapor-Bubble Growth in a Superheated Liquid", J. Fluid Mech. 85, 349.

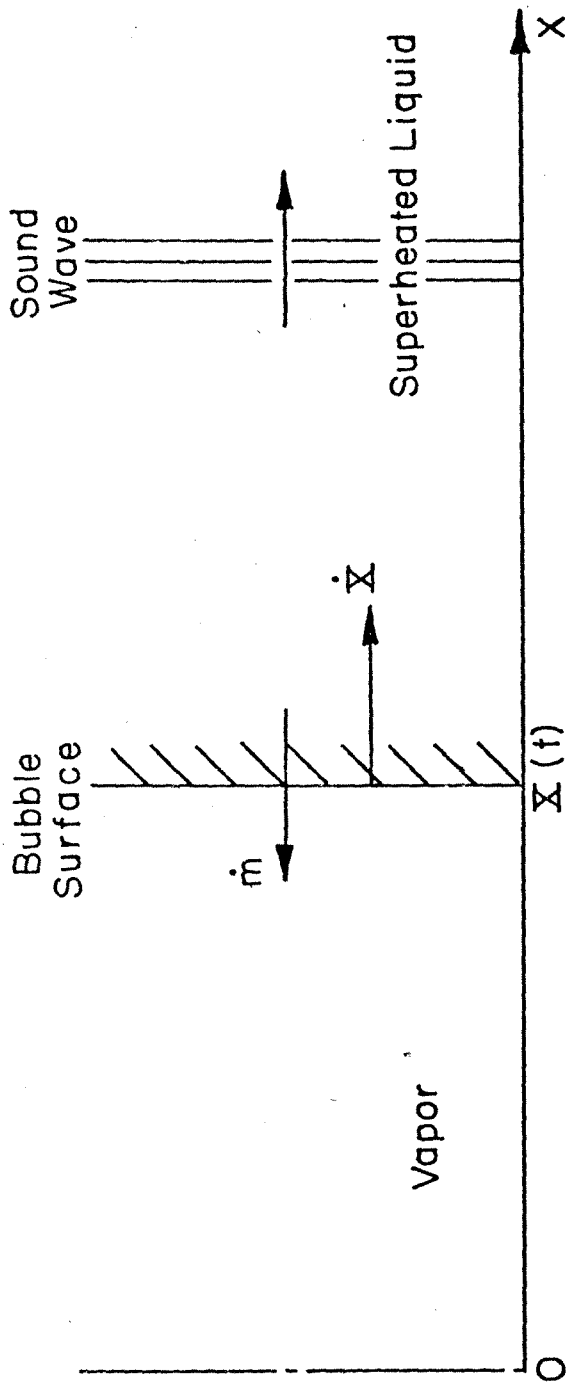

FIG. 6.1 ONE-DIMENSIONAL ANALOG OF CLASSICAL BUBBLE GROWTH

VII. CONCLUSIONS

The vapor explosion of a single droplet (~ 1 mm dia.) of liquid butane at the superheat limit has been experimentally investigated. The purpose of this experiment was exploratory, and was motivated by the difficult and unknown dynamics of highly nonequilibrium evaporation which occurs at the limit of thermodynamic stability. High speed photography and pressure measurements have been used together for the first time to obtain a description of the complete explosion process within a drop superheated in the bubble-column apparatus. Emphasis was placed on the early (microsecond time scale) evaporative stage. Despite the apparent simplicity of the vapor explosion of a single superheated droplet, the present experiment revealed a wide range of phenomena of varying complexity occurring at different stages of the explosion.

The explosion is initiated by a single nucleus spontaneously forming in the drop, close to, but not on the drop surface. The nucleus grows by evaporation of the surrounding superheated butane to form a butane vapor bubble asymmetrically located within the drop. Bubble growth involves several new and unique features which are remarkably repeatable for different explosions:

a) Photographs of the evaporative surface show a highly roughened and disturbed interface for most of the evaporative stage. At the earliest times in the explosion for which photographs have been obtained (~ 8 μsec), the roughening appears to begin as a regular pattern on an otherwise spherical surface, suggestive of a fundamental instability due to evaporative mass flux.

b) Due to the asymmetric location of nucleation within the

drop, a portion of the evaporating bubble surface is observed to contact the host fluid first and become nonevaporating. A unique, axisymmetric structure of circumferential surface waves culminating in a spherical cap appears on this protruding nonevaporating surface as the bubble grows. Both the surface waves and the protrusion of the nonevaporating surface are conjectured to be driven by the "jet" of evaporated vapor coming from the opposing evaporating surface and impinging on the host liquid.

c) Nucleation and initial development of the bubble in the first 10 μsec is almost universally accompanied by an intriguing pulsating pressure signal, characterized by two steps, which suggests that a fundamental and repeatable unsteadiness, perhaps connected with the above-mentioned instability, is taking place at this stage. Unfortunately, no volume data were obtained in the present experiment prior to 8 μsec so that a definite source for this signal could not be determined.

Overall, bubble growth is characterized by a constant effective radial velocity of $\sim$ 14.3 m/sec, resulting in the complete vaporization of the original drop liquid within 40-160 μsec (depending on the initial drop size) of the beginning of the explosion. Pressure signals measured $\sim$ 2.5 cm from the explosion during the evaporative stage (but after the occurrence of the two-step structure which is always observed) show a roughly linear increase of pressure with time, upon which nonrepeatable oscillations may be superposed. The maximum pressure reached at the end of evaporation ranges from 1 to 7 psi, larger drops producing larger maximum pressures.

Immediately following the completion of evaporation, the bubble is at a net positive overpressure, due to the dynamic, nonequilibrium nature of the foregoing evaporation process. This stored energy is released through subsequent volume oscillations of the gas bubble.

These oscillations produce characteristic pressure waves known as "bubble pulses", which are the dominating feature of all pressure signals measured in the later stages of the explosion. At the minimum in volume of the first oscillation cycle, the surface of the bubble experiences large adverse accelerations, resulting in Taylor instability, and catastrophic deformation of the bubble surface results. Continuing volume oscillation of the deformed bubble is accompanied by further Taylor instability and increasing deformations until the original bubble is broken up into a large number of smaller bubbles; in all cases, this is the final state visible to the human observer.

All of these features of bubble dynamics observed at later times have been previously reported by many investigators in other contexts; the merit of the present observations is the clarity of the photographs of the instability process and the ideal nature of droplet vapor explosions for producing large amplitude oscillations of an inert gas bubble.

By far the most important discovery of the present work is the instability of the evaporative surface and its implication for greatly increased evaporative mass transfer. A simple acoustic model of the evaporating bubble was developed to relate evaporative mass flux to the volume growth rate and emitted pressure signal. Using photographically determined bubble volumes and pressure signals measured in the first 30 μsec of the explosion, a preliminary estimate of the evaporative mass flux has been made with this model. After a very rapid increase in the first 1-2 μsec of bubble growth, the mass flux remains approximately constant at $\sim$ 400 gm/cm^2 sec thereafter. This mass flux is much larger than encountered in typical evaporation

experiments and is 10^2 larger than would be predicted on the basis of classical, diffusion-limited bubble growth. Further, comparison with measured volume growth rates and emitted pressure signals shows that the classical theory vastly underestimates both quantities at later times. It is not possible to determine from this preliminary investigation whether the abnormally large mass flux is solely produced by the increase of evaporative surface area due to the roughening or whether more subtle effects associated with the highly nonequilibrium state of the liquid are also involved. In any case, the present results clearly indicate that the assumptions of the previous, near-equilibrium theories of evaporation need reconsideration at the extreme conditions of the superheat limit.

It is proposed in the present work that the roughening of the evaporative surface originates in a fundamental instability of the liquid-vapor interface driven by the evaporative mass flux. We have investigated this for the simplest type of instability mechanism, the Landau or inertial instability, which depends only on the existence of a sufficiently large mass flux and a density difference at the interface. Landau's original analysis for a plane surface was supplemented by an ad hoc correction for sphericity, and the resulting theory was applied to the classical model of bubble growth. Taking into account surface tension and deceleration, the bubble surface was found to be unstable for the portion 8×10^{-9} to 3×10^{-7} sec of the initial growth.

The earliest observations in the present study at 8 μsec show a regular pattern with a scale length of 20-40 μm on the surface of the bubble; a maximum length scale of 2-10 times smaller than that is predicted by by the ad hoc theory to occur at times of order 0.3 μsec. An explanation consistent with the available evidence and the theory is that the

observed instability at 8 μsec has developed well into the nonlinear stage and the actual instability did occur in the first 1-2 μsec of bubble growth. Bubble images enhanced by digital processing show substantial asymmetry and randomness in the pattern observed at the earliest times, supporting the above conclusion.

A one-dimensional analogue of the classical model of bubble growth has been developed and, under certain assumptions, analytically solved. In the context of this one-dimensional model, we have reexamined the assumption used in the classical theory that convective heat transfer is neglibible. It is concluded that under the conditions found at the superheat limit, this assumption is incorrect. Entirely different types of solutions may be possible; in particular, steady-state solutions can exist.

In conclusion, the present observations are fundamentally different from what would be expected by the mere extrapolation of previous near-equilibrium theories and results. Preliminary efforts have been made to calculate the evaporative flux and stability properties of rapidly evaporating surfaces, but only a superficial treatment has been possible. The extent of the generality of the present experimental results needs to be verified in detail, but clearly, the present observations indicate evaporation at the superheat limit can be much more complex than previously envisioned.

APPENDIX A, PRELIMINARY MEASUREMENTS

A.1 Shadowgraphy

Initial visualization of the explosions was made with a simple shadowgraph system (Figure A.1) which consisted of a point source spark gap, a collimating mirror and a Polaroid film holder. The spark gap was triggered from the pressure signal by the same technique as described in Section 2.4.2 and the images were recorded on Polaroid type 667 film (ASA 3ØØØ). Due to focusing effects mentioned in Section 2.4.2, the drops and bubbles appeared as relatively featureless opaque blobs; only the relatively large surface perturbations (Taylor instability) at late times were obvious.

From these shadowgraphs and the pressure signals the existence of bubble oscillations and the possibility of instability at late times were inferred. The evaporation process remained unrevealed and clearly better diagnostics were called for.

A.2 Extinction Meter

Shadowgraph observations of the nearly circular shadows cast by the exploding droplets suggested that a continuous measurement of the extinction of incident light could yield the mean diameter as a function of time. A system was assembled to do this as shown in Figure A.2. The principle of operation is that the optical cross-section of such a scatterer as the exploding droplet is proportional to the geometric cross-section. Asymptotically in the far field of the scattered radiation, the constant of proportionality is 2; directly reflected and refracted rays account for half this, the other half is contributed by the light diffracted from the edge of the drop, see Brillouin (1949). Generally, the far field approximation is not

achieved experimentally (Sinclair 1947) and a calibration scale has to be established for individual instruments.

The illumination for the instrument shown in Figure A.2 was provided by a 5 mW He-Ne laser whose output was spatially filtered and collimated. The collimated beam passed through a beam splitter where a portion of it was focused onto a phototransistor (reference detector); the remainder of the beam proceeded through the test section intercepting the exploding droplet. After exiting the test section the beam passed through an aperture and was focused onto a second phototransistor (signal detector). The outputs from the reference and signal detectors were recorded by the Nicolet oscilloscope for later processing by the computer. Given the initial drop diameter and the instrument calibration, the projected area as a function of time could be determined from the ratio (used to eliminate any overall drift in intensity) of signal detector output to reference detector output. An example of the signal detector output is shown in Figure A.3, the bubble oscillations and mean volume increase can be seen quite clearly.

These measurements confirmed the existence of oscillating bubbles, at late times, and indicated that an overall expansion of the drop occurred during the evaporation stage. However, there was no chance of revealing the details of the evaporation process by this method and it was not further pursued.

REFERENCES

Brillouin, L. 1949 "The Scattering Cross Section of Spheres for Electromagnetic Waves", J. App. Phys. 20, 1110.

Sinclair, D. 1947 "Light Scattering by Spherical Particles", J. Opt. Soc. Am. 37, 475.

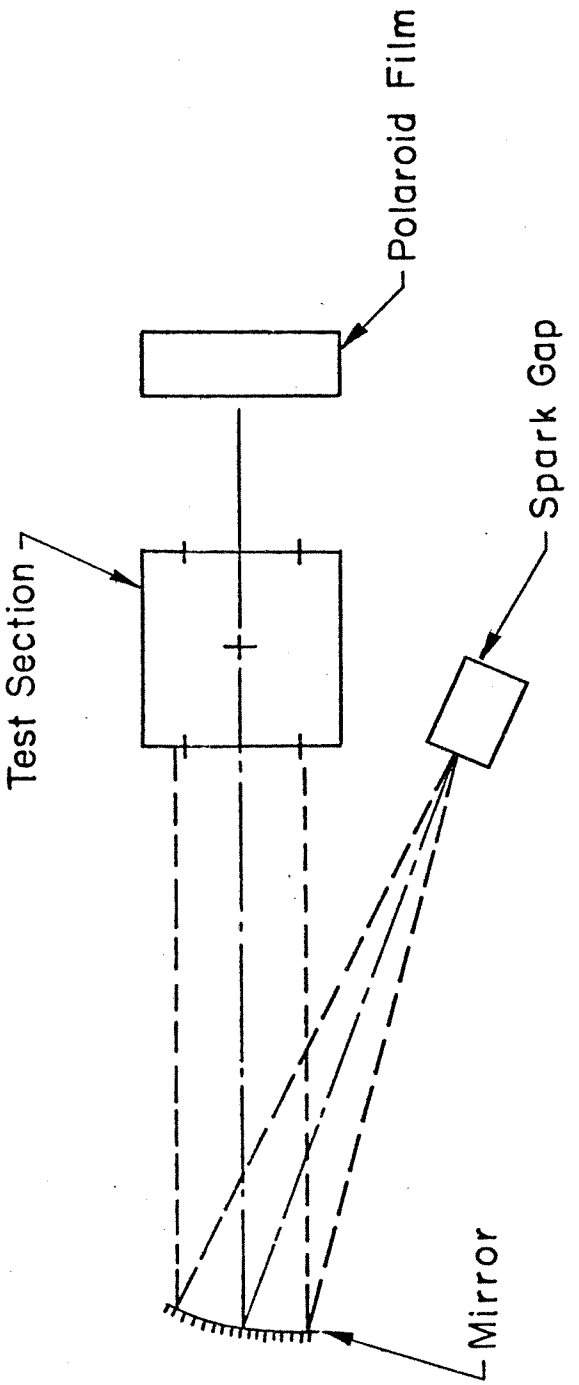

FIG. A1 APPARATUS FOR SPARK SHADOWGRAPH PHOTOGRAPHY

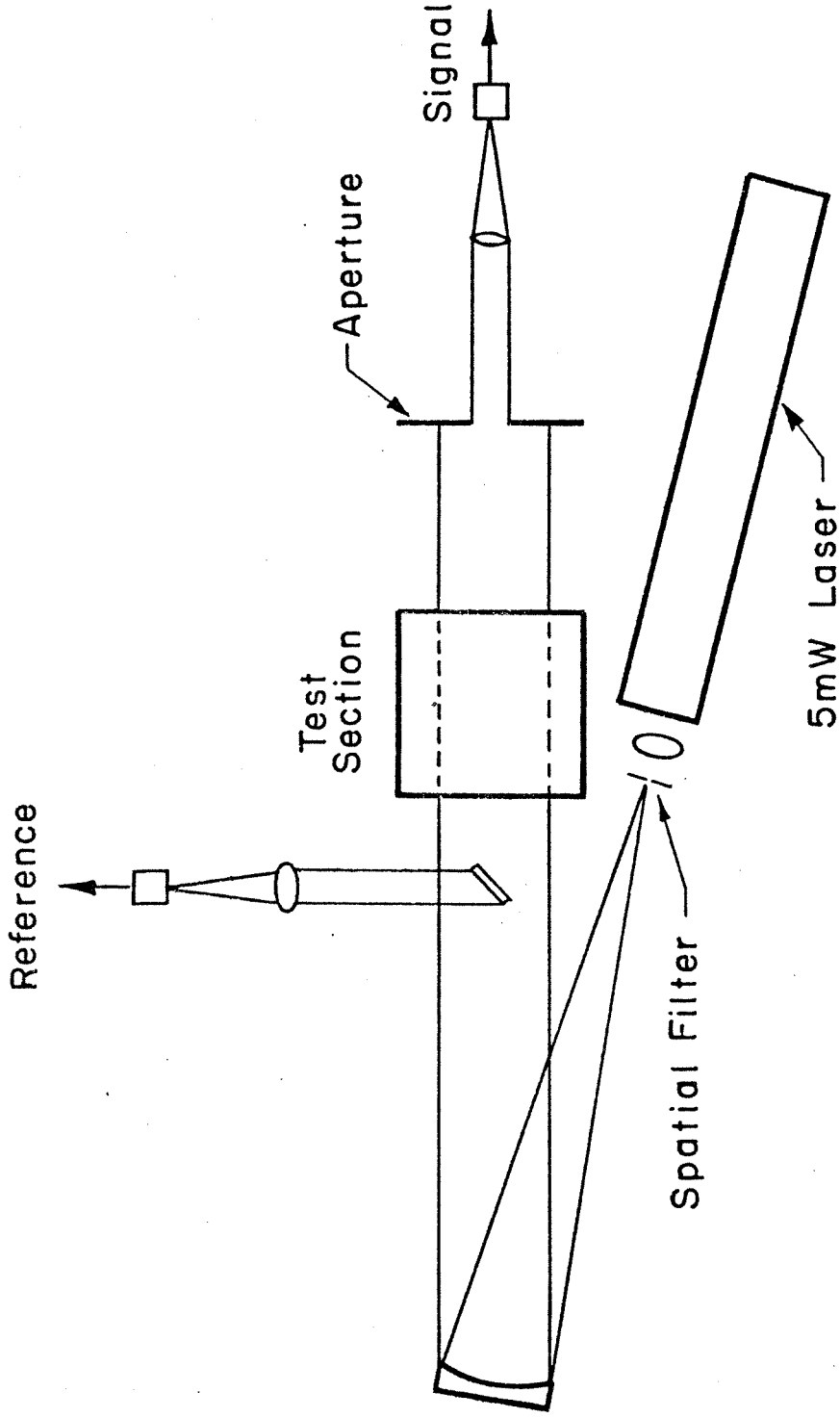

FIG. A.2 OPTICAL EXTINCTION MEASUREMENT

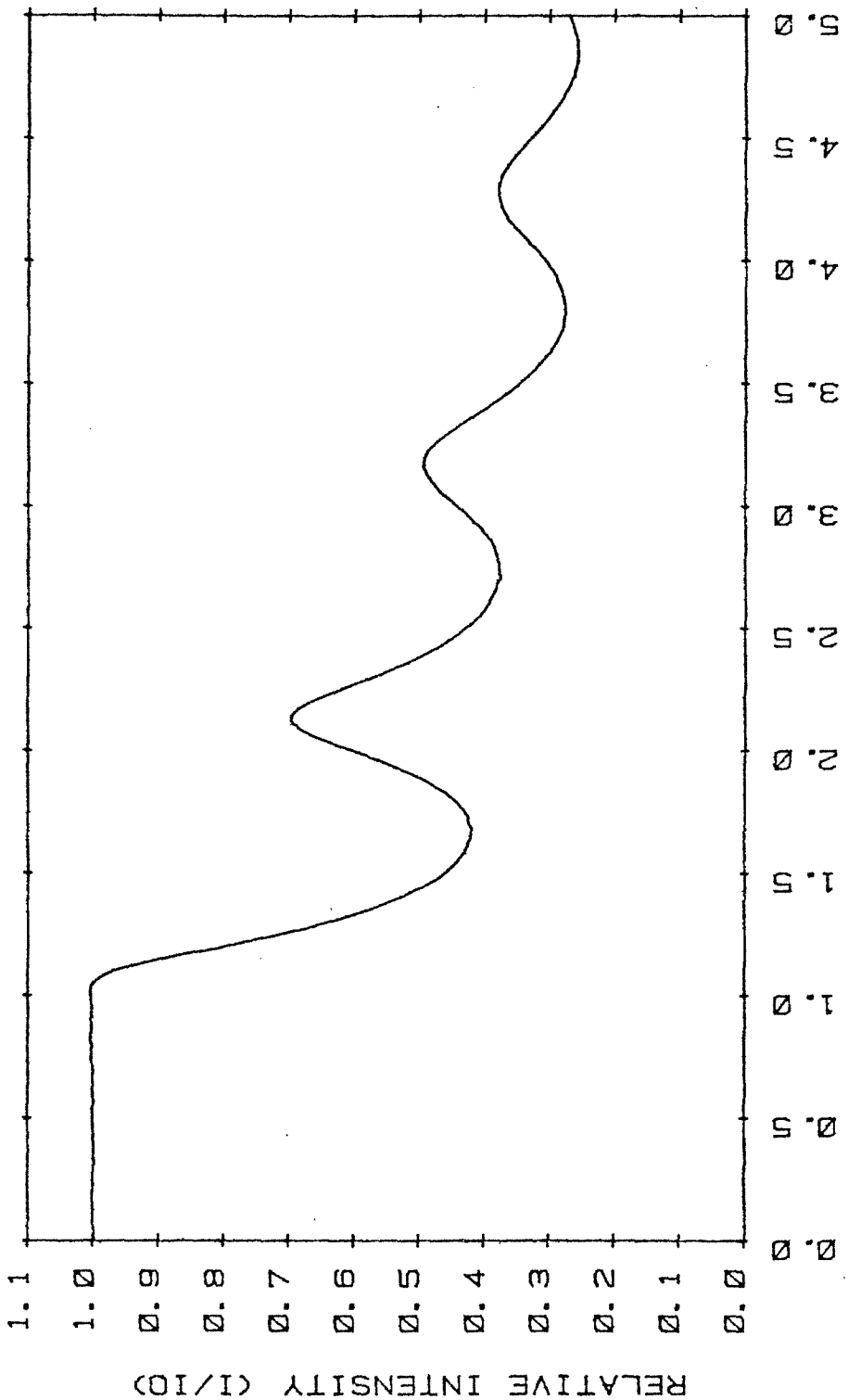

FIG. A.3 EXAMPLE OF RAW DATA FROM EXTINCTION METER MEASUREMENT

APPENDIX B, START UP OF AN AIR JET INTO WATER

This appendix describes some exploratory flow visualization of the start up of an air jet submerged in water. The purpose of this experiment was to determine if there was any similarity of the air-water interface to the butane vapor-glycol interface described in Section 3.3.2. The primary interest was in the form of the instabilities that must certainly be present on the jet surface. No effort was made to achieve true dynamic similarity between the two flows.

The apparatus (Figure B.1) consisted of an aquarium filled with water, an air injection system (jet air supply) and a photographic set up similar to that described in Section 2.4.2. The jet issued downward from a flanged 1/8" pipe placed just beneath the free surface of the water, about 8" from the bottom of the aquarium. A solenoid valve connected the jet pipe with the air reservoir, a surplus oxygen bottle ($\sim$ 340 cm^3 volume) pressurized with house air (30 psig). The triggered spark gap-diffuser described in Section 2.4.2 was used to illuminate the jet at a variable delay time from the solenoid opening. The image was recorded at a magnification of 2 on Polaroid type 47 film, using the same Graphex camera body as in the principal investigation. By carefully maintaining constant initial conditions for every shot (i.e. the same reservoir pressure and the same size initial air bubble protruding from the jet orifice), single photographs taken at different delay times on separate shots could be used to construct the course of jet development.

Several different combinations of jet orientation (upwards or downwards) and orifice configurations (flanged and unflanged) were experimented with. All of these combinations showed the development

of instabilities on the jet surface; the most striking of these were obtained with the particular arrangement of Figure B. 1. The development of the jet is shown in Figure B. 2; the times indicated under each print are the number of milliseconds that have elapsed since the current was first applied to the solenoid. Prior to 4 msec, there was no detectable motion; this corresponds to the opening time of the solenoid.

The jet is initially just a growing half bubble of air, originating from the small half bubble naturally present on the orifice when there is no flow. Mean half bubble shape develops from an initially oblate to a prolate axisymmetric surface; bubble volume increases approximately linearly in time (flow through the solenoid valve orifice is choked). The surface appears very smooth until $\sim$ 10 msec, when an annular bulge can be seen developing near the base of the bubble. Further development of surface deformations can be seen in the subsequent prints at 11, 19 and 26 msec. These surface deformations are very strikingly axisymmetric and exhibit the sharp corners (particularly the 26 msec print) and regularity seen in the vapor explosions. In the 19 msec print, the surface is observed to have a re-entrant shape following the bulge nearest to the flange.

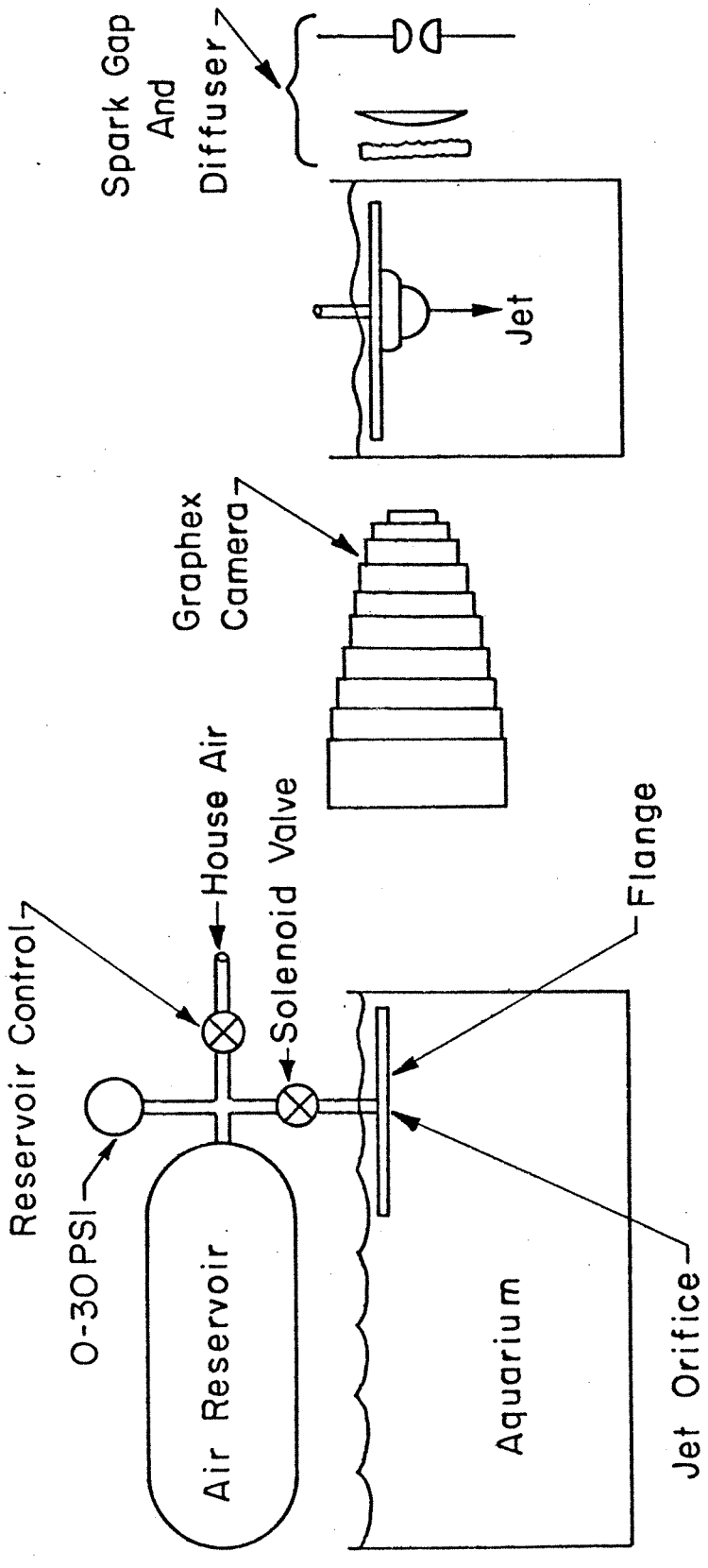

(a) Mechanical (b) Photography

FIG. B.1 SETUP FOR AIR → WATER JET VISUALIZATION

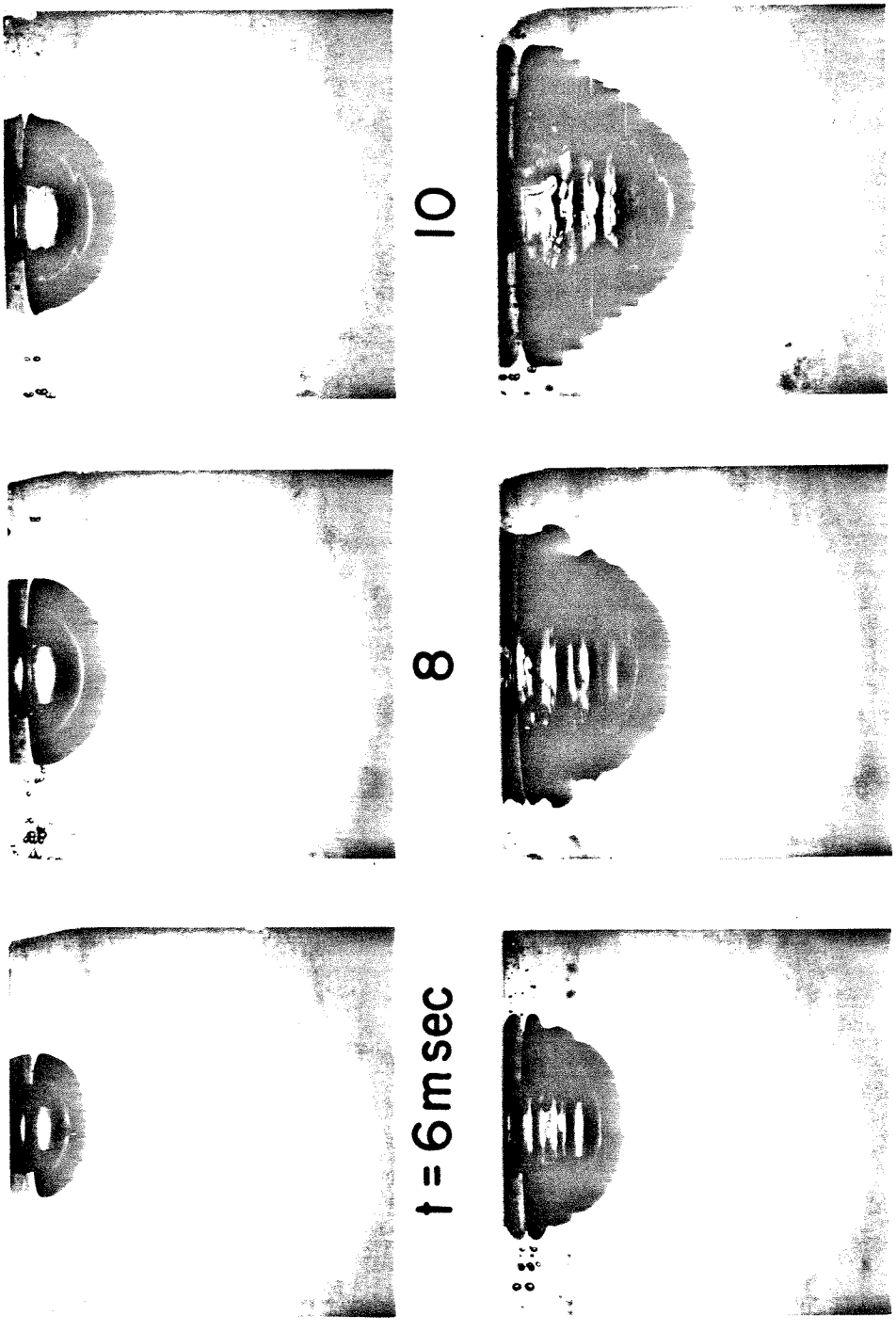

FIG. B.2 START UP OF AIR JET INTO WATER (|—|, 1cm.)

APPENDIX C, STABILITY CRITERIA FOR OSCILLATING BUBBLES

Linear stability of the surface of an oscillating bubble was first considered in connection with the observed instability of collapsing cavitation bubbles (Plesset 1954) and bubbles resulting from underwater explosions (Cole 1948). General criteria for stability were established by Birkhoff (1956), who found that, in addition to the usual Taylor instability associated with acceleration, there could exist an algebraically growing instability associated with a decrease in radius. Although the stability for freely oscillating bubbles was investigated numerically by Strube (1971), the role of accelerations was not emphasized and the simple results which can be obtained from Birkhoff's criteria were not stated. The purpose of this appendix is to explain some general features of the instability and to give the results of Birkhoff's criteria for stability of the freely oscillating bubbles observed in the present experiments.

A standard linear stability analysis assuming inviscid, incompressible flow (for example see Plesset and Prosperetti (1977)) yields the Rayleigh equation

$$R\ddot{R} + \frac{3}{2}\dot{R}^2 = \frac{p(R) - p_\infty}{\rho_\infty} - \frac{2\sigma}{\rho_\infty R} \qquad (C\text{-}1)$$

for the mean bubble radius R and a linear, second order equation for the surface perturbation amplitude a_n

$$\ddot{a}_n + 3\frac{\dot{R}}{R}\dot{a}_n - A\,a_n = 0 \qquad (C\text{-}2)$$

where

$$A = (n-1)\left(\frac{\ddot{R}}{R} - \frac{(n+1)(n+2)\sigma}{\rho_\infty R^3}\right) \qquad (C\text{-}3)$$

and the vapor density has been neglected in comparison to the liquid

density in the last expression. The angular variation of the surface perturbation is assumed to be given by a spherical harmonic of order n, $Y_n^m(\theta,\varphi)$; note that the azimuthal index m does not appear in equation C-2.

Birkhoff's stability criterion for equation C-3 is:

a) $A < 0$, $\frac{d}{dt}(R^6 A) > 0$; oscillatory instability, surface wave amplitudes oscillate in sign and grow in time.

b) $A > 0$, $\frac{d}{dt}(R^6 A) \lesseqgtr 0$; unstable, surface wave amplitudes grow monotonically in time.

c) $A < 0$, $\frac{d}{dt}(R^6 A) < 0$; absolutely stable, surface wave amplitudes decrease monotonically in time.

Generally, instability b) grows much faster than a), exponentially vs. algebraically, so b) tends to be more important and will be discussed first. From equation C-3, $A > 0$ whenever $\ddot{R} > 0$ and sufficiently large; thus instability b) can be expected whenever the surface accelerations are large and positive. This is simply the spherical analog of the Taylor instability (Taylor 1950) for an accelerated plane interface. Both the plane and spherical cases share the common feature that if the wavelength λ of the disturbance is small enough (i.e. mode number n large enough) $\lambda < \lambda_c$, then surface tension will damp out any possible instability. For large mode number n, the spherical interface appears locally plane to the disturbance and an effective wavelength λ can be defined,

$$n\lambda = 2\pi R \quad . \tag{C-4}$$

The effective cutoff wavelength λ_c can then be determined by setting $A = 0$, approximating $(n+1)(n+2) \doteq n^2$ and using equation C-4,

$$\lambda_c = 2\pi \sqrt{\frac{\sigma}{\ddot{R}\rho_\infty}} \quad . \tag{C-5}$$

This expression has exactly the same form as the corresponding result for a plane interface. Another common feature is that there is a most unstable mode in both spherical and planar cases. The form of equation C-3 and its dependence on n assures that A will have a maximum for n between $n = 2$ (the lowest order mode which actually represents a surface deformation) and the cutoff mode number, $n_c = 2\pi R/\lambda_c$.

The major difference between the spherical and planar Taylor instabilities is that the longest wavelength possible in the spherical case is finite (corresponding to $n = 2$), while in the planar case modes of infinitely large wavelength can occur. This difference can be interpreted as the existence in the spherical case of another cut-off wavelength λ_R, approximately equal to the bubble radius, which has the effect of damping out all modes with $\lambda > \lambda_R$. An important consequence is that the spherical interface can be absolutely stable if $\lambda_c > \lambda_R$, irrespective of the magnitude of the accelerations. Physically, this case occurs whenever the bubble radius is so small that surface tension forces associated with the mean curvature of the interface damp out any possible disturbances. The criterion for the absolute stability under the conditions where $\ddot{R} > 0$ can be found by requiring A to be negative for the lowest mode (insuring that it will be negative for all modes), $n = 2$. This implies that

$$(\ddot{R})_{max} < \frac{12\sigma}{\rho_\infty R^2} \quad . \tag{C-6}$$

Instability a) is specific to spherical surfaces and occurs under conditions ($A \leq 0$) considered stabilizing or at worst, neutrally stable for a plane interface. General circumstances under which this instability occurs are difficult to specify, but there are some simple particular cases. One standard example is the collapse of a spherical void suddenly created in a fluid; this is Rayleigh's original cavitation bubble collapse problem, discussed in Plesset and Prosperetti (1977). In that case, the accelerations are stabilizing but the decreasing "bubble" radius causes any initial surface disturbances to grow, the amplitude being proportional to $R^{-1/4}$ and oscillating in sign as the "bubble" collapses. Another simple case is the freely oscillating bubble, which will be discussed next.

An idealized model for the oscillating gas bubbles observed in the present study is the Rayleigh equation with the gas pressure given by the adiabatic relation

$$p(R) \sim R^{-3\gamma} \quad . \tag{C-7}$$

With appropriate boundary conditions, this equation yields periodic, nonlinear oscillations of R (schematically indicated in Figure C. 1) which have been used extensively to represent the motion of freely oscillating bubbles, e. g. Cole (1948). Using the stability criterion given above the unstable portions of an oscillation cycle can be determined as a function of the amplitude and frequency of the oscillation.

As expected, the motion is stable for all frequencies of oscillation if the amplitude is small enough. With increasing amplitude, the first possibility of instability is parametric excitation for particular volume oscillation frequencies corresponding to subharmonics

of the linear surface wave oscillation frequencies. This mechanism causes surface deformations to grow slowly over many volume oscillation periods (Hullin 1971; Francescutto and Nabergoj 1978), and is obviously irrelevant to the catastrophic instability observed in the present experiments.

The catastrophic type of instability seen in the present work is associated primarily with the large, positive radial accelerations that occur at the minimum in volume during the oscillation cycle. For large oscillation amplitudes, the surface tension can be neglected in the Rayleigh equation and the accelerations $(\ddot{R})_{max}$ at the volume minimum can be written

$$(\ddot{R})_{max} = \frac{\Delta p(R_{min})}{\rho_\infty R_{min}} \quad . \tag{C-8}$$

Using the above expression for $(\ddot{R})_{max}$ in inequality (C-6), we find that it is possible that $A > 0$ (for $n = 2$) only if

$$\Delta p(R_{min}) > \frac{12\sigma}{R_{min}} \quad . \tag{C-9}$$

Whether inequality (C-9) is satisfied depends on the amplitude of oscillation; the larger the amplitude, the better it is satisfied. Therefore, if the amplitude of the oscillation is sufficiently large, then $A > 0$ for some mode numbers n when the bubble radius is a minimum. Taylor instability then, is only possible in that portion of the oscillation cycle near the minimum radius (labeled (b) in Figure 6.1); whether the instability will actually occur depends on both the amplitude of the oscillation i.e. $(\ddot{R})_{max}$ and the magnitude of the surface tension.

Away from the region near the minimum radius, $\ddot{R} < 0$ and therefore $A < 0$ always. Then, the only type of behavior possible is case (a) or (c). Using the Rayleigh equation, the deriviative $\frac{d}{dt}(R^6 A)$ can be calculated and we find that if $\dot{R} > 0$ case (c) holds, absolute stability; if $\dot{R} < 0$ case (a) holds, with the possibility of algebraic instability. The regions of the oscillation cycle where these two cases occur is shown on Figure 6.1. In summary:

a) $\dot{R} < 0$, $\ddot{R} < 0$; unstable, surface waves grow algebraically in time;

b) $\dot{R} \lesseqgtr 0$, $\ddot{R} > 0$; unstable, surface waves grow exponentially in time;

c) $\dot{R} > 0$, $\ddot{R} < 0$; absolute stability, surface waves are damped (exponentially) in time.

The three regimes where the different instabilities, (a) - (c), are possible are indicated on a typical cycle of oscillation in Figure C.1 (the corresponding pressure pulse Δp that would be produced in the far field of this oscillation is also shown). Away from a region near the minimum radius, growth of the bubble damps the surface waves until the maximum radius occurs. As the bubble collapses from the maximum radius, surface waves can first grow algebraically in amplitude, then exponentially if $\ddot{R}$ becomes sufficiently positive near the minimum radius.

Experimentally, onset of instability and the importance of non-linear effects, at the first minimum in bubble volume, is shown in Figure C.2. The pressure trace in this figure was obtained in the far field (configuration C of Figure 2.3) so that a comparison to

Figure C.1 is possible. From print (c), the characteristic wavelength of the deformations can be estimated to be 0.3 mm. Using equation C-8, the radial acceleration can be estimated from the peak amplitude of the bubble pulse and the minimum bubble radius (2 mm) to be 10^4 g. The most amplified wavelength, $\lambda^* = \lambda_c/\sqrt{3}$ predicted by the plane Taylor instability theory from this acceleration (i.e. equation C-5) is within a factor of 2 of the observed characteristic wavelength. The even more complex process which occurs at the second minimum is illustrated in Figure C.3.

REFERENCES

Birkhoff, G. 1956 "Stability of Spherical Bubbles", Q. Appl. Math. 13, 451.

Cole, R.H. 1948 Underwater Explosions, Princeton University Press, Princeton, New Jersey.

Francescutto, A. and Nabergoj, R. 1978 "Pulsation Amplitude Threshold for Surface Waves on Oscillating Bubbles", Acustica 41, 215.

Hullin, C. 1977 "Stabilitäts grenze pulsierender Luftblasen in Wasser", Acustica 37, 64.

Plesset, M.S. 1954 "On the Stability of Fluid Flow with Spherical Symmetry", J. App. Phys. 25, 96.

Plesset, M.S. and Prosperetti, A. 1977 "Bubble Dynamics and Cavitation", in Ann. Rev. Fluid Mech. 9, 145.

Strube, H.W. 1971 "Numerische Untersuchungen zur Stabilität nichtsphärisch schwingender Blasen", Acustica 25, 289.

Taylor, G.I. 1950 "The Instability of Liquid Surfaces when Accelerated in a Direction Perpendicular to Their Planes. I", Proc. Roy. Soc. A201, 192.

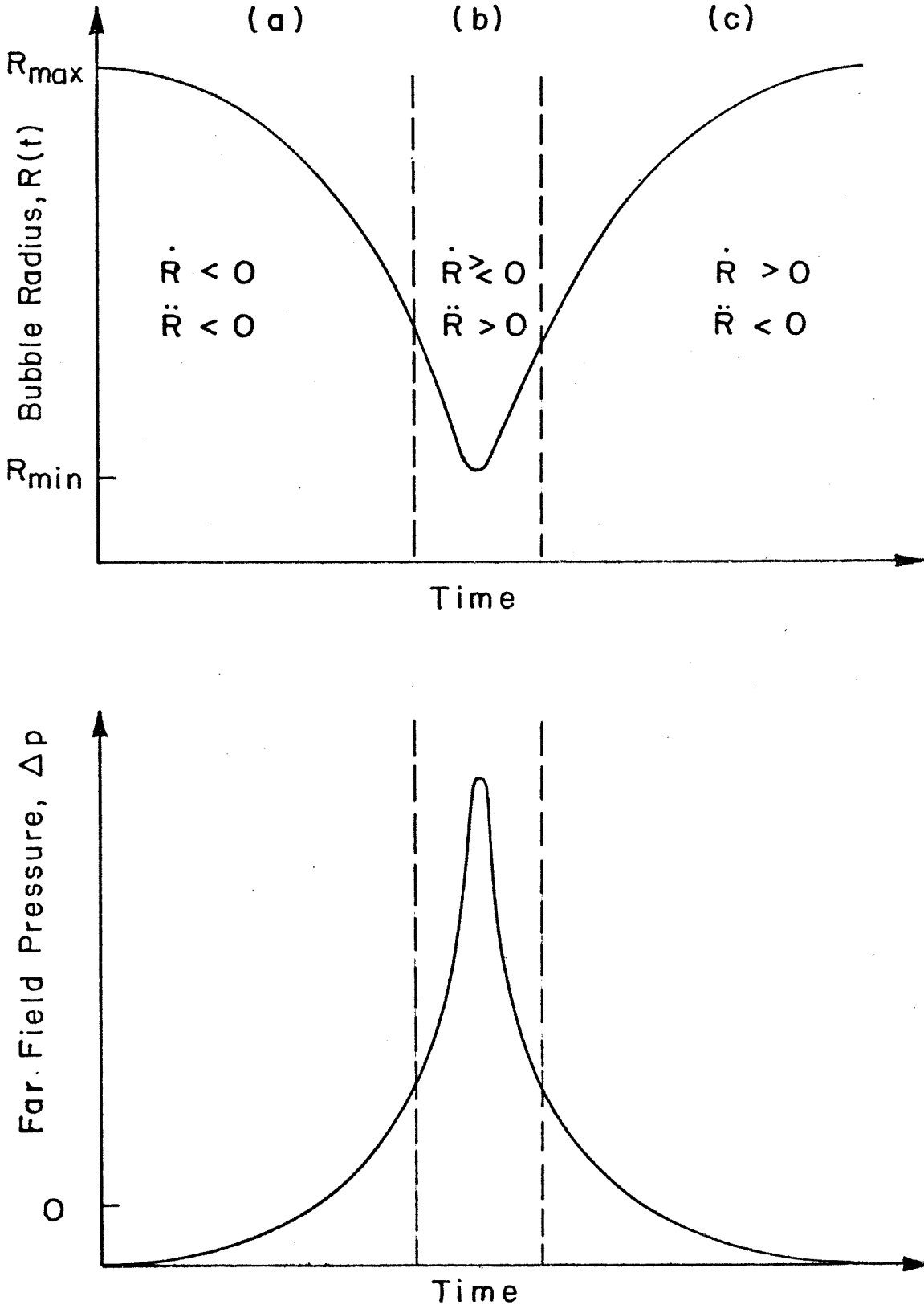

FIG. C.1 A NONLINEAR BUBBLE OSCILLATION CYCLE SHOWING STABILITY REGIMES AND THE FAR FIELD BUBBLE PULSE

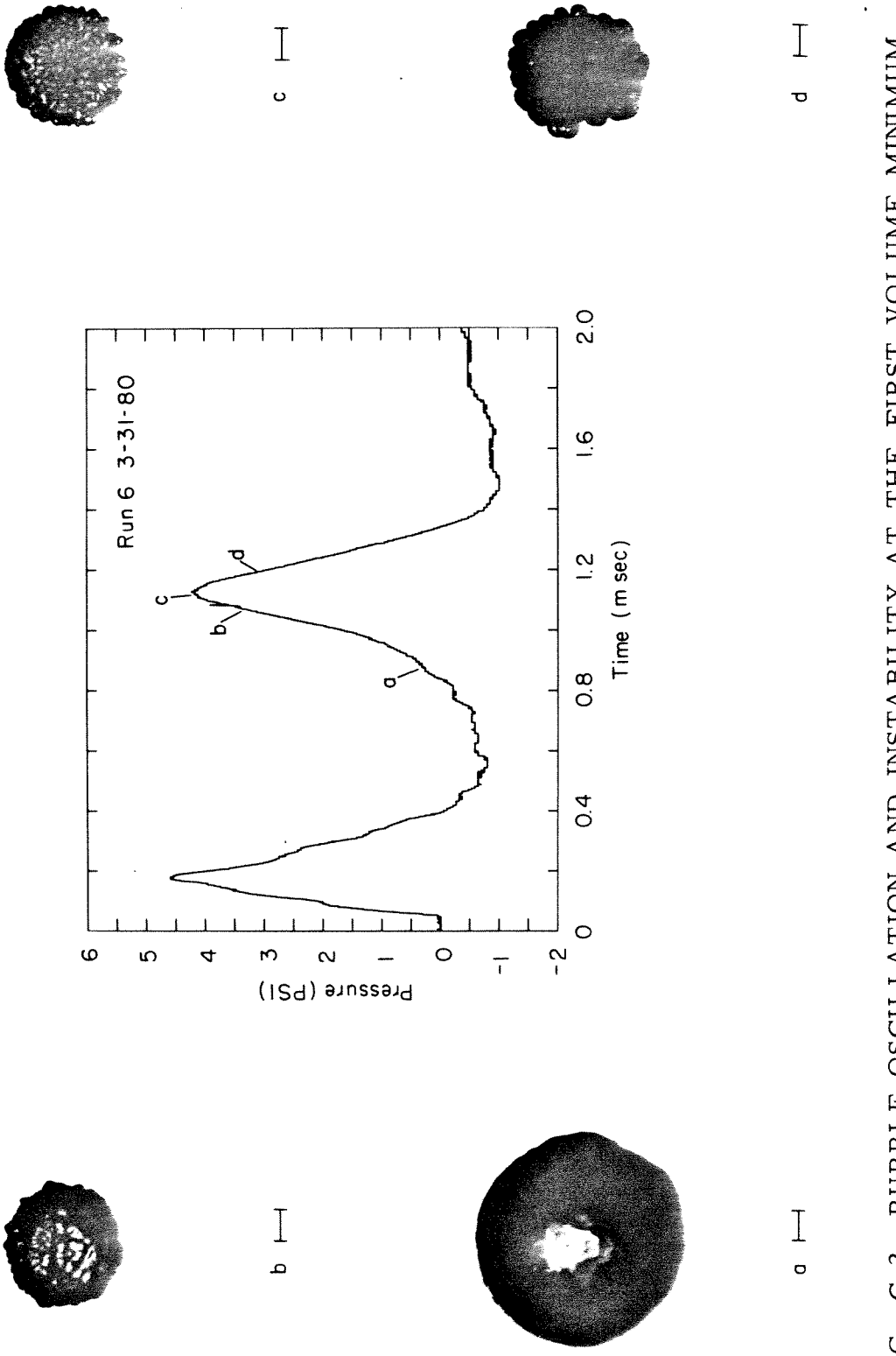

FIG. C.2 BUBBLE OSCILLATION AND INSTABILITY AT THE FIRST VOLUME MINIMUM.

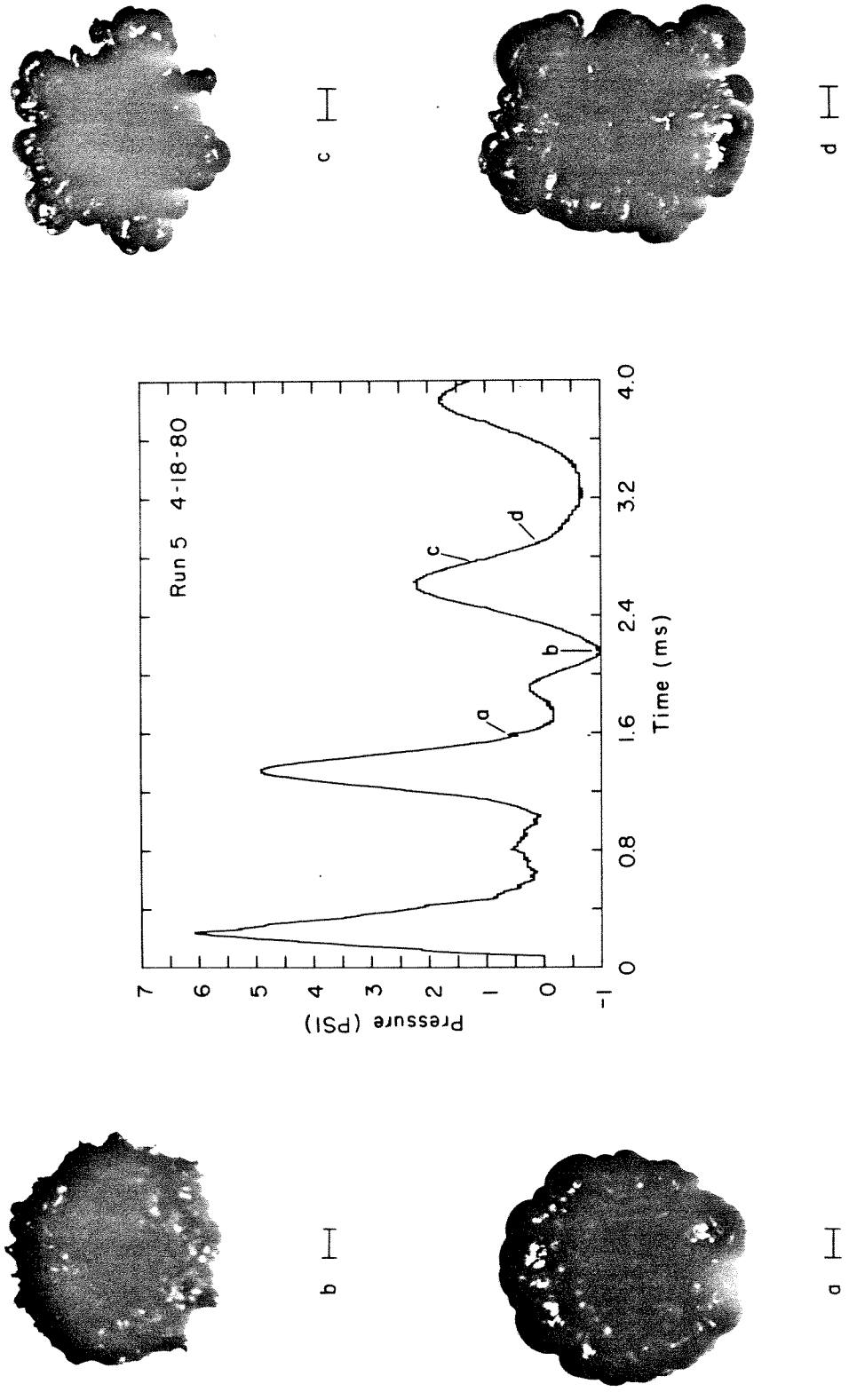

FIG. C.3 BUBBLE DEFORMATION DEVELOPMENT AT SECOND VOLUME MINIMUM.